NTNU

Norwegian University of
Science and Technology

Iron-Mediated Growth of Graphene on SiC for Radiation Detection

Adam Götz

Nanotechnology
Submission date: June 2017
Supervisor: Justin Wells, IFY

Norwegian University of Science and Technology
Department of Physics

"A person who never made a mistake never tried anything new."

ALBERT EINSTEIN

Abstract

A proposed radiation sensor exploits graphene's high electron mobility and sensitivity to miniscule electric fields to attain a novel approach for radiation detection. Realizing such a sensor is contingent on controlled growth of high-quality graphene on a semiconductor with an insulating interlayer. It has been shown that treating silicon carbide with iron prior to annealing reduces graphitization temperature to $\sim 600\,^{\circ}\mathrm{C}$ along with the formation of an iron silicide interlayer.

In this thesis the appropriateness of the SiC-FeSi-C_{Gra} system for forming radiation sensors was examined with regard to fabrication process and electrical properties. Graphene was grown in ultra-high vacuum on SiC $(000\bar{1})$ and characterized using X-ray photoelectron spectroscopy (XPS). The presence of graphene with a 30° rotation with respect to the substrate was confirmed by low-energy electron diffraction. Quantitative analysis on XPS data showed that approximately one monolayer of graphene was grown.

Samples were successfully patterned by evaporating iron through a shadow mask, and the presence of graphene selectively on exposed regions was confirmed by spatially resolved XPS. A Hall bar was formed by patterned evaporation of iron for graphene growth, and silver for contacts. Hall measurements were carried out on the device, however inconclusive results were obtained due to poor electrical contact. Photoconductance measurements showed no clear improvement in conductance under exposure to light.

Ab-initio calculations on the system suggest that the first layer of graphene interacts strongly with the underlying iron silicide layer forming a metallic buffer layer. It is hence suggested that a thicker film of graphene is grown for successful electrical measurements.

Sammendrag

En foreslått strålingsensor utnytter grafens høye elektronmobilitet og følsomhet ovenfor små elektriske felt for å oppnå en ny tilnærming til strålingsdeteksjon. Å realisere en slik sensor er betinget av kontrollert vekst av grafen med høy kvalitet på en halvleder med et isolerende mellomlag. Det har blitt vist at behandling av silisiumkarbid med jern før varmebehandling reduserer grafitiseringstemperaturen til $\sim 600\,^{\circ}\mathrm{C}$ samt å forårsake dannelsen av et jernsilisid mellomlag.

Gjennom denne oppgaven ble det undersøkt hvorvidt SiC-FeSi-C_{Gra} systemet er hensiktsmessig for å danne et strålingssensor med hensyn til både fabrikasjonsprosess og elektriske egenskaper. Grafen ble laget i ultrahøy vakuum på SiC $(000\bar{1})$ og karakterisert ved hjelp av røntgenfotoelektronspektroskopi (XPS). Tilstedeværelsen av grafen med 30° rotasjon med hensyn til substratet ble bekreftet ved lavenergi-elektrondiffraksjon. Kvantitativ analyse av XPS-data viste at omtrent ett monolag av grafen ble dannet.

Prøver ble vellykket mønstret ved deponering av jern gjennom en skyggemaske, og selektive tilstedeværelsen av grafen på eksponerte områder ble bekreftet av romlig oppløst XPS. En Hall-bar ble laget ved mønstret fordampning av jern for grafen vekst, og sølv for kontakter. Hall-målinger ble utført på prøven, men resultatene var ufullstendige på grunn av dårlig elektrisk kobling. Fotokonduktivitetsmålinger ble utført, men viste ingen klar forbedring av konduktans under eksponering for lys.

Ab-initio beregninger på systemet antydet at det første laget av grafen er sterkt påvirket av det underliggende jernsilisidlaget, og danner et metallisk bufferlag. Det foreslås derfor at en tykkere film av grafen dannes for vellykkede elektriske målinger.

Preface

This thesis was written in conclusion to the five-year study programme in nanotechnology at the Norwegian University of Science and Technology. The project spanned over the final semester of the degree and though it included many nerve-racking moments, it wound up to be the most educational time of my studies. Being a member of prof. Justin Wells' research group has given a great opportunity to work closely with skilful group members, and to learn a great deal about working in ultra-high vacuum and using X-rays for surface science.

The aim of this thesis is to summarize the experiences gathered during the course of this project, and to present it in a way accessible for an interested student from another field of science. As the majority of this project involved training and experimental work at the XPS lab, a large part of this thesis is dedicated to describing work in ultra-high vacuum. The time-frame of the project also included a visit to a synchrotron beam-time at BESSY in Berlin.

Many people have contributed to making this work possible. I would primarily like to thank group members Dr. Simon Cooil for spending countless hours helping with training at the lab, setting up the system for experiments and providing valuable advice, and Prof. Justin Wells for indispensable guidance at every stage of this project. I would also like to thank Dr. Rajesh Chellappan for support during experiments, Dr. Øystein Dahl for helping with photoconductance measurements and the NanoLab staff for providing the training for multiple instruments. Finally I would like to thank my parents and brother for their unwavering support throughout my studies, and my close friends for making studying in Trondheim a blast.

June 2017
NTNU, Trondheim

Adam Götz

Contents

List of Figures

Abbreviations

AFM Atomic Force Microscopy

ARPES Angle-Resolved Photoemission Spectroscopy

CVD Chemical Vapor Deposition

DFT Density Functional Theory

DOS Density of States

FET Field Effect Transistor

FSG Free-Standing Graphene

GGA Generalized Gradient Approximation

IMFP Inelastic Mean Free Path

LEED Low Energy Electron Diffraction

NTNU Norwegian University of Science and Technology

PES Photoelectron Spectroscopy

PMT Photomultiplier Tube

STM Scanning Tunneling Microscopy

STS Scanning Tunneling Spectroscopy

UHV Ultra-High Vacuum

UPS Ultraviolet Photoelectron Spectroscopy

XPS X-ray Photoelectron Spectroscopy

Nomenclature

Physical constants

c	Speed of light
e	Elemental charge
h	Planck constant
$\hbar$	Reduced Planck constant
k_B	Boltzmann constant
N_A	Avogadro's number

General

E	Energy
P	Pressure
t	Time
T	Temperature
$\mathbf{B}$	Magnetic flux density
$\mathbf{E}$	Electric field
$\mathbf{r}$	Position
$\mathbf{v}$	Velocity

Quantum mechanical

$\hat{H}$	Hamiltonian
m	Electron mass
N	Electron density
V	Potential energy; volume
ψ	Time-independent eigenstate
Ψ	Wavefunction
$\mathbf{G}$	Reciprocal lattice vector
$\mathbf{k}$	Wavevector

Semiconductor physics

E_F	Fermi energy
μ	Charge carrier mobility

n	Conduction electron concentration
N_C	Conduction band effective density of states
N_V	Valence band effective density of states
p	Hole concentration
σ	Conductivity
$f_F(E)$	Fermi-Dirac distribution density
$g(E)$	Density of states

X-ray physics

BE, E_b	Binding energy
KE, E_k	Kinetic energy
γ	Lorentzian width
I	Intensity
λ	Inelastic mean free path
σ	Cross section; Gaussian width
W	Shirley step width
Φ	Workfunction
$\mathrm{DS}(x, x_0, \alpha, F)$	Doniach-Sunjic function
$\mathrm{G}(x; \sigma)$	Gaussian distribution density
$\mathrm{L}(x; \gamma)$	Lorentzian distribution density
$\mathrm{S}(x; x_0, W)$	Shirley step function
$\mathrm{V}(x; x_0, \sigma, \gamma)$	Voigt function

Chapter 1

Introduction

Efficient detection of radiation is of vital importance in modern technology and society. Forms of ionizing radiation constitute an indispensable probe in various applications, from materials science and inspection of mechanical components to medical imaging and radiation protection. Advancements in experimental techniques have set increasing demands on detector technology in terms of speed, cost, efficiency, and energy- and spatial resolution – many of which today's state-of-the-art detectors have significant shortcomings in [1]. An innovative design for a radiation detector has been proposed using graphene integrated on a semiconductor substrate [2].

Graphene consists of a single sheet of carbon atoms arranged in a honey-comb lattice. Since its first successful isolation by Geim and Novoselov in 2004 [3], graphene has seen an enormous increase in interest by researchers attributed to its extraordinary mechanical, thermal and electronic properties [4–6]. Graphene is the first truly 2-dimensional material observed in nature – its conduction electrons exhibit relativistic behaviour, and may be viewed as massless charged fermions living in 2D space [7, 8] with reported experimental mobility in excess of $15\,000\,\mathrm{cm^2\,V^{-1}\,s^{-1}}$ [7]. The possibility of the electric field effect in graphene with tightly peaked resistivity near the charge-neutrality point was already shown by Geim's group [3], and has lead to prospect of replacing parts of modern semiconductor devices by graphene-based transistors for high speed electronics and in the effort to continue electronics miniaturisation [9].

The ultra-high mobility combined with high sensitivity to minuscule changes of electric field make graphene an excellent candidate material for high speed and high sensitivity sensing of charges induced in an adjacent semiconductor by incident radiation. Simulations have shown that the local electric field from single gamma-

photon absorbed in a silicon substrate can be more than sufficient for detection by a graphene overlayer [10]. The proposed device structure involves a thin insulating layer between the semiconductor substrate and graphene monolayer. An external electric field is applied normal to the substrate surface to drift radiation-induced charge carriers toward the graphene layer. This has been successfully demonstrated in a proof-of-concept SiC-graphene field effect transistor (FET) device with $\sim 200\%$ increase in conductance under exposure to visible light, and up to 70% using X-rays [11, 12].

Most promising techniques in the growth of high-quality graphene include growth on transition metal substrates by chemical vapour deposition (CVD) and epitaxial growth on silicon carbide (SiC) [13, 14]. Growth on SiC has the advantage of satisfying the requirement of a semiconducting substrate, hence eliminating an extra step of transferring graphene onto a different substrate. Graphene formation is achieved by thermal decomposition of bulk SiC at temperatures between 1000 and 1400 °C [14]. Although a number of groups have succeeded in growing large single crystalline monolayers with good reproducibility [15], controlling growth rate and high quality remain challenges. A novel synthesis method has been presented by forming a thin film of iron on SiC prior to annealing, resulting in a lowered graphitization temperature of 600 °C due to the catalytic behaviour of iron, and the formation of a iron silicide (FeSi) interlayer between the substrate and graphene [16].

The focus of this thesis is contributing to the understanding of the SiC-FeSi-C_{Gra} system, and assessing its suitability for graphene based radiation detection. Of key importance are the quality of the graphene film produced as well as the structure and electronic properties of the underlying FeSi, as it should be insulating enough to prevent charge carriers from entering the graphene sheet. Iron deposition and graphene growth will be done in ultra high vacuum (UHV) and characterised by in situ X-ray photoelectron spectroscopy (XPS) and low energy electron diffraction (LEED). Further characterisation of devices will be provided by various spectroscopic and microscopic techniques, as well as electrical measurements in the presence of a magnetic field and electromagnetic radiation. Theory and experimental work in this thesis will be supported by density functional theory (DFT) calculations using the SIESTA code [17].

Chapter 2

Theory

This chapter gives insight into selected topics viewed essential for appreciating this work. The intended audience of this text are final year Master's students within a field of science, however the flow of ideas is presented in a way that should be interesting to read also for somebody with limited scientific background.

In effort to write an independent theory section a simple model of the electronic structure of solids is first introduced, and applied to our 2-dimensional test material graphene. This is a model that can be found in any elementary text on solid state physics such as Ref. [18, 19], and is included as a review of some basic concepts relevant in this work. In the succeeding section the basic idea behind density functional theory is introduced as it is one of the leading modern tools for understanding the behaviour of solids. In Sec. 2.3 the operation of some devices relevant to radiation detection is described along with techniques of graphene growth, and in Sec. 2.4 the theory behind the experimental techniques used is outlined, with focus on photoemission spectroscopy.

2.1 Electronic properties of solids

Understanding properties of the solid state is one of the largest branches of physics and fields of research – inventions stemming from solid state physics and quantum mechanics have been estimated to account for approximately 30% of the gross national product of USA [20]. Its perhaps most remarkable accomplishments are providing the theoretical basis for materials science, and indirectly leading to the formation of the semiconductor industry. In this section we will use basic models in solid state physics to explain differences between metals, semiconductors and insulators, and

apply those models to graphene.

Much of the properties of a solid are closely related to the way electrons are arranged within it. The high thermal and electrical conductivity and malleability of metals is a consequence of their high density of states at the Fermi-level[1] leading to a delocalization of valence band electrons. In contrast, materials with the Fermi-level in a band gap tend to be more brittle, and have lower thermal and electrical conductivities due to tighter binding of electrons to specific atoms. Ultimately most properties of materials on a microscopic scale are governed by quantum mechanics[2], and in particular the time-dependent Schrödinger equation

$$i\hbar\frac{\partial}{\partial t}\Psi(\mathbf{r},t) = \hat{H}\Psi(\mathbf{r},t). \tag{2.1}$$

Unfortunately the computational effort of solving this equation scales exponentially with the number of particles in a system N, and an analytical solution exists only for the simplest system with $N \leq 2$ (hydrogen atom). As the number of particles in a macroscopic solid is in the order of $N_A \approx 10^{24}$ it is clear that the problem quickly becomes intractable for conventional computers. Fortunately – as we will see in the following sections – by applying a few approximations it becomes possible construct models using Eq. 2.1, from which one can make instructive predictions regarding properties of many materials.

2.1.1 Band theory

The first simplification that is usually made is ignoring the time-dependence in Eq. 2.1. Although there are numerous time-dependent processes occurring in solids at finite temperatures, many of the properties we are interested in are determined by the ground-state of the system. The second approximation we are going to make is that we are going to treat nuclei classically. Moreover, as the mass of an electron is around four orders of magnitude lower than the mass of the nucleus we can assume that nuclei are essentially 'frozen' in their positions, treating them as an external potential when calculating the electronic structure. This is known as the Born-Oppenheimer approximation [21].

Atomic orbitals of separated atoms have well-defined energies. As the separation between atoms decreases forming a bulk solid, the electron energies diverge into

[1]Fermi-level, or Fermi energy E_F is the energy of a hypothetical state in a solid which would have 50% probability of being occupied by an electron. The majority of states with energy lower than E_F are filled, and vice versa for higher energy states.

[2]Quantum mechanics too has failures in explaining some physical phenomena, as demonstrated by e.g. its incompatibility with general relativity.

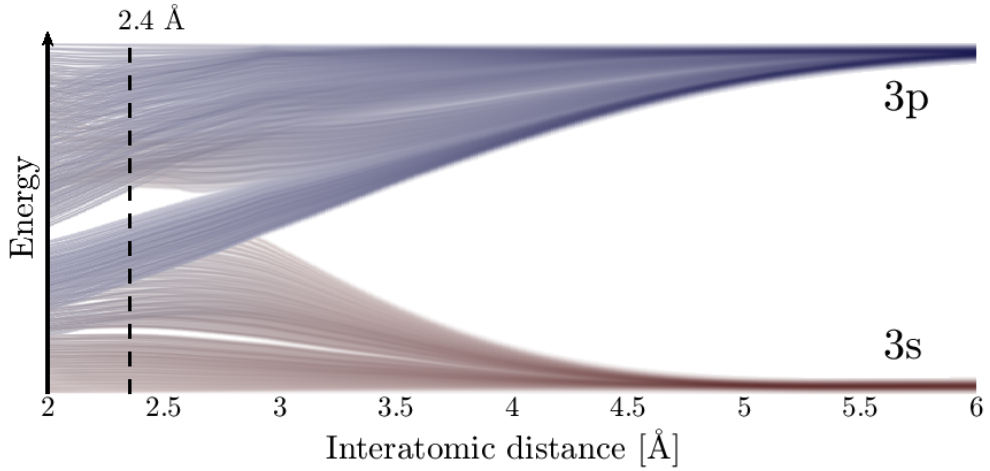

Figure 2.1: *DFT calculation of bulk silicon (diamond-cubic) valence band density of states as a function of interatomic spacing. At high separations Si atoms behave as isolated atoms with a well defined energy states. As interatomic spacing decreases, electrons in distinct orbitals split in energy forming bands of hybrid orbitals. At equilibrium distance corresponding to the Si lattice constant* 5.43 Å *[22] a band gap is observed with capacity for all four valence electrons of Si in the valence band, and an empty conduction band. Calculated using the SIESTA code [17], see Sec. 4.5 for simulation details.*

bands due to the Pauli exclusion principle stating that no two electrons can occupy the same state simultaneously. This is illustrated in Fig. 2.1 where the simulated density of states for 3s and 3p orbitals of bulk silicon is plotted as a function of interatomic spacing.

For analytical solutions to quantum systems the electron-electron interaction is sometimes ignored, in which case Eq. 2.1 reduces to the time-independent Schrödinger equation for a single particle with mass m in the potential field $V(\mathbf{r})$

$$\left[-\frac{\hbar^2}{2m}\nabla^2 + V(\mathbf{r})\right]\psi(\mathbf{r}) = E\psi(\mathbf{r}). \tag{2.2}$$

Free electron model of metals

The free electron model combines classical Drude model of electrical conduction with quantum mechanical Fermi-Dirac statistics, and gives an intuitive description of electron transport in metals [19]. It starts with all of the aforementioned simplifications along with the approximation of the potential due to the nuclei to a 3-dimensional

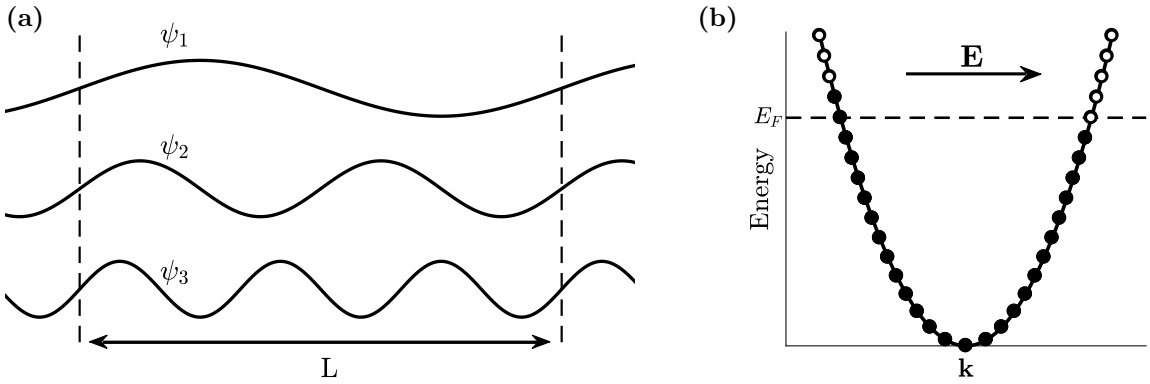

Figure 2.2: ***(a)*** *First three eigenstates of the one-dimensional particle in a box problem with periodic boundary conditions.* ***(b)*** *Electrical conduction in a metal in the presence of an electric field* **E**. *As there are available electronic states directly above the Fermi-level, electrons can rearrange into states with a net momentum resulting in a current.*

potential well – a particle in a box with volume $V = L^3$. The solution to Eq. 2.2 is then given by

$$\psi(\mathbf{r}) = \frac{1}{\sqrt{V}} e^{i\mathbf{k}\cdot\mathbf{r}} \tag{2.3}$$

where $k = \sqrt{\frac{2mE}{\hbar^2}}$ is the wavevector of the associated wavefunction.

Applying phase-matching with periodic boundary conditions $\psi(\mathbf{r} + L\mathbf{u}) = \psi(\mathbf{r})$ (see Fig. 2.2a) we get quantization of the wavevector $k_i = \frac{n_i 2\pi}{L}$ where $n_i \in \mathbb{N}$, $i = x,\ y,\ z$. The volume of a single state in k-space is then given by $\left(\frac{2\pi}{L}\right)^3$, and assuming N electrons occupying the $\frac{N}{2}$ lowest energy states within a sphere of radius k_F centered at the center of the Brillouin-zone (Γ-point) the wavevector and energy of electrons at the Fermi-level become

$$k_F = \left(\frac{3\pi^2 N}{V}\right)^{\frac{3}{2}}, \qquad E_F = \frac{\hbar^2}{2m}\left(\frac{3\pi^2 N}{V}\right)^{\frac{2}{3}}. \tag{2.4}$$

The density of states (DOS) is obtained as the derivative of the number of electronic states available with respect to energy

$$g(E) = \frac{\partial N}{\partial E} = \frac{V}{2\pi^2}\left(\frac{2m}{\hbar^2}\right)^{\frac{3}{2}}\sqrt{E}. \tag{2.5}$$

The expression for $g(E)$ shows that the density of states in a metal is proportional to the square-root of energy. At finite temperatures the some of the electrons possess sufficient energy to be excited to states above the Fermi-level, and hence the

occupancy of electronic states in a solid is given by the DOS modulated by the Fermi-Dirac distribution

$$f_F(E,T) = \frac{1}{e^{\frac{E-E_F}{k_B T}} + 1}. \tag{2.6}$$

Electrical conduction in a metal is illustrated in Fig. 2.2b. As an effectively continuous band of states are available in metals at the Fermi-level, the thermal energy is sufficient to excite a large number of electrons to higher energy states. This allows the reordering of electrons into states with a non-zero net momentum, and thus a current to flow.

Nearly free electron model

The free electron model helps to develop intuition about the electronic structure and conductivity in metals. It however fails to describe semiconductors and insulators altogether [19].

We have seen in Fig. 2.1 that the valence 3s and 3p orbitals of silicon, a semiconductor, form two continuous bands of sp^3 hybridized orbitals with capacity to hold four electrons each, separated by a band gap with no states. Hence, in order to rearrange to gain net momentum, electrons in the lower valence band must be excited to the upper conduction band by an energy greater than the band gap. If the band gap is comparable to the thermal energy $k_B T$ some electrons are thermally excited as described by the Fermi-Dirac distribution in Eq. 2.6, and the material is called a semiconductor. If on the other hand the band gap is too large for significant thermal excitations, the material is insulating. The difference between metals, semiconductors and insulators is illustrated in Fig. 2.3.

What causes the formation of a band gap in some materials? The answer lies in the periodicity of the crystal lattice. The ensuing derivation is written following Ref. [18]. One can express the periodic screened potential of the lattice as a Fourier series in terms of reciprocal lattice vectors $\mathbf{G}$ as $V(\mathbf{r}) = \sum_{\mathbf{G}} U_n e^{i\mathbf{G}\cdot\mathbf{r}}$. Similarly the wavefunction representing the solution to the time-independent Schrödinger equation inside the solid can be written as a sum of plane waves with the boundary condition analogous to the free electron model (Fig. 2.2a). Plugging these Fourier expansions into Eq. 2.2 we get

$$\left[-\frac{\hbar^2}{2m}\nabla^2 + \sum_{\mathbf{G}} U_{\mathbf{G}} e^{i\mathbf{G}\cdot\mathbf{r}}\right] \sum_{\mathbf{k}} C_{\mathbf{k}} e^{i\mathbf{k}\cdot\mathbf{r}} = E \sum_{\mathbf{k}} C_{\mathbf{k}} e^{i\mathbf{k}\cdot\mathbf{r}}.$$

Using $\nabla^2 e^{i\mathbf{k}\cdot\mathbf{r}} = -k^2 e^{i\mathbf{k}\cdot\mathbf{r}}$ in the first term, redefining $\mathbf{k}$ as $\mathbf{k} - \mathbf{G}$ in the second term, subtracting the right hand side and factoring out $\sum_{\mathbf{k}} e^{i\mathbf{k}\cdot\mathbf{r}}$, remembering that plane-

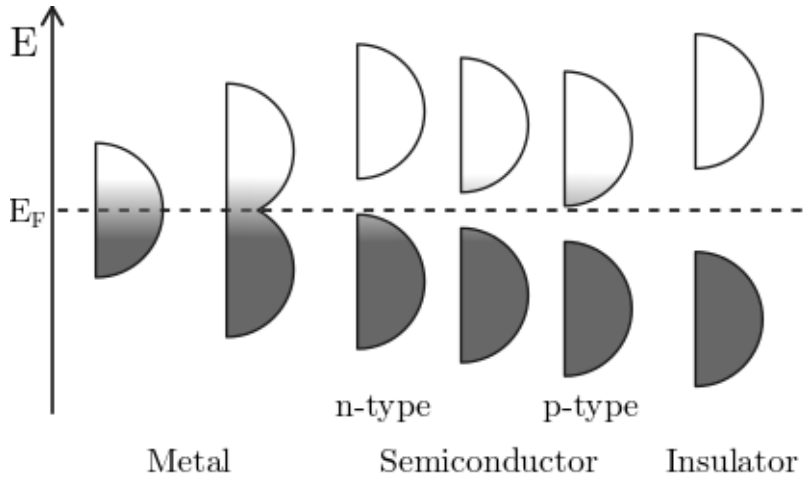

Figure 2.3: *Difference between metals, semiconductors and insulators in terms of band gap, and shifts in the Fermi-level due to doping in semiconductors.*

waves with distinct wavevectors are orthogonal and therefore must all be zero for their sum to vanish, we arrive at the central equation

$$\left(\frac{\hbar^2 k^2}{2m} - E\right) C_{\mathbf{k}} + \sum_{\mathbf{G}} U_{\mathbf{G}} C_{\mathbf{k}-\mathbf{G}} = 0. \tag{2.7}$$

The central equation represents an infinite system of equations that solved for $c_{\mathbf{k}}$ with different values of $\mathbf{k}$ in the first Brillouin zone yields the solution for the Schrödinger equation. Note that with $U_{\mathbf{G}} = 0$ for all $\mathbf{G} \neq 0$ (potential well) the solution reduces to the solution in the free electron model. The idea behind the nearly free electron model is to only include one term U_1 in a one-dimensional lattice, and to treat it using first order corrections in perturbation theory. Analysis at the Brillouin-zone boundary yields twofold degeneracy (at k and $-k$) resulting in a energy split [23, Eq. 6.26]

$$E = \frac{\hbar^2 k^2}{2m} + U_0 \pm |U_1| \,. \tag{2.8}$$

The shift up and down by $|U_1|$ at the Brillouin-zone boundary correspond to the lowest and highest points on the conduction and valence bands respectively, and hence a band gap of $E_g = 2\,|U_1|$ is formed. This characteristic gap is formed in all materials, however in metals no gap is formed at the Fermi-level either due to an odd number of valence electrons, or an overlap of the valence and conduction bands at distinct k-points.

2.1.2 Semiconductor theory

Since the mid-20th century the semiconductor industry has seen remarkable growth into the largest industry in the world today. What makes semiconductors so useful is their conductive properties that can be amply controlled by a number of factors such as light, heat, electrical fields, and most significantly minute amounts of dopants [24]. The number of electrons thermally excited to the conduction band in a semiconductor is given by the density of states multiplied by the Fermi-Dirac distribution function integrated over the conduction band

$$n = \int_{E_F}^{\infty} g(E) f_F(E,T) dE. \tag{2.9}$$

The corresponding number of holes in the valence band is obtained reversing the sign of E in f_F. Introducing the concepts effective density of states $N_{V,C}$ in the valence and conduction bands (see [24, p. 17-19] for more details) the electron and hole concentrations as charge carriers can be expressed as

$$n = N_C \exp\left(-\frac{E_C - E_F}{k_b T}\right); \qquad p = N_V \exp\left(-\frac{E_F - E_V}{K_b T}\right). \tag{2.10}$$

Although the product $np = N_C N_V e^{-\frac{E_g}{k_B T}}$ is solely determined by the properties of the semiconductor and temperature, by introducing dopants the Fermi-level can be shifted to increase the number of positive or negative charge carriers. This results in a substantial increase in the conductivity of the semiconductor, which is given by

$$\sigma = e\left(n\mu_e + p\mu_h\right). \tag{2.11}$$

where μ_e and μ_h are the electron and hole mobilities.

2.1.3 Graphene

Carbon is perhaps the most fascinating element in the periodic table – not only is it the building-block of organic molecules, making up more diversity of molecules than all other elements put together and forming the basis of life, but also in its pure form it comes in various allotropes with unique properties. Diamond is sp^3 hybridized carbon; each carbon atom is covalently bonded to four adjacent atoms in a cubic diamond structure. It has the highest hardness and thermal conductivity of all known materials [25]. Graphite is sp^2 hybridized carbon with atoms bonded in sheets arranged in a honeycomb-lattice, and loosely held by van der Waal's forces between sheets. Graphite is a soft, semimetallic material.

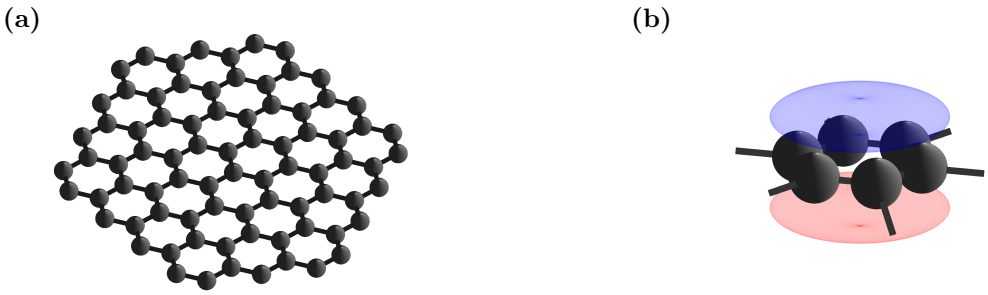

Figure 2.4: ***(a)*** *Ball-and-stick model of the structure of graphene. Each carbon atom is bonded to three neighbouring atoms with sp^2 hybridized bonds in a honeycomb pattern.* ***(b)*** *Illustration of the remaining $2p_z$ orbitals delocalized in π and π^* bands above and below the lattice.*

Graphene is a monolayer of graphite. Although theoretical models of graphene date as far back as 1947 [26], it was hypothesized as thermodynamically unstable. This was disproved when in 2004 Novoselov and Geim successfully isolated graphene from graphite sheets using tape [3]. Graphene has host of a number of interesting properties such as record high stiffness and heat conductivity [4, 5], and most importantly highly unique electrical properties [6].

Graphene is a two-dimensional material forming a hexagonal structure with two atoms per unit cell. A simple ball-and-stick model of graphene is shown in Fig. 2.4a. Each carbon atom is bonded to three neighbouring carbon atoms with sp^2 hybridized bonds, while the remaining $2p_z$ orbitals dangle out above and below the lattice forming the π and π^* bands as visualized in Fig. 2.4b. Electrons in the π bands of graphene are delocalized over the entire area of the lattice, making graphene an infinite-sized aromatic molecule, accounting for its high electrical conductivity [27].

Tight-binding model

The tight-binding model for solids is based on the assumption that electrons are strongly bound to the atom to which they belong to, and have limited interaction with surrounding atoms. The electronic band structure is calculated using a superposition of the wavefunctions for isolated atoms. In this section a short review of the tight-binding model for graphene is given following Ref. [28].

Suppose that ϕ is the solution to the Hamiltonian $\hat{H}^0$ for an isolated carbon atom. Using perturbation theory, we want to include the effect of the three nearest atoms m on the total wavefunction ψ in a honeycomb-lattice. The Hamiltonian for

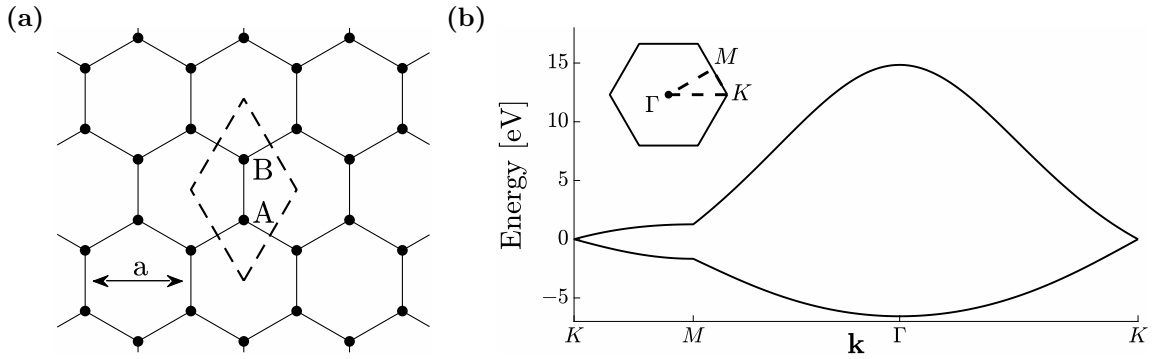

Figure 2.5: ***(a)*** *Unit cell of graphene with lattice constant a containing two atoms at inequivalent sites. Each carbon atom is surrounded by three atoms at opposite sites.* ***(b)*** *Tight-binding model of the graphene band structure showing the dispersion of bands along high-symmetry directions in the first Brillouin-zone.*

an atom j in unit cell l (see Fig. 2.5a) can then be written as$\hat{H}_j = \hat{H}_j^0 + \hat{H}_j'$, with

$$\hat{H}_j^0 = -\frac{\hbar^2}{2m}\nabla_j^2 + V\left(\mathbf{r}_j - \boldsymbol{\delta}_j - \mathbf{R}_l\right), \qquad \hat{H}_j' = \sum_{m=1}^{3} V\left(\mathbf{r}_j - \boldsymbol{\delta}_m - \mathbf{R}_l\right) \tag{2.12}$$

where $\mathbf{r}_j$ is the position of electron belonging to atom j, $\mathbf{R}_l$ is the lattice vector to the unit cell l containing j and $\boldsymbol{\delta}_m$ is the position of atom m with respect to $\mathbf{R}_l$. We can construct the solution to the total Hamiltonian in a unit cell$\hat{H} = \sum_{l=1}^{N} \hat{H}_{A,l} + \hat{H}_{B,l}$ as a trial wavefunction written as the superposition of wavefunctions for isolated atoms ϕ.

$$\psi_{\mathbf{k}} = \alpha_{\mathbf{k}}\psi_{\mathbf{k}}^{(A)}(\mathbf{r}) + \beta_{\mathbf{k}}\psi_{\mathbf{k}}^{(B)}(\mathbf{r}), \qquad \psi_{\mathbf{k}}^{(j)} = \frac{1}{N}\sum_{l=1}^{N} e^{i\mathbf{k}\cdot R_l}\phi_l\left(\mathbf{r} - \boldsymbol{\delta}_j\right) \tag{2.13}$$

The first order energy correction is given by $E(\mathbf{k}) = \frac{\langle\phi|H'|\phi\rangle}{\langle\phi|\phi\rangle}$ [23], and minimization with respect to α and β leads to the equation

$$\begin{pmatrix} H_{AA} & H_{AB} \\ H_{BA} & H_{BB} \end{pmatrix}\begin{pmatrix}\alpha \\ \beta\end{pmatrix} = E_j \begin{pmatrix} S_{AA} & S_{AB} \\ S_{BA} & S_{BB} \end{pmatrix}\begin{pmatrix}\alpha \\ \beta\end{pmatrix} \tag{2.14}$$

for which the solution is found by solving the secular equation $\det\left(\mathcal{H} - E_j\mathcal{S}\right) = 0$, where $H_{ij} = \langle\psi^{(i)}|H'|\psi^{(j)}\rangle$ and $S_{ij} = \langle\psi^{(i)}|\psi^{(j)}\rangle$ are called matrix elements.

Since only nearest-neighbour interactions are included, in diagonal matrix elements only terms of $\psi_{\mathbf{k}}^{(j)}$ with equal l (same atom in the same unit cell) need to be

considered. Diagonal matrix elements therefore reduce to the energy shift due to potential on neighbouring atoms $H_{ii} = \epsilon$ and the inner product of the function with itself $S_{ii} = 1$. The off-diagonal matrix element H_{AB} can be calculated as

$$H_{AB} = \frac{1}{N} \sum_{l=1}^{N} \sum_{m=1}^{3} e^{i\mathbf{k}\cdot\left(\boldsymbol{\delta}_{B,m} - \boldsymbol{\delta}_A\right)} \left\langle \psi^{(A)}(\mathbf{r} - \boldsymbol{\delta}_A) | H | \psi^{(B)}(\mathbf{r} - \boldsymbol{\delta}_{B,m}) \right\rangle . \tag{2.15}$$

The negative of the inner product in Eq. 2.15 is denoted γ_0 and called the inter-atomic matrix element. It is the most important matrix element, describing the bond energy between neighbouring carbon atoms. H_{AB} can be written as the product $-\gamma_0 f(\mathbf{k})$ where $f(\mathbf{k})$ the is sum of the phase factors (see Fig. 2.5a)

$$f(\mathbf{k}) = e^{\frac{ik_y a}{\sqrt{3}}} + 2e^{-\frac{ik_y a}{2\sqrt{3}}} \cos\left(\frac{k_x a}{2}\right). \tag{2.16}$$

Similarly the remaining matrix elements reduce to $H_{BA} = -\gamma f^*(\mathbf{k})$, $S_{AB} = s_0 f(\mathbf{k})$ and $S_{BA} = s f^*(\mathbf{k})$. Plugging the matrix elements into the secular equation and solving for E we get

$$E_{\pm} = \frac{\epsilon_{2p} \pm \gamma_0 \left| f(\mathbf{k}) \right|}{1 \mp s_0 \left| f(\mathbf{k}) \right|}. \tag{2.17}$$

In figure 2.5b the tight-binding valence and conduction bands of graphene are plotted for $\epsilon = 0$, $\gamma_0 = 3.033\,\mathrm{eV}$ and $s_0 = 0.129$ [29]. Note the linearity of the curve near the K point – this gives rise to some interesting properties as described in the following section.

Electronic transport in graphene

The valence and conduction band structure of graphene from a DFT calculation is shown in Fig. 2.6. Although the two bands are not permitted to overlap, they touch at six points (K-points) at the edge of the first Brillouin-zone named *Dirac-points*. In pristine graphene the Fermi-level lies directly at the crossing between the two bands where the density of states vanishes, making graphene a zero band gap semiconductor, or a semimetal.

A unique property of graphene is the linear relationship between energy and wavevector at the Dirac points, which is a consequence of the two-dimensional nature of graphene [7]. This relationship can be written as

$$E = \pm \hbar v_F \left| \mathbf{k} \right| \tag{2.18}$$

where v_F is the Fermi-velocity, the velocity of an electron at the Fermi-level measured experimentally to approximately $1.0 - 1.1 \times 10^6\,\mathrm{m\,s^{-1}}$ [6]. This equation differs on

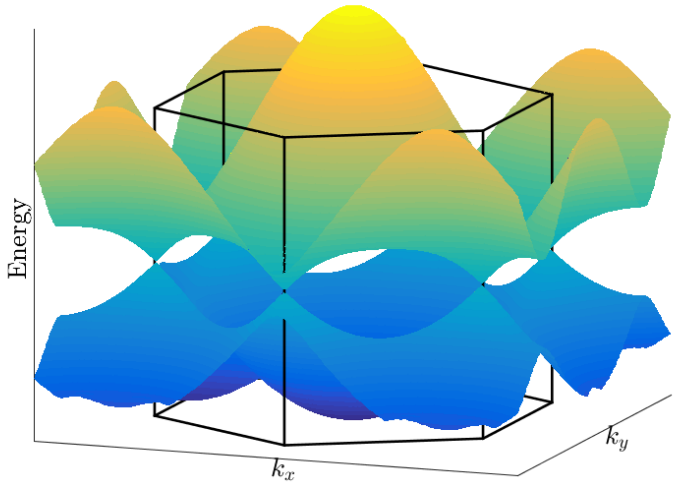

Figure 2.6: *Band structure of graphene. The valence and conduction bands meet at six points called Dirac points. Much of graphene's unique properties are due to the linear dispersion of bands near these points, resulting most notably in a highly pronounced ambipolar field effect. Simulated using SIESTA, see Sec. 4.5.*

a fundamental level from the characteristic parabolic dispersion exhibited by semiconductors at the bottom of the conduction band / valence band top (Eq. 2.8). Comparing electronic dispersion of graphene near the Dirac point to the relativistic energy of a particle given by

$$E = \sqrt{m^2c^4 + p^2c^2}, \tag{2.19}$$

where m and p are the rest mass and momentum of the particle and c is the speed of light, we can see that this linear relationship at Dirac points implies that electrons behave as zero rest mass particles, obeying the Dirac equation for relativistic particles – hence the name *Dirac-points*.

At room temperature graphene exhibits an exceptionally high electron mobility. Mobilities as high as $200\,000\,\mathrm{cm^2\,V^{-1}\,s^{-1}}$ [30] in free standing graphene and beyond $10\,000\,\mathrm{cm^2\,V^{-1}\,s^{-1}}$ on SiC [31] have been measured. This can be partially attributed to the zero effective rest mass as described above. Another cause has to do with scattering by optical phonons – in conventional semiconductors optical

phonon scattering dominates at room temperature [32], however in graphene, being a 2-dimensional solid, energies of optical phonons are too high to be excited at room temperature [33]. In addition graphene has low DOS near the Fermi-level, and thus the probability of electrons coupling with optical phonons is low.

Another interesting property of graphene highly relevant for this thesis is its highly pronounced ambipolar field effect. The Fermi-level of graphene can be tuned by the application of an electric field which results in a high increase in the density of states at the Fermi-level, and hence in conductivity. An increase in the charge carrier concentration up $10^{13}\,\mathrm{cm}^{-2}$ while retaining high mobility has been demonstrated [3]. This is illustrated in Fig. 2.7. The sharp response of conductivity to changes in bias is the property of graphene we wish to be exploit in the fabrication of novel radiation sensors.

2.2 Density functional theory

In the previous section a few examples of analytical solutions to the time-independent Schrödinger equation for bulk materials were shown with the approximation of non-interacting electrons. Although this can yield intuitive understanding of the behaviour of solids, for a more accurate description of real materials computational solutions of the Schrödinger equation including electron-electron interactions are preferred. The other two aforementioned approximations, namely the Born-Oppenheimer approximation and the treatment of only ground-state electronic configurations are still going to remain applicable in the scope of this discussion. Using this new set of assumptions, the many-electron Schrödinger equation can now be written as

$$\left[-\frac{\hbar^2}{2m}\sum_{i=1}^{N}\nabla_i^2+\sum_{i=1}^{N}V(\mathbf{r}_i)+\sum_{i=1}^{N}\sum_{j<i}U(\mathbf{r}_i,\ \mathbf{r}_j)\right]\psi=E\psi \tag{2.20}$$

where final term inside the brackets accounts for the electron-electron interaction, and the wavefunction ψ is now a complex function of the spatial coordinates of all N electrons in the system, that is an $3N$-dimensional function. As already discussed this equation is intractable even for relatively small systems – solving it for a single water molecule with 10 electrons involves solving for a function of 30 variables.

Density functional theory (DFT) is a computation method in which the Schrödinger equation is solved in a form where the ground state of the system is expressed in terms of the electron density $n(\mathbf{r})$ rather than wavefunction ψ. Its foundation rests on the mathematical theorems proved by Kohn and Hohenberg [34] stating that

1. The ground state kinetic and exchange energy of a quantum system [first and

last terms inside brackets in Eq. 2.20] is a universal functional[3] of electron density.

2. The electron density that minimizes the total energy functional is the ground state electron density of the system.

These theorems have a profound consequence – they prove that the problem of solving Eq. 2.20 for a $3N$-dimensional wavefunction can be reduced to the problem of solving an equation with respect to a 3-dimensional electron density. A surprising implication of these theorems is that in fact the same amount of information of a quantum system is contained in its 3-dimensional electron density as in its $3N$-dimensional wavefunction.

At first glance the Hohenberg-Kohn theorems may seem too good to be true, however they come with a catch; although it can be proven that a universal functional of energy in terms of electron density exists, its exact form is unknown. The basis of density functional theory is solving the electron density for approximate forms of the functional. The following discussion in based on Ref. [21].

In practice, within the framework of Kohn-Sham DFT, the many-particle equation in Eq. 2.20 is written in terms of a single particle moving in an effective potential

$$\left[-\frac{\hbar^2}{2m}\nabla^2 + V(\mathbf{r}) + V_H(\mathbf{r}) + V_{\mathrm{XC}}(\mathbf{r})\right]\psi_i(\mathbf{r}) = \epsilon_i\psi_i(\mathbf{r}) \tag{2.21}$$

where the three potentials appearing in the equation are the potential due to atomic nuclei $V(\mathbf{r})$ also appearing in Eq. 2.20, the Hartree potential given by

$$V_H(\mathbf{r}) = e^2 \int \frac{n(\mathbf{r}')}{|\mathbf{r} - \mathbf{r}'|}\,\mathrm{d}^3r' \tag{2.22}$$

representing a 'classical' electron-electron repulsion of the electron density, and the unknown 'quantum' part $E_{\mathrm{XC}}(\mathbf{r})$ called the exchange-correlation functional. A solution to the problem is found iteratively by initially 'quessing' an electron density, calculating the Hartree potential and an approximate version of V_{XC}, and solving Eq. 2.21 for the single particle wavefunction ψ_i used to calculate the new $n(\mathbf{r})$. The electron density is adjusted, and the process is repeated until it converges into the same value before and after an iteration.

The two most notable approximations for V_{XC} are the *local density approximation* (LDA) and the *generalized gradient approximation* (GGA). The LDA functional

[3] A functional is a function which takes another function as an input and returns a single value, e.g. returns the energy from the electron density function of three spacial coordinates.

approximates V_{XC} at a point to the exchange correlation functional of a homogeneous electron gas for which an analytical solution exists in limiting cases, and can otherwise be calculated numerically. More sophisticated approximations for V_{XC} exist such as the GGA which also takes into account local gradient of electron density, and can in some cases lead to more physical results. It should however be noted that unlike with the exact form of the Schrödinger equation, even given infinite computation time the solutions obtained using approximate energy functionals are not exact solutions to Eq. 2.20.

In addition to the use of approximate exchange-correlation functionals most DFT codes distinguish between valence- and core electrons by only treating valence electrons explicitly. The interaction of core electrons with other atoms is ignored, and their contribution is included in the potential from atomic nuclei $V(\mathbf{r})$ in the form of a pseudopotential. This entails that the electron density only needs to model the valence electron density of the system, reducing the amount of detail and hence simplifying the problem.

The electron density in DFT codes is typically represented as an expansion in some non-spatial basis set. Basis sets can be categorized as localized and spatially extended. A typical example of a localized basis is a function resembling the atomic orbitals of atoms. Such bases have the advantage of requiring fewer basis functions to represent realistic electron densities, however they tend to be numerically less stable. Localized basis sets are most commonly used for modelling molecules in computational chemistry. Spatially extended basis sets include plane waves, which are often used in modelling bulk materials due to the their resemblance to the electronic states in actual solids.

2.3 Device fabrication and operation

In this section aspects related to the fabrication and operation of graphene based radiation sensors is outlined. The section starts with an introduction to the operation of currect radiation sensors, including the two main types *ionization-based* and *scintillator* detectors. Next, a review of the operation of graphene field effect transistors FET is given, and related to the operation of the suggested graphene based radiation detector. As the final device fabricated in this thesis has the form of a Hall bar, basic Hall theory is also outlined. Finally, a short summary of various methods of graphene fabrication is given, with emphasis on iron mediated growth on SiC [16].

2.3.1 Modern radiation detection

When discussing radiation detection it is important to be aware what type of radiation is being detected. The term radiation is defined as the transmission of energy through space or matter in the form of particles or waves. This definition encompasses a vast number of phenomena, which based on the relevant branch of physics for instance can be divided into electromagnetic, particle, acoustic and gravitational radiation. The forms of radiation relevant in the context of this thesis include particle radiation and visible to high-energy electromagnetic radiation. The following discussion is based on Ref. [1].

Current state-of-the-art radiation detectors are based on two distinct principles of operation, both of which were already demonstrated over a hundred years ago. *Ionization-based detectors* consist of a potential applied between two opposing electrodes around an *active volume*, usually filled with a reactive gas. Absorption of radiation causes ionization of the gas which is then swept by the potential toward opposing electrodes, allowing a detectable current to flow. These types of detectors are typically used for the detection of particle radiation such as alpha-radiation or neutrons.

Ionization based detectors have three working modes depending on the anode voltage. At low voltages only ions from the initial ionization are detected, and hence the signal is weak. At a medium voltage avalanche multiplication occurs and the signal is amplified, however without saturation, and the signal is hence still proportional to the amount of initial ionization. At high anode voltages saturation occurs, and the detector operates in a *Geiger counter* mode. Gas detectors are usually operated at medium voltages in the proportional region as this allows the determination of how much ionization was created by the absorbed radiation.

The advantage of ionization based detectors is their simple working principle which allows any type of radiation causing ionization in an active volume to be detected. Their main disadvantage is that detection is based the drift of ions causing low response speed with a high associated *dead time*.

Scintillator detectors are based on the emission of photons in a scintillator crystal as a result of absorbed radiation. The intensity of the emitted photons is proportional to the energy of absorbed, which in case of incident gamma-rays allows determining the energy of incident particles by analysis of the height of the electrical pulse produced. Determining the kinetic energy of neutrons by this method is not possible as the main contribution to the absorption energy comes from capturing the free neutron into a nucleus, and the ionization from thermalizing fast neutrons is relatively small. The photons emitted in the scintillator are detected usually by means of a

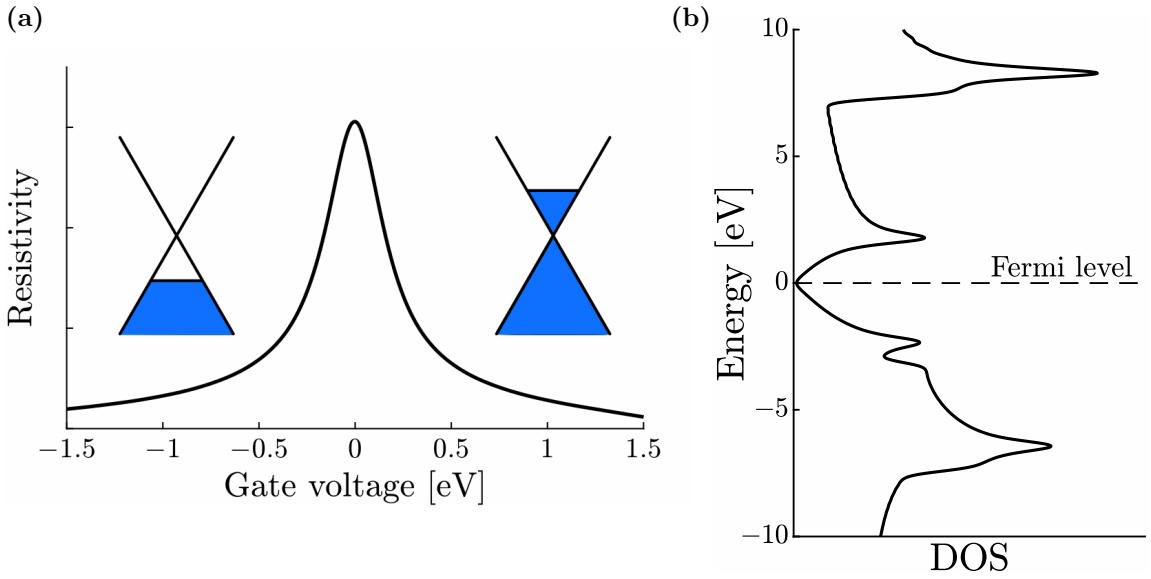

Figure 2.7: ***(a)*** *Ambipolar field effect in graphene. A gate bias resulting in a perpendicular electric field can be used to shift the Fermi-level of graphene, changing the conductivity of the sheet. At the Dirac-point this leads to a sharply peaked resistivity.* ***(b)*** *Density of states in graphene. Calculated using SIESTA, see Sec. 4.5.*

photomultiplier tube (PMT). The advantage scintillator detectors have compared to ionization based detectors is their higher detection speed and lower dead time. They also tend to be more robust, although distinguishing between photons and neutrons using scintillator detectors is generally more difficult.

2.3.2 Graphene based devices

Graphene, as reviewed in Sec. 2.1.3, is host for a number of unique properties that make it an interesting candidate for use in various electronic applications. Its most promising property for the scope of this thesis is its strong ambipolar field effect. Due to the linear dispersion of the electronic bands near the Dirac-points, the density of states – and hence the conductivity – is highly affected by the application of minute amounts of electrical bias [3]. The connection between graphene's density of states and peaked conductivity at the Dirac-point is illustrated in Fig. 2.7. This property makes graphene an ideal material for applications such as field effect transistors and radiation sensors.

Graphene field-effect transistor

Field-effect transistors use an electric field to control the electrical behaviour of the device. It is a three-terminal device where the resistance between the source and drain is controlled by an electric field applied via a gate voltage. Metal-oxide-semiconductor field-effect transistors are the main component of the majority of modern electronics, and hence an improvement in their performance is of great interest for scientists and society.

The operation of the most common field-effect transistors is based on controlling the amount of majority charge carriers in a semiconducting channel between the source and drain terminals [24]. A similar effect can be achieved exploiting the ambipolar field effect exhibited by graphene – applying a gate voltage can shift the Fermi-level of graphene, changing the density of states at the Fermi-level, and hence the conductivity of the sheet. This is illustrated in Fig. 2.7. Graphene based field-effect transistors have the advantage of exploiting the high sensitivity of graphene as well as its high electron mobility, resulting in transistors with higher sensitivity to the gate voltage and faster switching time [2].

Radiation detector

The principle of a graphene based field-effect transistor can be applied to make a radiation sensor. The idea is to grow graphene onto a semiconductor with a thin insulating interlayer. The device structure is shown in Fig. 2.8. A gate voltage is applied on the bottom contact resulting in a electric field perpendicular to the sample surface. As radiation is absorbed in the semiconductor causing ionization, charged particles are driven toward opposite sides of the device by the electric field. Charged particles are stopped by the insulating interlayer, however changes in the local electric field causes a shift in the Fermi-level of graphene resulting in a change in its conductance.

The advantage of this detector design lies in the unique properties of graphene. Current state-of-the-art detectors rely on the amplification of the signal from incident radiation by means of avalanche multiplication in ionization based detectors, or a PMT in the case of scintillator detectors. The amplification leads significant dead-time of the detectors, limiting the maximum frequency at which individual particles can be detected. Due to the extreme sensitivity of graphene to electrical fields at the Dirac point no such amplification is necessary in a graphene based device, which along with the high electron mobility of graphene leads to the superior performance of the device.

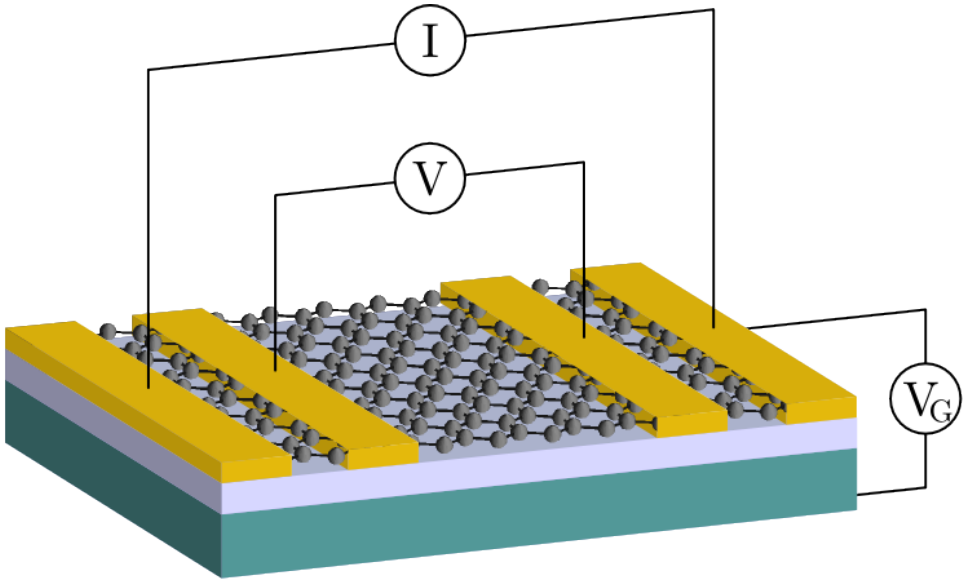

Figure 2.8: *Illustration of a potential design for a graphene based radiation sensor. Radiation is absorbed by the green semiconductor substrate creating free charge carriers. Opposite charges are sweeped toward opposite sides of the device by a potential V_G applied to a bottom contact, and stopped by a thin insulating interlayer (white). Changes in the local electric field due to ionization are detected by measuring the conductance of a graphene sheet at the sample surface using the four point probe method by applying a current I and measuring the potential difference V.*

Hall theory

Much of the electrical behaviour of a material is characterized by its majority charge carrier type, concentration and mobility. Although the resistivity of the material is determined by the latter two, none of these parameters can be determined by electrical measurements alone. They can however be measured exploiting the Hall effect. Measuring the mobility of graphene is useful as it can provide convincing evidence of the formation of graphene due to its uniquely high value, as well as means to determine the quality of the graphene layer by comparing to mobility in other settings found in literature.

The Hall effect is exhibited by materials in the presence of non-parallel electric and magnetic fields. The situation is illustrated in Fig. 2.9 where a current I_x is passed through a sample in the x-direction in the presence of a magnetic field $\mathbf{B}$ in the z-direction. The Lorentz-force on a charged particle in the sample with charge q

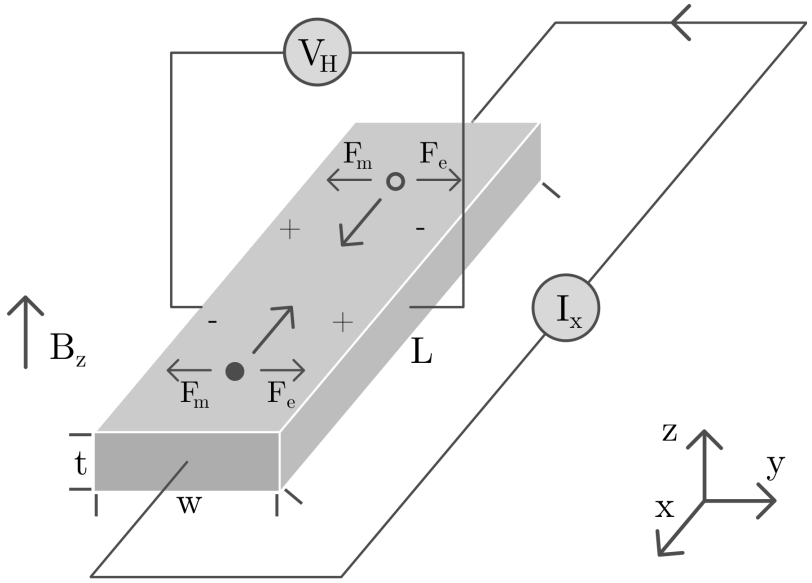

Figure 2.9: *The Hall effect. Charge carriers making up a current I_x through the sample are deflected in the presence of a normal magnetic field. An uneven distribution of charges arises to compensate for the magnetic force which can be measured as the Hall voltage V_H. At equilibrium the Lorentz force in y vanishes, implying $F_m = F_e$.*

is then given by

$$\mathbf{F} = q\left[\mathbf{E} + (\mathbf{v} \times \mathbf{B})\right] \tag{2.23}$$

where $\mathbf{E}$ is the electric field driving the current and $\mathbf{v}$ is the velocity of the particle. As the magnetic field term in the force is pointing in the direction orthogonal to the particle's velocity, the particle trajectory will bend toward one of the sides of the Hall bar depending on the sign of the particle's charge. This will create a voltage measured across the y-dimension of the sample. At equilibrium the magnetic force and the force due to the Hall voltage V_H will be equal

$$\frac{V_H}{w} = v_x B_z$$

which assuming one majority type of charge carriers can be rearranged to give an expression for the Hall voltage

$$V_H = \frac{I_x B_z}{nqt} \tag{2.24}$$

where n is the charge carrier density and t is the thickness of the sample.

The result of a Hall measurement can be summarized in terms of the Hall-coefficient R_H defined as

$$R_H \equiv \frac{E_y}{j_x B_z} = \frac{1}{nq} \tag{2.25}$$

where E_y is the electric field component caused by the Hall voltage [24]. The sign of the Hall voltage determines whether charge transport occurs mainly by the movement of electrons or holes in semiconductor, and its magnitude is related to the concentration of such carriers. By independently measuring the conductivity σ of the sample, which can simply done by four-probe measurements on the Hall bar in the absence of the magnetic field, the electron mobility in a negative majority charge carrier sample can be found using

$$\mu_n \equiv \frac{v_x}{E_x} = \sigma R_H \tag{2.26}$$

2.3.3 Graphene synthesis

Since it was first knowingly isolated by Geim and Novoselov in 2004 by means of mechanical exfoliation, exploring methods of graphene growth has become an extensive area of research. Although numerous techniques are being studied, three methods are particularly notable for their high quality of the film produced and/or scalability for large area production.

Mechanical exfoliation is the technique initially used by Geim's group to isolate graphene, and is today still known to produce the highest quality graphene in terms of electrical properties [14]. As however crystallites produced are typically under 1 mm in size, the method is not easily applicable in large-scale production of graphene for device fabrication. Mechanically exfoliated graphene nevertheless remains the benchmark in terms of electrical properties, to which graphene formed in other synthesis methods is compared to [14].

The remaining two methods for graphene growth are chemical vapour deposition (CVD) and and epitaxial growth on SiC. Although the electrical properties of graphene produced by these methods are affected by the substrate, they are more promising candidates for large-scale production, and are more compatible with modern semiconductor processing techniques.

Chemical vapor deposition

Chemical vapour deposition is a chemical process in which gaseous precursors at a high temperature react or decompose at the surface of the substrate producing a desired deposit. Gaseous bi-products are subsequently removed by gas flow. Chemical

vapour deposition is attractive for producing graphene as it is an inexpensive and readily accessible method. Graphene growth have been demonstrated by CVD on top of various single crystal metal surfaces such as nickel, gold, platinum, copper and several others [13].

CVD methods of producing graphene can be divided into two types [13]. Graphene growth in a top-down method involves catalytic de-hydrogenation of hydrocarbon gas at the sample surface, allowing carbon to be deposited at the surface. As the catalytic effect only occurs at the metal surface, the process will stop after fully covering the surface hence forming a uniform carbon layer. In a bottom-up approach carbon is forced into the substrate under high pressure, and subsequently precipitates out under the driving force of lower surface energy, forming a graphene film at the surface.

The properties of the resulting graphene film are largely determined by the interaction between graphene and the underlying substrate. Due to a mismatch in the graphene and substrate lattice constants a Moiré pattern is typically formed. This in addition to bonding with the substrate affects the electrical properties of graphene, which will be dependent on the substrate material. Another critical quality of the graphene layer grown is the size of the grains formed. By keeping the number of nucleation sites low, growth of as large as 5 mm crystallites have been routinely achieved [15].

Epitaxial growth on silicon carbide

Another promising method of graphene synthesis involves thermally anneal SiC forming graphitized carbon on high quality surface of silicon carbide. SiC is a wide band gap semiconductor (6H-SiC band gap 3.05 eV [35], see DFT band structure in Fig. 2.11) consisting of stoichiometric amounts of silicon and carbon in a tetragonal structure, where each atom is bonded to four atoms of the opposite element. Due to free rotation of tetrahedral units in layers, various polymorphs of SiC exist. High quality crystals include predominantly one stacking sequence, the most common types being 3C-SiC, 4H-SiC and 6H-SiC where C stands for cubic, H for hexagonal and the number is the number of tetragons stacked in a single unit cell. The crystal structure of 6H-SiC is shown in Fig. 2.10a.

Although graphitization on SiC through thermal annealing has been known for a long time, it wasn't until 2004 de Heer *et al.* performed transport measurements revealing the Dirac nature of charge carriers, and electron mobility values exceeding $1100\,\mathrm{cm^2\,V^{-1}\,s^{-1}}$ [36]. The main advantage of thermal decomposition of SiC is that graphene is grown directly on a semiconductor substrate, and no transfer is necessary for the fabrication of electronic devices.

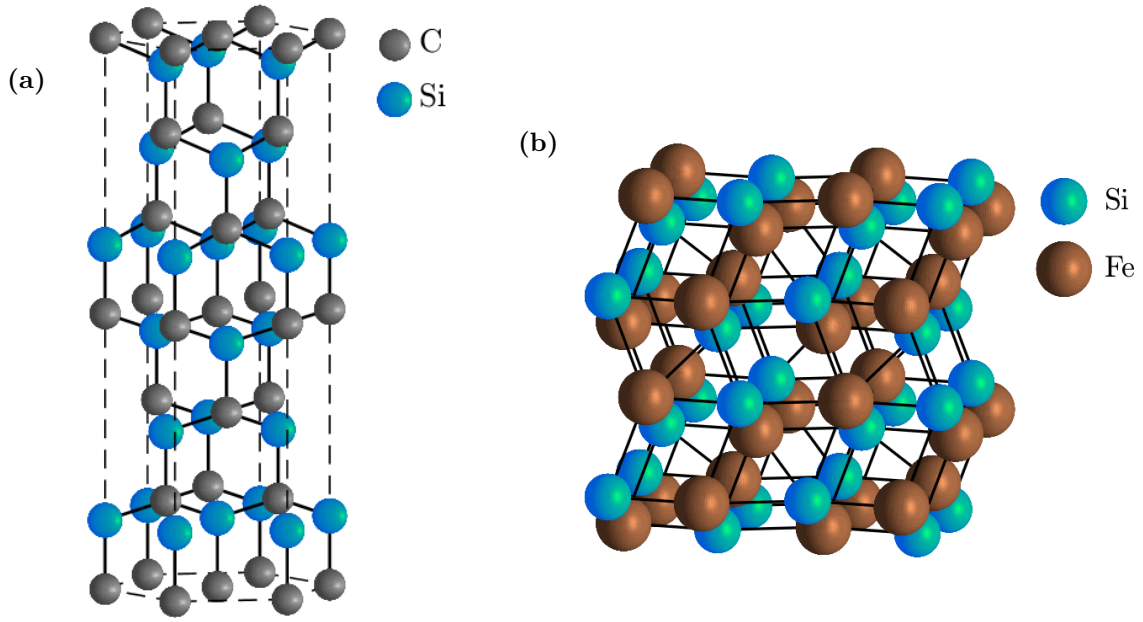

Figure 2.10: ***(a)*** *Conventional unit cell of 6H-SiC. It is a polymorph of SiC with six layers of Si-C tetrahedrons arranged in a ABCACB stacking sequence.* ***(b)*** *Crystal structure of (cubic) ϵ-FeSi. Each unit cell consists of four iron and silicon atoms. The atoms within the unit cell are arranged such that each atom is equidistant to seven other atoms.*

Growth of graphene on SiC occurs at high temperatures by sublimation of silicon out of the sample, with the remaining carbon atoms rearranging in a graphitic structure. Graphene grows in a $(6\sqrt{3} \times 6\sqrt{3})\mathrm{R}30°$ structure, with the first layer partially bonded by covalent bonds to the substrate, thus not exhibiting characteristic properties for graphene and thereby called a *buffer layer* [14]. Graphene growth can be achieved on Si- (0001) and C-terminated SiC $(000\bar{1})$, however growth on the (0001) face is usually preferred. This is because graphene growth on SiC (0001) is slower and hence more easily controlled. Annealing to approximately 1250 °C results in one monolayer in a more or less self-terminating reaction, while growth on $(000\bar{1})$ face growth occurs already at 1100 °C and is more difficult to control [14].

A novel method of graphene growth on SiC treated with iron has been presented in Ref. [16]. The method involves the deposition of a thin film of iron on SiC which lowers the graphitization temperature to approximately 600 °C. The method relies the reaction of iron with silicon rather than silicon sublimation, and the catalytic conversion of carbon from an sp^3 to sp^2 hybridized state. The reaction can be

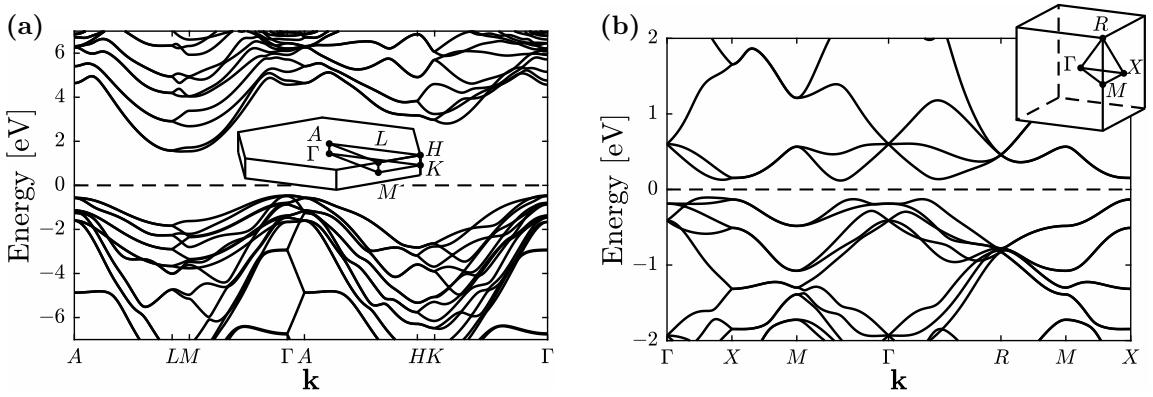

Figure 2.11: *Electronic band structure of* ***(a)*** *6H-SiC and* ***(b)*** *cubic FeSi along high-symmetry directions. SiC is a wide band-gap semiconductor and ϵ-FeSi is a narrow band gap semiconductor. Plots presented here are DFT calculations with SIESTA using the generalized gradient approximation (see Sec. 4.5), and hence underestimate the true band gap of the materials.*

summarized as

$$\mathrm{SiC} + \mathrm{Fe} \rightarrow \mathrm{FeSi} + \mathrm{C_{Gra}} \tag{2.27}$$

The resulting structure formed is a film of graphene on a iron silicide interlayer. Although the exact structure and stoichiometry of the iron silicide formed is not known, evidence suggests that predominant phase is cubic ϵ-FeSi (space group 198) [16]. The crystal structure of ϵ-FeSi is shown in Fig. 2.10b.

This processing method has numerous advantages. By lowering the annealing temperature from 1250 to 600 °C the process of forming graphene becomes more compatible with other semiconductor manufacturing processes. The stoichiometric combination of Fe with Si also allows precise control over the thickness of graphene layer formed, and potentially provides means of graphene patterning. Depending on the electronic properties of the FeSi interlayer, it could also be an advantage for the formation of devices – for production of the radiation sensors described in Sec. 2.3.2 it would be desired that the interlayer formed is insulating, although this is not known for sure.

2.4 Theory behind experimental techniques

In this section the principles of main characterization methods used in this thesis are outlined. As the emphasis of this thesis is placed on techniques carried out within an UHV system, only those will be discussed here, with focus on photoemission

spectroscopy (PES).

2.4.1 Photoemission spectroscopy

The basis for photoelectron spectroscopy stems from the discovery of the photoelectric effect, and its interpretation in 1905 by Albert Einstein in his notorious paper leading to the quantum revolution in physics [37]. The photoelectric effect is an interaction between a photon and an electron bound in an atom where the photon is absorbed with its energy transferred to the electron which is ejected from the atom. Photoemission spectroscopy refers to the utilisation of the photoelectric effect to excite electrons by incident photons, and the detection of emitted electrons to probe the occupied electronic states in a sample.

The variety of information carried by electrons makes photoemission techniques highly attractive in many applications. PES is a standard tool in surface science in e.g. the determination of compositional structure at the surface, identification of chemical states for characterizing reactions and electronic band-structure measurements. The suitability of PES for surface analysis is credited to the short attenuation length of photoexcited electrons in a sample. While typical photons at energies used in PES such as X-rays penetrate the sample deep enough to excite bulk electrons, only electrons from the top few nanometers escape to the surface and are ejected into vacuum. Photoemission spectroscopy encompasses a number of techniques with variations differing in the terms of the property of the sample explored, and subsequently characteristics of the photon source, range of electron energies scanned and other acquisition features such as optional angular or spacial resolution.

Technique overview

A typical photoemission setup using X-rays as the excitation source in an ultra-high vacuum (UHV) system is shown in figure 2.12. This technique is named X-ray Photoelectron Spectroscopy (XPS), and is perhaps the most common photoemission technique used mainly for probing inner shell – or *core level* – electrons in a sample. It was developed by Kai Siegbagn in 1957 who was later awarded a Nobel Prize for his work [38].

The technique is highly surface-sensitive due to the strong interaction of electrons with matter. As core level electrons have sharply defined energies, XPS spectra can be used as 'fingerprints' for various elements making XPS an excellent technique for elemental analysis. Quantitative XPS can be used to determine the thickness of a thin-film on a substrate, say something about the uniformity of a sample, and get information about the chemical environment of elements based on peak shifts.

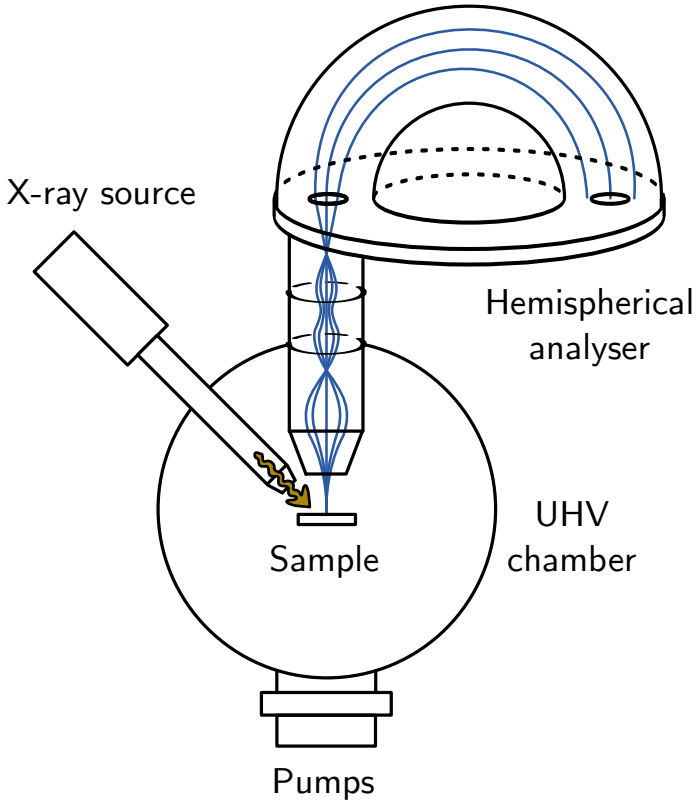

Figure 2.12: *Typical XPS setup in ultra-high vacuum. A sample is illuminated by photons from an X-ray source, and the photoemitted electrons are scanned in energy and detected in a hemispherical electron analyser.*

Photoemission of electrons can be approximated semi-classically in a three step process as **(1)** the excitation of the electron onto higher energy state, **(2)** its propagation through the sample to the surface, and **(3)** its ejection into vacuum [39]. The first step involves matching the energy and wavevector of the initial electron state plus photon with an unoccupied electronic state. This together with the creation or absorption of phonons to ensures energy and momentum conservation of the system. The photon momentum and phonon energy can often be neglected in analysis as they are small relative to other terms.

In the second step of the process the electron propagates through the sample to its surface. Due to their strong interaction with matter electrons are likely scatter or be absorbed travelling distances longer than a few nanometers. Once the electron has reached the surface it has to overcome the difference between the sample and

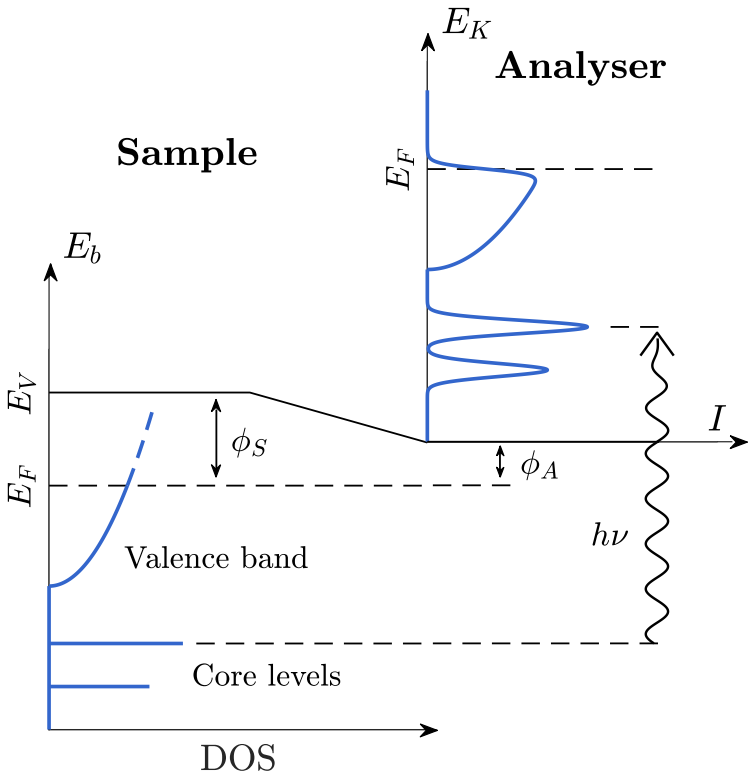

Figure 2.13: *Energy diagram of the photoemission setup. Electrons bound to the sample are excited by photons with energy $h\nu$, and emitted with a kinetic energy given by Eq. 2.28. As the sample and the analyser are in electrical contact their Fermi-levels align leading to a potential gradient in the vacuum level E_V. Electrons are detected at the analyser with the kinetic energy in Eq. 2.29.*

vacuum level potentials given by the workfunction of the sample Φ_S. While the lateral momentum of the electron is conserved, due to the workfunction momentum perpendicular to the sample surface is not conserved. The kinetic energy in vacuum of the emitted electron is given by

$$E_k = h\nu - E_b - \Phi_S \tag{2.28}$$

where $h\nu$ is the energy of the photon and E_b is the binding energy[4] of initial state of the electron. In a photoemission setup the sample is usually in electrical contact with the energy analyser, in which case the kinetic energy measured at the analyser

[4]The binding energy of a state is defined as the energy taken to excite an electron up to the Fermi-level.

Table 2.1: *Atomic quantum numbers and their ranges. In photoemission orbital notation is used to denote direct photoemission peaks and X-ray notation to denote Auger electron peaks.*

Q. number	Range	Degeneracy	Orbital notation	X-ray notation
n	$\mathbb{N}$	$2n^2$	$1,\ 2,\ 3\ldots$	$K,\ L,\ M\ldots$
l	$0 \leq l \leq n-1$	$2\,(1+2l)$	$s,\ p,\ d\ldots$	$1,$ 2-3, 4-5$\ldots$
m_l	$-l \leq m_l \leq l$	2		
m_s	$\pm 1/2$	1	$j = \lvert l + m_s \rvert$	$1;\ 2,3;\ 4,5\ldots$

is given in terms of the analyser workfunction Φ_a (see Fig. 2.13) as

$$E_K = h\nu - E_b - \Phi_a. \tag{2.29}$$

Atomic orbitals

Prior to looking at an example XPS spectrum it is instructive to review some basic results from atomic physics. The solution to the time-independent Schrödinger equation (Eq. 2.2) for a particle in a spherical Coulomb-potential – representing a hydrogen atom – leads wavefunctions with three quantum numbers n, l and m_l called principal, momentum and magnetic quantum numbers [23]. Each permitted combination of the three quantum numbers corresponds an atomic orbital in the hydrogen atom with capacity to hold two electrons of opposite spin. A combination of the spin quantum number with the aforementioned three quantum numbers fully specifies an electron in the hydrogen atom. Their range of values and relation to distinct notations relevant for photoemission are summarised in Tab. 2.1.

In its ground state the hydrogen atom only contains one electron in the lowest-energy $1s$ orbital. Increasing the number of protons in the nucleus we get a model for heavier hydrogen-like atoms (atoms containing only one electron) such as He^{+}, Li^{2+}, Be^{3+}, etc. As this merely involves a scaling of the potential energy term in Eq. 2.2, the analytical solution of the hydrogen atom scaled by the number of protons remains valid for hydrogen-like atoms. It is only when the number electrons in an atom is increased that the analytical model becomes inaccurate. This is because simply filling up the orbitals of a hydrogen-like atom following the Pauli-principle[5] does not take into account electron-electron interactions. Fortunately, the orbitals of multi-electron atoms are qualitatively similar to those of the hydrogen atom, and

[5]The Pauli exclusion principle states that no two electrons with the same spin can occupy the same state at the same time.

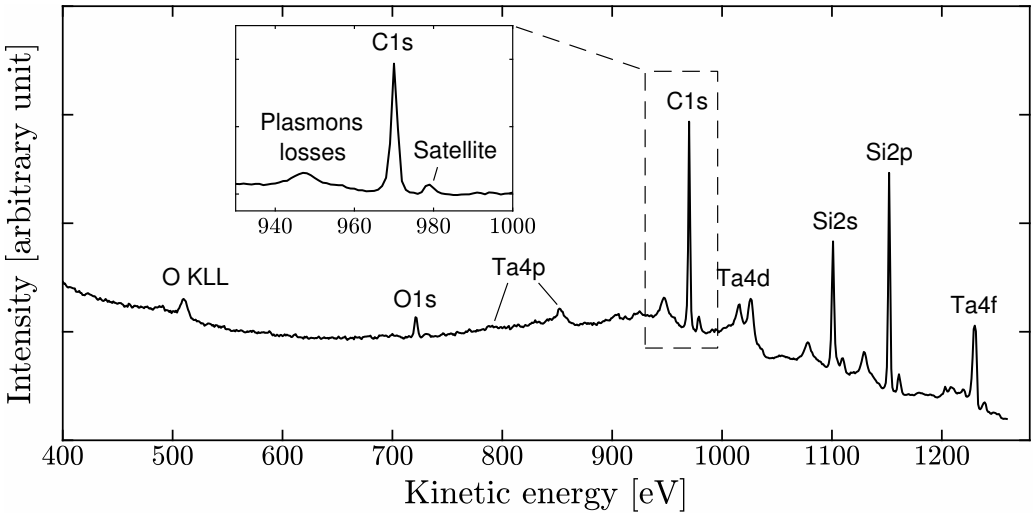

Figure 2.14: *Example of a widescan on a clean C-terminated SiC sample using a Mg Ka X-ray lamp ($h\nu = 1253.6\,\mathrm{eV}$). Direct photoemission peaks are labelled along with main Auger peaks, and some additional characteristic features.*

have the same quantum numbers which allows the notation from Tab. 2.1 to be used for all atoms.

Features of an XPS-spectrum

Although the main objective of photoemission techniques is to probe the electronic states, or more precisely the density of states of the sample, not all detail in an XPS spectrum correspond to real features of the electronic structure. Fig. 2.14 shows an example of an XPS survey spectrum, here forth *widescan*, of a carbon-terminated clean SiC sample with various features labelled. Following Ref. [40], the most prominent features can be summarized as the follows.

Direct photoemission peaks These photoemission peaks are attributed to electrons excited by the main line of photons from the X-ray source, ejected into vacuum and detected without incurring any energy loss. Their energy is hence given by Eq. 2.29, and can be directly translated into electron binding energy. They generally make up most of the detail in an XPS spectrum, and are used for identification and quantification of elements and molecules. They are labelled as C1s, Si2p, etc. denoting the atomic orbital they originate from.

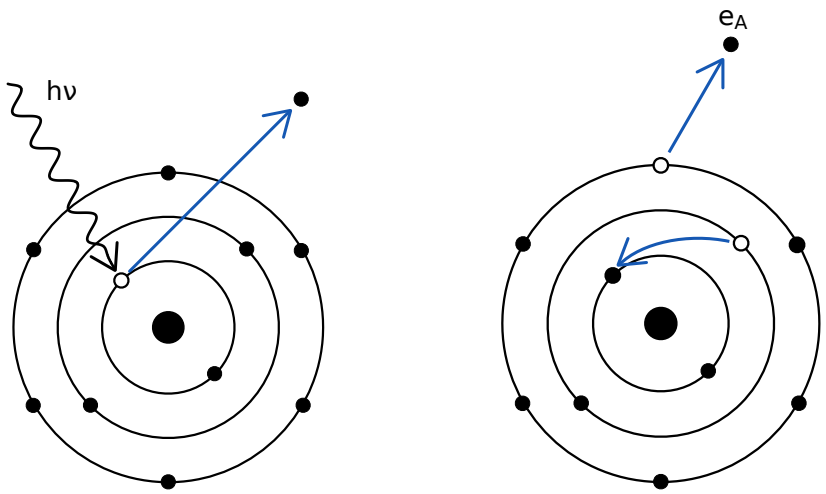

(a) Photoemission *(b) Auger-electron emission*

Figure 2.15: *Electron emission processes in photoemission spectroscopy.*

Auger emission peaks *Auger electrons* [pronounced *oh-zhey*] are produced in a three electron -process as a biproduct of photoexcitation as illustrated in Fig. 2.15. The excitation of a primary electron leaves an empty low energy state that is quickly filled by relaxing an electron from a higher energy orbital. The transition energy released in the process can be dissipated in form of an emitted photon, or less commonly a third electron called an Auger electron. Unlike primary electrons, the energy of an Auger electron is determined by the energy difference of the initial and final states of the relaxed electron, and is therefore not related to the X-ray energy;

$$\mathrm{KE}_A = \mathrm{BE}_1 - \mathrm{BE}_2 - \mathrm{BE}_3 - \Phi_s \tag{2.30}$$

where $\mathrm{BE}_{1\text{-}3}$ are the binding energies of the primary, relaxed and Auger electrons. As three electrons are involved in the emission of an Auger-electron, Auger peaks are denoted in X-ray notation (see Tab. 2.1) as for example O KLL referring – reading the letters backwards – to an Auger electron from the oxygen L-shell ($n = 2$) emitted in the relaxation of another electron from an L to a K shell orbital. The choice of different notation for primary photoemitted and Auger electrons stems from historical reasons.

Chemical shifts The exact binding energy of photoemission peaks is not only dependent on the source atom but also its chemical environment. For this reason XPS was at first called "electron spectroscopy for chemical analysis (ESCA)" by its

developer Kai Siegbahn. Chemical shifts are small shifts in the binding energy of core electrons as a result bonding or doping. This can be caused by an initial or final state effect. In the former the orbital energy of the actual emitted electron is dependent on the chemical state, while in the latter the chemical environment affects the rearrangement of remaining electrons after a photoemission process, hence influencing the total energy given to the emitted electron. In both cases chemical shifts are useful for identifying elements in different chemical environments in a sample. Chemical shifts tend to be particularly sensitive to differences in oxidation state.

Spin-orbit splitting Spin-orbit splitting is an effect that occurs in degenerate atomic orbitals with angular momentum different from zero, i.e. $m_l \neq 0$, and can be observed as splitting of the photoemission peak corresponding to a single atomic orbital into two components. This occurs because of an interaction between the electron spin and orbital angular momentum. When an electron is photoexcited an unpaired electron remains, leaving a total spin $s = \pm 1/2$ in the orbital. In degenerate orbitals this spin can interact with the orbital angular momentum either in parallel or anti-parallel, adding up to a total angular momentum $j = l \pm 1/2$. Due to different energies of the final state of the system in these two cases the energy transferred to the photoemitted electron varies, and two peaks are observed. The ratio of the areas of the peaks are proportional to the number of electrons in each degenerate level, and is given by

$$r = \frac{2(m_l + s) + 1}{2(m_l - s) + 1}. \tag{2.31}$$

Plasmon losses Plasmon loss peaks are small additional peaks on the lower kinetic energy side of a direct photoemission peaks. They are caused by quantized loss processes in photoionized electrons before leaving the sample surface, and therefore often consist of multiple peaks at equal spacings. Two common loss mechanisms can be identified. Intrinsic losses are caused by coupling between the hole created in the photoexcitation process and valence electrons in the atom resulting in less energy transferred to the photoexcited electron. Extrinsic losses include coupling of an electron travelling toward the sample surface with quantized excitations of valence or conductions electron in the sample, leading to loss of energy.

Satellites Satellites arise due to non-monochromatic components of the X-ray source at lab conditions. Conventional twin-anode sources have high resonance at

one emission line, however other X-ray lines are also present. Non-preferential X-rays are attenuated by a thin aluminium window, but are still present in the beam illuminating the sample and produce shifted low-intensity photoemission peaks.

Secondary electron spectrum Multiple scattering processes and other loss mechanisms ultimately cause many electrons to lose information about their origin, and contribute to a continuum of secondary electrons.

The inelastic mean free path

As X-rays tend to travel relatively deep into materials without significant attenuation, electrons throughout the sample are excited in the photoemission process and the surface sensitivity of photoemission techniques is governed by the depth from which electrons can escape the sample. As in XPS quantification one is generally interested in direct photoemission peaks, the relevant measure of this depth is given by the inelastic mean free path (IMFP) of electrons not having lost any energy in inelastic collisions, and thus possessing distinct kinetic energies related to their binding energy.

The inelastic mean free path of electrons with a given energy travelling through a given material is an empirical quantity, and there is no model that accurately generalizes the IMFP over for various materials or kinetic energies. With that in mind, the IMFP tends to be quite sensitive to fine material properties such as phase or impurities. For that reason, in the scope this project an empirical best-fit model of the inelastic mean free path λ is used [41, Eq. 5] given by

$$\lambda = \frac{1430}{E_k^2} + 0.54\sqrt{E_k} \tag{2.32}$$

where E_K is the kinetic energy of the electron. The advantage of such a simple formula is its ease of use, consistency and elimination of the systematic error arising from using values of λ measured by different means.

Photoionization cross-section

The *photoelectric effect* is an interaction between a photon and an electron bound in an atom. Through its course the photon energy is absorbed by the electron which is ejected from the atom with the kinetic energy

$$E_K = h\nu - E_b - \phi_S \tag{2.33}$$

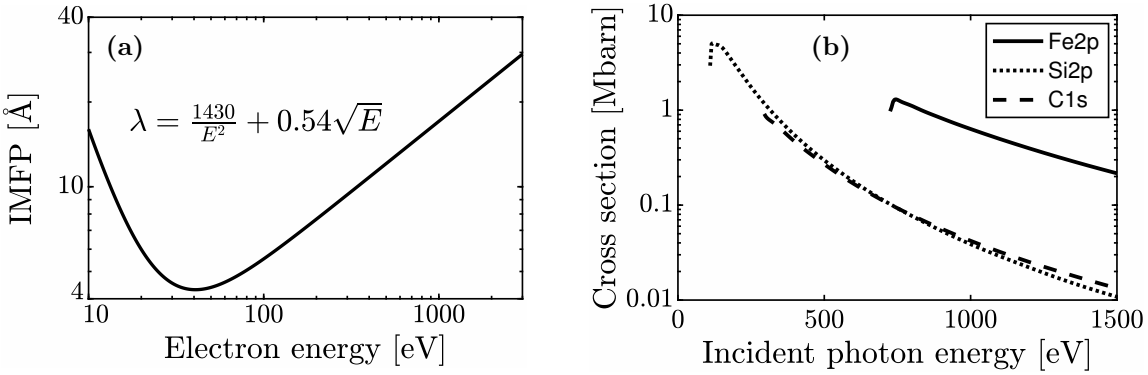

Figure 2.16: ***(a)*** *So called 'universal curve' for the inelastic mean free path of electrons through materials as a function of electron energy [41].* ***(b)*** *Photoemission cross-sections for C1s, Si2p and Fe2p electrons as a function of photon energy.*

where h is Planck's constant, ν is the photon frequency, ϕ_S is the work function of the sample and E_b binding energy of the electron.

The photoelectric effect is most prominent at low photon energies, slightly above the binding energy of the emitted electron. The probability of the interaction between a photon and an electron is expressed in terms of the photoemission cross section

$$\sigma = \frac{R}{\Phi N} \tag{2.34}$$

where R is the reaction rate inside a unit volume of target material, Φ is the incident photon flux and N is the atomic density. The total photoelectric effect cross section generally increases as a function atomic number due to more electron shells to interact with, and a higher probability of interacting with electrons in outer shells. An approximate empirical formula estimating the total photoemission cross section [42] is given by

$$\sigma = \text{const} \times \frac{Z^n}{E^{3.5}} \tag{2.35}$$

where Z is the atomic number of the atom, E is the energy of the X-ray and n is a constant between 4 and 5. The photoemission cross section for 1s electrons in carbon and 2p electrons in silicon and iron are shown in Fig. 2.16b [43].

Quantitative analysis

In the analysis of XPS spectra we are interested in attributes of direct photoemission peaks such as their area, the binding energy of its components and the shape of the

peak. For quantitative analysis, in particular changes and ratios of peak areas and relative chemical shifts are the most interesting as absolute values tend to be highly dependent on sample alignment, transmission function, etc.

The spectral width of photoemission peaks arises from several factors such as the line shape of the incident photon flux, the resolution of the electron analyser, thermal Doppler broadening and the core-hole lifetime. The first three factors are often assumed to have Gaussian profiles with the dominant contribution coming from the spectral width of the photon flux, while the core-hole lifetime results in Lorentzian broadening [44]. A common line shape to fit to direct photoemission peaks is therefore a Voigt profile which is given by the convolution of a Gaussian and Lorentzian function with spectral widths σ and γ respectively

$$\mathrm{V}\left(x; x_0, \sigma, \gamma\right) = \int_{-\infty}^{\infty} \mathrm{G}\left(x' - x_0; \sigma\right) \mathrm{L}\left(x - x' - x_0; \gamma\right) \mathrm{d}x' \tag{2.36}$$

The Voigt-profile has no analytical form, and in practice often a pseudo-Voigt function is used to represent $\mathrm{V}\left(x; x_0, \sigma, \gamma\right)$ in order to avoid computing the integral in Eq. 2.36 numerically at each iteration of curve fitting. One commonly used pseudo-Voigt function is given by a normalized sum of Gaussian and Lorentzian functions using the mixing parameter suggested by Thompson *et al* [45, Eq. 2-3], accurate to 1.2% [46].

Electrons originating from metallic atom orbitals tend to undergo additional energy-loss processes when excited through the high density of states Fermi-level which leads to an asymmetry in the peak profile on the low kinetic energy side. The Voigt-profile gives a poor fit to such peaks and asymmetric line-shapes are typically used. A common asymmetric peak profile with theoretical backing is suggested by Doniach and Sunjic [47]

$$\mathrm{DS}(x; x_0, \alpha, F) = \frac{\cos\left[\frac{\pi\alpha}{2} + (1-\alpha)\tan^{-1}\left(\frac{x-x_0}{F}\right)\right]}{\left(F^2 + (x-x_0)^2\right)^{\frac{1-\alpha}{2}}} \tag{2.37}$$

where α is the asymmetry parameter between 0 and 1, F is related to the width and x_0 to the position of the peak. The disadvantage to using the Doniach-Sunjic peak shape is that its fitted parameters are not directly comparable to the fit parameters of a Voigt-profile. Moreover, for $\alpha > 0$ the integral of Eq. 2.37 diverges which necessitates the definition of an arbitrary energy cut-off for normalizing the peak intensity. The way such a cut-off is defined impacts the relative measured intensities of peaks with different asymmetry parameters, and the especially the relative intensity of peaks fitted with Voigt- and Doniach-Sunjic lineshapes. In this thesis a cut-off of $5F$ is defined on each side of x_o.

In additional to the peak profiles a correct treatment of the secondary electron background is necessary for realistic fit parameters. In this project a Shirley-type background [48] was used consisting of a step function centered at the position of each peak component x_0

$$\mathrm{S}(x; x_0, W) = \mathrm{erf}\left(\frac{x_0 - x}{W}\right). \tag{2.38}$$

where W is the width equal to the pseudo-Voigt width [45, Eq. 3] or the Doniach-Sunjic width F. The Shirley background arises from inelastic scattering of electrons originating from each photoemission peak, and is used in conjugation with an additional constant offset or linear background.

Layer modelling

One application of qualitative analysis on XPS spectra is using photoemission peak areas to determine the thickness of a thin film deposited on a sample of a different material. One can derive a simple expression for the thickness of an overlayer on a substrate knowing the electron inelastic mean free path λ and photoemission cross sections of the two materials σ. The Beer-Lambert law gives the attenuation in the intensity of electrons travelling a distance d through the sample

$$I = I_0 e^{-\frac{d}{\lambda}}. \tag{2.39}$$

The number of electrons per unit of time ejected to vacuum from a volume $A\Delta x$ at depth x within a sample is given by

$$\Phi = I_{phot} n \sigma A e^{-\frac{x}{\lambda}} \Delta x \tag{2.40}$$

where I_{phot} is the incident photon intensity and n is the atomic density of the material. As X-ray attenuation is negligible at the scale of λ, we have approximated the photon intensity constant as the function of depth. The total flux of electrons emitted from an overlayer film of thickness d is then found

$$\Phi_o = I_{phot} \int_0^d n_o \sigma_o A e^{-\frac{x}{\lambda_o}} \,\mathrm{d}x = I_{phot} n_o \sigma_o A \lambda_o \left[1 - e^{-\frac{d}{\lambda_o}}\right]. \tag{2.41}$$

Similarly we can find the flux of electrons emitted from the underlying substrate. The ratio of the electron intensity emitted from the substrate and overlayer is then given by

$$\frac{I_o}{I_s} = \frac{n_o \sigma_o \lambda_o}{n_s \sigma_s \lambda_s} \frac{1 - e^{-\frac{d}{\lambda_o}}}{e^{-\frac{d}{\lambda_o}}} \tag{2.42}$$

Assuming similar atomic densities and inelastic mean free paths in the two materials, Eq. 2.42 can be rearranged to find the thickness d of the overlayer

$$d = \lambda \ln\left(1 + \frac{\sigma_s I_o}{\sigma_o I_s}\right). \tag{2.43}$$

Ultraviolet photoelectron spectroscopy

Ultraviolet photoelectron spectroscopy (UPS) is a variant of PES in which a lower energy photon source is used to excite low binding energy electrons, typically from the valence band of a sample. Much like XPS it gives information related to the density of states at the sample surface. Using an ultraviolet light source for valence band mapping has the advantage over X-rays of having higher photoemission cross sections for valence band electrons, and easier production of high-intensity UV light [39]. It is also more suitable for angle-resolved photoemission spectroscopy (ARPES) as the lateral dispersion of electrons from states with distinct wavevectors is larger.

Mapping the valence band structure of a material gives complementary information to XPS data. While the latter is more suitable for elemental analysis, since the behaviour of valence band electrons is dominated by bonding with neighbouring atoms the valence band spectrum of a material gives information related to the electrical properties of the sample. A distinct difference between metals and insulators is evident in valence band spectra. In metals states exist up to the Fermi-level where a sharp drop of intensity is observed with the shape of the Fermi-Dirac distribution, while in insulators and semiconductors the Fermi-level is in a band gap, and therefore the intensity of spectra vanishes before reaching the Fermi-level. ARPES gives information not only about the density of states, but also the dispersion of the energy of states in k-space. ARPES can therefore be used to reconstruct the band structure of materials such as the ones shown for SiC and FeSi in Fig. 2.11.

2.4.2 Low-energy electron diffraction

Low-energy electron diffraction (LEED) is based on the Bragg-reflection of low-energy electrons from a single crystalline surface. The de Broglie wavelength λ of a particle is given by

$$\lambda = \frac{h}{\sqrt{2mE}} \tag{2.44}$$

where h is Planck's constant, and m and E are the particle mass and kinetic energy. For electrons with energy $\sim$ 10 - 200 eV this corresponds to wavelengths of the order of 1 - 4 Å, which is comparable to the spacing of atoms in a solid.

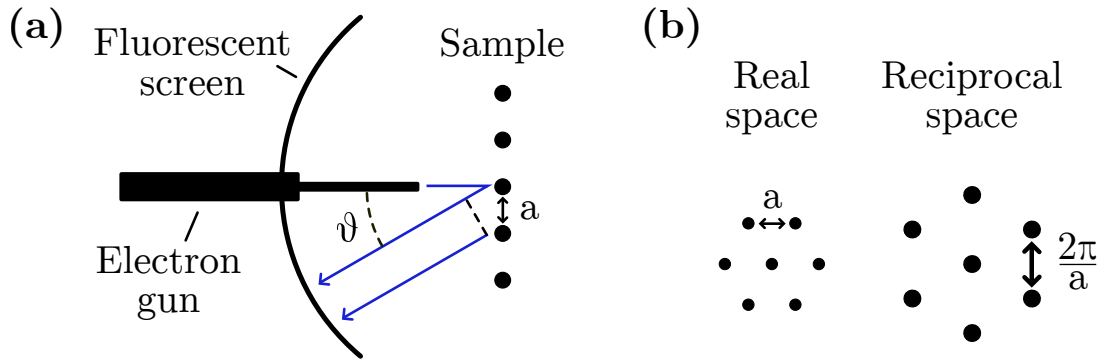

Figure 2.17: *(a) Low-energy electron diffraction setup demonstrating the Bragg-condition.* ***(b)*** *Hexagonal 2D lattice and its reciprocal lattice which is also a hexagonal lattice, rotated by* 90°*.*

A LEED instrument is typically placed in UHV where the electron attenuation is low. Fig. 2.17a shows a typical instrument setup. An electron gun emits electrons onto a sample with typically high crystalline order. The electrons are scattered by the crystal, and the interference of back-scattered electrons forms an interference pattern on a fluorescent screen.

Much like in PES the surface sensitivity of LEED is dominated by the strong interaction of electrons with matter which results in that only the top few atomic layers of a material are probed. As there are no diffraction elements perpendicular to the surface, the diffraction pattern formed in LEED is the reciprocal lattice of the two-dimensional lattice of atoms at the sample surface. In Fig. 2.17b the diffraction pattern of a hexagonal lattice is shown, which is also a hexagonal lattice rotated by 30°. LEED provides valuable structural information about the sample and surface reconstructions, and is often integrated into an XPS system.

Chapter 3

Equipment and apparatus

The final section of Chapter 2 gave an overview of the experimental techniques applied in this thesis from a theoretical point of view. In this chapter a more practical perspective of photoemission spectroscopy and processing in ultra-high vacuum is provided. As minimizing contamination is crucial for attaining good results in an UHV experiment, the content of this chapter is imperative for understanding the experimental methods and results in this thesis. Furthermore, since large parts of the duration of this thesis was spent at the lab learning about such practices, it is an integral part of this work and an indispensable reference for a newcomer in X-ray physics.

3.1 Ultra-high vacuum

Ultra-high vacuum (UHV) is as suggested by its name very low-pressure vacuum, often defined in the range $10^{-7} - 10^{-12}$ mbar [49]. UHV is achieved in laboratory conditions inside a vacuum chamber by using pumps. The most common use of UHV is in scientific research applications such as surface or particle physics, requiring a high mean free path of particles inside the chamber. The mean free path of molecules is inversely proportional to pressure, and typical values in UHV conditions is of the order of 1-10^5 km [49], not counting the collisions with the chamber walls of course.

Doing experiments in UHV significantly complicates and prolongs the processing steps compared to ex situ processing. Therefore generally only experiments requiring UHV are performed at these conditions. One of the notable advantages of processing in UHV is the low rate of contamination. While a cleanroom can be used to eliminate most of the particulate contamination, the success of many experiments especially

in surface science is reliant on the performing controlled reactions in the absence of atmospheric gasses such as oxygen.

From the kinetic theory of gasses we can derive a simple relation for the flux of particles incident on the sample surface as a function of pressure. Pressure is defined as the force F a gas exerts on a surface of per unit area, where the force can be expressed as the derivative of the gas momentum normal to the surface by time

$$P = \frac{\partial n m v_\perp}{\partial t}.$$

Here n and m are the atomic density and mass of gas molecules, and $v_\perp$ is the normal velocity component. For inelastic collisions between the gas and the surface, the flux of particles incident on the surface per unit area can be expressed as

$$\Phi = \frac{P}{2m\bar{v_\perp}} \tag{3.1}$$

Assuming that the reaction of gasses with the surface is proportional to their flux we see that contamination rate of a clean surface in vacuum increases linearly with pressure. As a general guideline at a pressure of 10^{-6} mbar a sufficient amount of gas molecules are incident on a surface to form one monolayer of contamination per second [50].

For techniques based on the detection of electrons emitted from a sample such as PES or LEED ultra-high vacuum is a necessity due to the high dependence of electron mean free path on pressure – in atmospheric pressure most electrons would be absorbed after travelling a distance of a few nanometers, and would not make it to the detector.

3.2 Vacuum chamber

Degassing from and the permeability of gasses through many materials inside a vacuum chamber places strict constrains on the materials used to construct an UHV-system. Due to oxidation of carbon steel which increases its surface area, hence enhancing the adsorption of molecules, only stainless steel is used in the construction of a vacuum chamber. Due to the incompatibility caused by degassing of the majority of organic compounds such as plastics with UHV environments, single-use copper gaskets are used to ceil joints points between vacuum components. A photo of the home lab at NTNU is shown in Fig. 3.1.

The vacuum is maintained by various pumps running at all times to remove gas entering the chamber by degassing or permearing through chamber walls. After the

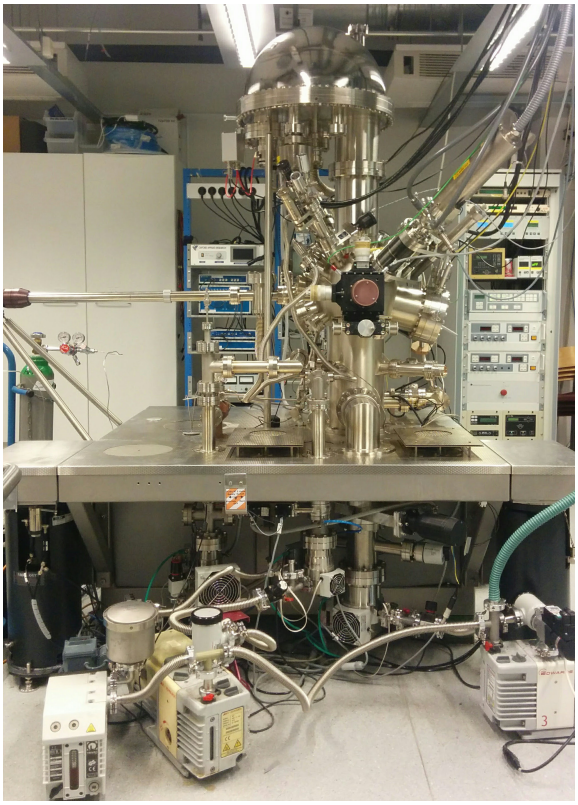

Figure 3.1: *Photo of NTNU Department of Physics XPS-lab showing a stainless steel vacuum chamber with various components attached to it. On the top is the hemispherical energy analyser. Sticking out on the left side and front are a magnetic arm and manipulator for sample transfer and alignment. Under the table several roughing pumps are visible backing the turbomolecular pumps.*

chamber has been introduced to ambient air it must be baked above 100 °C while pumping in order to remove water condense from the chamber. Most systems include an interlock, or loadlock, for introducing new samples without pumping down the main chamber. The loadlock can be pumped down separately to a moderate pressure before introducing the sample to the main chamber. Various parts of the UHV system are separated by gate valves for sample transfer using magnetic arms. In the main chamber the position of the sample can usually be controlled more accurately in a manipulator. The manipulator at the home lab used in this project allows sample alignment in x, y and z, and orientation θ in the angle orthogonal to z.

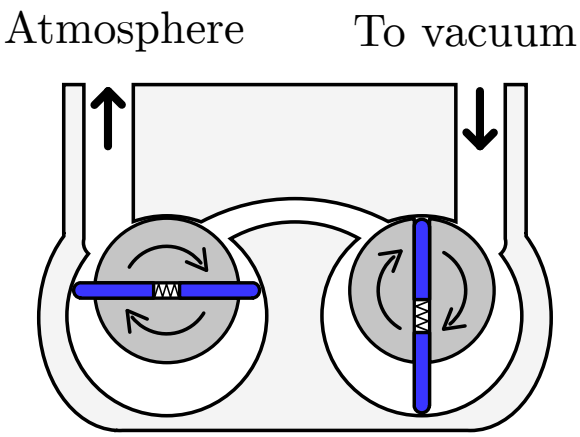

Figure 3.2: *Operation of a two-stage rotary vane pump.*

3.3 Pumping

Pump are used in an UHV-system to initially bring down the pressure, and subsequently to remove any gasses entering the chamber by degassing or diffusing through chamber walls. Various types pumps are necessary for maintaining the system which are reviewed in this section. Parts of the following discussion is taken from Ref. [49].

3.3.1 Roughing pump

Roughing pumps, also called backing pumps, are pumps used to for the initial evacuation of a vacuum system. They are typically mechanical pumps only able to pump down to the order of 10^{-3} mbar. They have an essential role in achieving ultra-high vacuum, as turbomolecular pumps (see following section) used to get down to high levels of vacuum generally cannot operate at 'rough vacuum' due to the transition from molecular to viscous flow. Therefore roughing pumps are placed behind such pumps to keep the pressure sufficiently low on both sides of the turbomolecular pump.

An important distinction between various forms of roughing pumps is whether the pump uses lubricating oil in the pumping volume. So called oil-sealed roughing pumps have the disadvantage compared to dry pumps is that traces of the oil can backstream into the vacuum causing contamination. Other differences in the pump design include effects aspects such as cost, lifespan and vacuum level achieved in the pump.

An example of a common mechanical pump used as a roughing pump is the rotary

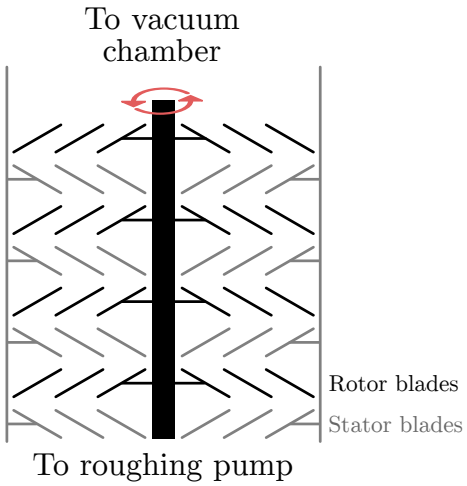

Figure 3.3: *Turbomolecular pump. Pumping action is achieved by several stages of fast spinning rotors. Typically an order of magnitude difference in pressure is achieved at each stage.*

vane pump. An example of a two-stage rotary pump is shown in Fig. 3.2. The rotary vane pump is an oil-immersed positive displacement pump. Each stage of the pump contains an cylinder with an eccentrically placed rotor. The rotor has vanes fitted into slots dividing the dividing the available inner space into working chambers. During the rotation of the rotor the volume of the working chamber expands and contracts, which achieves the pumping action.

3.3.2 Turbomolecular pump

A turbomolecular pump is a pump used to achieve ultra-high vacuum in vacuum chambers. It is based on the principle that gas molecules can be given momentum by repeated collisions with moving turbine blades. This principle only works at vacuum ranges where molecular low is the prominent form of gas flow, and therefore turbomolecular pumps cannot be used for pumping at atmospheric pressure and require a backing pump [51].

The design of a turbomolecular pump is shown in Fig. 3.3. The pumping is achieved at multiple stages of alternating spinning turbine blades separated by stationary stator blades. Due to the relative motion of the rotor and stator blades molecules preferentially hit the bottom of moving rotors, and are given momentum in the downward direction. At each stage of rotor blades an order of magnitude compression can be achieved, placing different requirements on blades along the gas

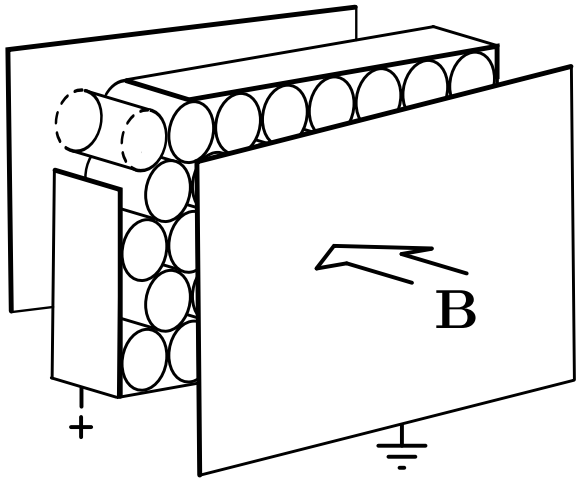

Figure 3.4: *Design of an ion pump. The anode is placed at a high potential between two grounded titanium cathode plates in the presence of a magnetic field. Electrons are emitted from the cathodes due to the potential difference, and are trapped in the anode cavities in a magnetron motion due to the magnetic field. Collision of electrons with gas molecules creates ions which are attracted to the cathodes, and impact with a high energy sputtering reactive titanium inside the pump. Figure was motivated by Ref. [49].*

line. Blades near the outlet of the pump are thicker and flatter to resist the high pressure, while blades near the inlet are thin and tilted 45° to maximize pumping action.

The pumping action of turbomolecular pumps is highly dependant on high spin speed of the rotors. This causes high friction build-up, which ultimately limits the performance of the pump due to build-up of heat. It also makes turbomolecular pumps volatile to intense vibrations or sudden exposure to high pressure, in which case blades can be bent and crash.

3.3.3 Ion pump

Ion pumps are different from conventional pumps in that they have no gas outlet – all particles removed from the vacuum chamber are stored inside the ion pump. Figure 3.4 shows an illustration of a common ion pump design. The following description is based on Ref. [49]. Two grounded cathode plates are placed on each side of a array of anode tubes kept at a high voltage. Strong ferromagnets are placed outside the ion pump resulting in a magnetic field through the pump.

The strong potential difference accelerates electrons from the cathodes toward

the anode in helical paths owing to the parallel magnetic field. As the electrons reach inside the anode they become trapped in a magnetron motion, and eventually collide with an atom ionizing it. The ion is repulsed by the high potential, and is accelerated toward the cathode which is made of a highly reactive material such as titanium. Upon collision the ion reacts with the cathode material and is deposited on the wall of the ion pump, at the same time sputtering several new titanium atoms off the surface. These titanium atoms will react with additional gaseous molecules forming compounds deposited on the anode.

Ion pumps are extremely useful in that they can eliminate gasses that turbo-molecular pumps can not, and lead to no backstreaming of organic contaminants reaching down to pressures around 10^{-11} mbar. They are also vibration free, and have long lifetimes. As all the gas is deposited onto the anode inside the ion pump they however cannot be used for high trough-put pumping as this would lead to excessive build-up of of contaminants, and shorten the ion pump lifetime. In addition due the high potential difference between the cathodes and anode, high pressure can generate sparks which create problems for vacuum chamber electronics.

3.3.4 Titanium sublimation pump

The titanium sublimation pump is somewhat similar to the ion pump. It uses the reactivity of titanium to trap gasses on the chamber surface. Titanium sublimation pumps operate by the evaporation of a titanium atoms from a Ti-Mo alloy wire by means of passing a current through it. The titanium atoms form a thin clean layer on the chamber surface reacting with gasses incident on the surface, thereby trapping them. Titanium sublimation pumps use up the Ti-Mo wire at rates of the order of $100\,\mathrm{mg\,h^{-1}}$, and thereby have a limited lifetime. They are hence used in combination with the aforementioned pumps, and titanium is only periodically evaporated.

3.4 Photon sources

Electromagnetic radiation in the ultraviolet and X-ray energy range have been shown to be an effective means of exploring the properties of matter in many fields of science. The exact requirements on wavelength and intensity are determined by the properties of the sample probed. Multiple sources of electromagnetic radiation are used in photoemission techniques, with the two types outlined in this section are the twin anode X-ray source for XPS and gas discharge lamp for UPS found at the home laboratory. Another common radiation source is synchrotron source, based

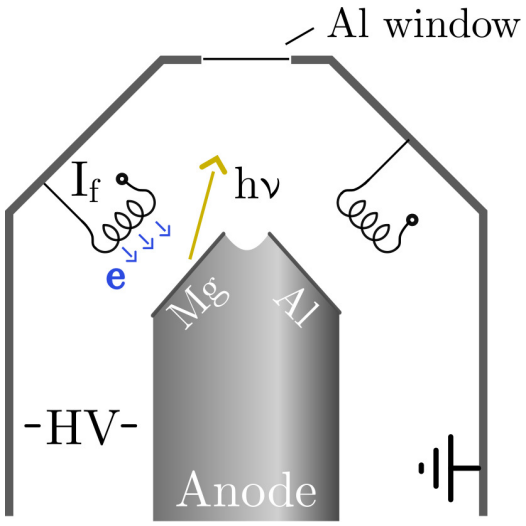

Figure 3.5: *Operation of a twin anode X-ray source. Electrons are emitted by a tungsten filament, and attracted toward the anode due to a large potential difference. Impact into the anode creates X-rays with energies characteristic to electronic transitions inside the anode material.*

on radiation emitted from charges moving in a circular trajectory inside a particle accelerator. These photons are filtered using a monochromator providing a high intensity monochromatic beam of photons for beamlines at the synchrotron facility.

3.4.1 Twin anode X-ray source

X-rays are are highly useful for probing the core levels of elements due to their high photoionization cross section combined with a relatively low cross section for valence band electrons. Additionally, core level electrons excited by typical X-ray sources typically have energies corresponding to the minimum of the 'universal curve', leading to enhanced surface sensitivity.

Twin anode sources are common X-ray sources at home laboratory conditions providing a medium intensity of X-rays with a strong monochromatic component. The source is based on the inverse process of the photoelectric effect. The design and operation of the twin anode source is illustrated in Fig. 3.5. A cathode filament, typically made of tungsten, is heated by a current and emits electrons in a thermionic emission process. The electrons are accelerated toward an anode at a high positive voltage, and impact producing X-rays. Typical anode materials include Mg and Al [39]. The cathode filament and anode are placed inside a grounded housing

evacuated from air. As a lot of energy is dissipated at the anode due to the impact of high energy electrons, the maximum capacity of the source is limited by how much the anode can withstand. Therefore water cooling at the anode is necessity.

Vacuum is necessary inside the X-ray source in order to allow free movement of electrons from the filament to the anode without collision with gas molecules. This is also useful for preventing sparks between the electrodes. A dual design is adopted in order to have two choices of anode material. Each anode emits X-rays at a characteristic energy depending on electronic transitions in the element. In magnesium and aluminium these are the 2p to 1s orbital transitions corresponding to X-rays emitted at 1253.6 eV and 1486.6 eV respectively [39]. The availability of two photon energies is useful as it allows the movement of Auger relative to direct photoemission peaks in case of an overlap.

3.4.2 Gas-discharge lamp

For valence band mapping it is often preferential to use a lower energy photon source. This is because photoemission cross-sections are generally higher at lower excitation energies [40]. Ultraviolet light is often sufficient to excite electrons from most of the valence band in techniques called ultraviolet photoelectron spectroscopy (UPS).

Ultraviolet light can be produced in gas discharge lamp. The lamp consists a glass capillary containing a noble gas with electrodes on each side. As a current is applied across the gas, electrons are accelerated from the cathode to the anode. Their energy is transferred to gas atoms in inelastic collisions, leaving the atoms in an excited state. The atoms eventually relax emitting ultraviolet light. The energy of the photons emitted is dependent on the atomic transitions in the gas. At the NTNU home lab ^{3}He gas is used with two main emission lines He-I at 21.22 eV and He-II at 40.81 eV using the *Specs UVS 10/35* UV lamp.

Due to the high attenuation of ultraviolet light in most materials, in order to get ultraviolet light inside the vacuum chamber the end of the capillary must be open to the vacuum leading to a leak of ^{3}He inside the chamber. The leak is minimized by using a very small hole in the capillary along with two stage differential pumping. The resulting beam of ultraviolet light is a small spot with diameter ~ 2 mm on the sample.

3.5 Hemispherical energy analyser

The most important component of an XPS-setup is the system used for collecting and detecting photoemitted electrons. This is usually achieved by means of focusing

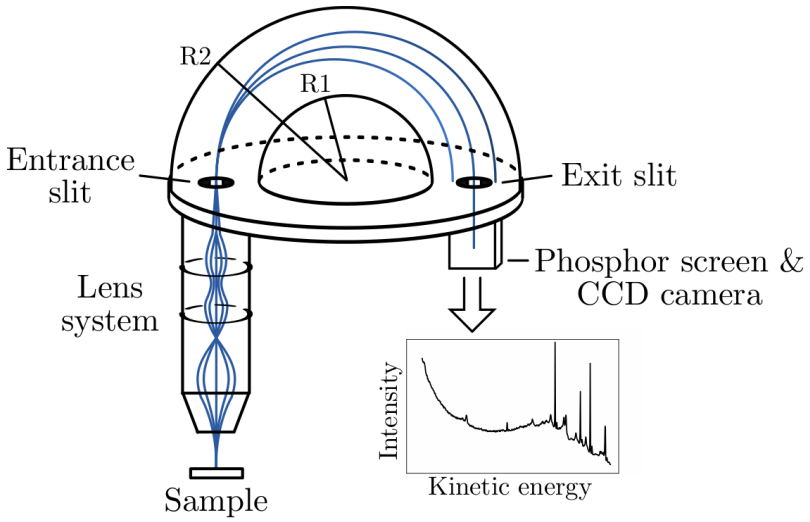

Figure 3.6: *Electron detection in with a hemispherical energy analyser. Electrons emitted from a sample are focused by electrostatic lenses, and passed between concentric hemispheres with an applied potential difference. Electrons with kinetic energy equal to the pass energy of the analyser travel along the central arc of the analyser and make it through the exit slit for detection.*

the electrons using electrostatic lenses and passing them through an energy analyser into a detector. Both focusing by the lenses and the operation of the energy analyser depend on the requirements on the spacial and angular resolution of the system, and different types of energy analysers are commercially available. In this section the operation of a traditional hemispherical energy analyser is outlined following the manual Specs manual Ref. [52].

A hemispherical analyser consists of a two concentric hemispheres set at a voltage difference, see Fig. 3.6. Electrons enter trough an entrance slit and are deflected by the electric field in a circular path. As electrons travelling at different velocities will travel in paths of different radii, the beam will disperse, and only electrons with kinetic energy equal to the pass energy of the system will exit through the exit slit. The pass energy E_p of the analyser is given by

$$E_p = -q\Delta V \left(\frac{R_1 R_2}{R_2^2 - R_1^2} \right) \tag{3.2}$$

where q is the electron charge, ΔV is the applied potential between the inner and outer hemispheres and $R1$ and $R2$ are the inner and outer radii of the analyser.

In XPS the analyser is generally run in fixed analyser transmission mode. This

means that the pass energy of the analyser is kept constant, and energies are scanned by applying a varying retarding potential prior to the electrons entering the analyser. This mode is preferential as the energy-resolution of the analyser is dependent on the pass energy given by

$$\Delta E_a = E_p \left(\frac{S}{2R_0} + \frac{\alpha^2}{4} \right) \tag{3.3}$$

where S is the mean of the entrance and exit slit widths $S = (S_1 + S_2)/2$ and α is the half acceptance angle of the detector. Similarly the intensity of the detection system is generally proportional to the square of the pass energy

$$I \sim \frac{E_p^2}{E_k}. \tag{3.4}$$

In order to achieve a high resolution low pass energies must be used. This is the case when scanning over individual photoemission peaks. When doing widescans high energy resolution can be sacrificed for intensity, and generally higher pass energies are used.

When analysing data from a detector it should be taken into account that also the efficiency at which the lens system delivers electrons to the analyser is dependent on the electron kinetic energy. The resulting changes in intensity are accounted for in the detector *transmission function*, which should be used to correct the counts measured by the detector prior to further data analysis.

Various forms of detectors can be mounted at the exit slit of the analyser. Traditionally channeltron detectors have been preferred due to their high efficiency and lifetime. Mounting a single detector at the exit slit however has the disadvantage that only electrons at the central path can be detected, and electrons deviating slightly in energy are lost. Position sensitive detectors detect electrons along the dispersion axis of the analyser, and utilize the entire flux of electrons from the exit slit without loss in resolution. In this project a *Specs Phoibos 150* energy analyser was used in combination with a phosphor detector and a CCD camera for electron detection.

3.6 Ultra-high vacuum processing

Due to the high surface sensitivity of photoemission techniques, exceptional care must be taken in the preparation of samples for good results. This involves working with high-quality materials and atomically clean surfaces. As working in situ eliminates many sources of contaminants, in situ sample preparation can often improve and is sometimes a must for satisfactory results. In this project two types of processing

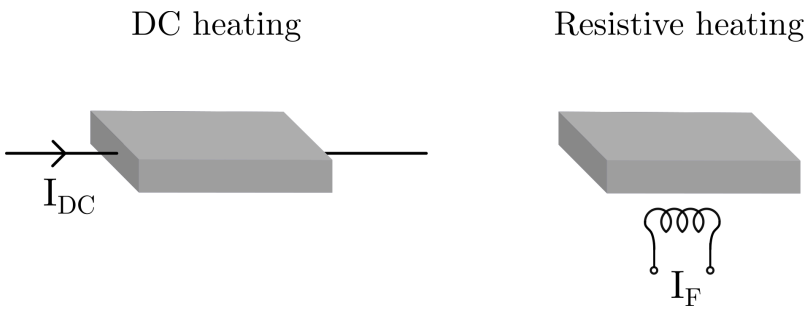

Figure 3.7: *In situ direct current and resistive heating.*

steps were done in situ, namely sample heating and the deposition of metals, which are both outlined here.

3.6.1 Sample annealing

In situ sample annealing is required for degassing samples after loading to wipe out contaminants, and is a necessary step in the formation of graphene. There are two ways of achieving this illustrated in Fig. 3.7. In direct heating a current is passed through the sample where power is dissipated owing to its resistance, heating up the sample. In resistive heating the current is passed through a filament adjacent to the sample, heating up the filament. The advantage of direct current heating is that higher sample temperatures can be reached, however the sample must be sufficiently conductive in order to pass significant current through it. Similarly, it must be sufficiently resistive to dissipate enough power without using too large currents.

3.6.2 Metallization

In situ deposition of metals is useful to avoid oxidation of the metal in atmospheric pressure. Two methods for depositing metals were used in this project. Electron beam evaporation is based on bombarding a target anode with electrons emitted by a tungsten filament. The electron beam causes the target material to be transformed in a gaseous state, and is deposited over everything within line-of-sight inside the vacuum chamber. The *EGCO4 Mini e-Beam Evaporator* was used for iron deposition in this project.

The other method used for depositing metals is thermal evaporation. This involves heating a target metal to sublimate it, depositing over adjacent surfaces. Thermal evaporation is typically done passing a current through a filament or coil with a high melting temperature wrapped around the target material.

Chapter 4

Methods

In the following chapter details of the experimental and computational methods related to this project are presented. A substantial part of the work has been devoted to processing and characterization in ultra-high vacuum with the goal of studying the reaction between iron and silicon carbide to form graphene on iron silicide, and ultimately producing a patterned graphene Hall bar.

Since several attempts to grow graphene were made with multiple samples produced, for the convenience of the reader the experimental procedure is presented with focus on distinct processing steps rather than given as a chronological outline of the processing of each sample. First the growth and characterisation of samples in ultra-high vacuum is described. In the following section an overview of additional characterization using techniques of microscopy and Raman spectroscopy at the NTNU NanoLab is given. Electrical measurements performed on the final Hall device are described in Sec. 4.4, and Sec. 4.5 outlines the computational procedure using SIESTA for supporting experimental results.

4.1 UHV growth and characterization

The UHV procedure described in this section took place at the Department of Physics XPS-lab at NTNU. Multiple attempts to grow graphene on metal-treated SiC were carried out, however several samples could not be completed due to difficulties with the instrumentation or human error. Three successful samples were produced, and in this section primarily the procedure for producing and characterising the latest two samples A and B illustrated in Fig. 4.1 is provided.

The purpose of the experiments on SiC were threefold: **(1)** to study the formation

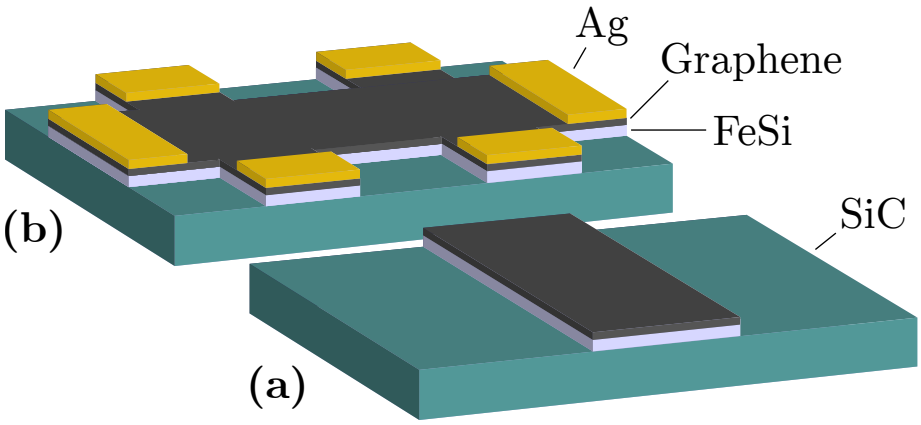

Figure 4.1: *Illustration of two graphene patterned SiC samples fabricated in the course of this project.* ***(a)*** *A strip of graphene on SiC for spatially resolved XPS measurements (sample A).* ***(b)*** *Graphene patterned Hall bar for electrical measurements (sample B).*

and characteristics of graphene and the iron silicide interlayer on SiC, and assess the system's suitability for the fabrication of a radiation sensor, **(2)** to determine the suitability of the growth method for patterned formation of graphene, and **(3)** to fabricate of a Hall bar for electrical measurements by selective formation of graphene on SiC. Each sample was produced with the partial goal of realizing objective **(1)**, while objectives **(2)** and **(3)** were directly addressed in the fabrication of samples A and B.

Rough UHV processing steps used for graphene growth can be summarized as the following.

1. Sample preparation and transfer into vacuum
2. Overnight degas and flash to $\sim 700\,^{\circ}\mathrm{C}$
3. Iron deposition
4. Sample anneal to $> 600\,^{\circ}\mathrm{C}$
5. Transfer out of vacuum chamber

XPS and in some cases UPS measurements were performed generally after steps 2, 3 and 4, and LEED patterns of clean SiC and SiC after graphene growth were obtained. The following sections give a more detailed overview of the steps for graphene growth, characterization, and the fabrication of graphene devices.

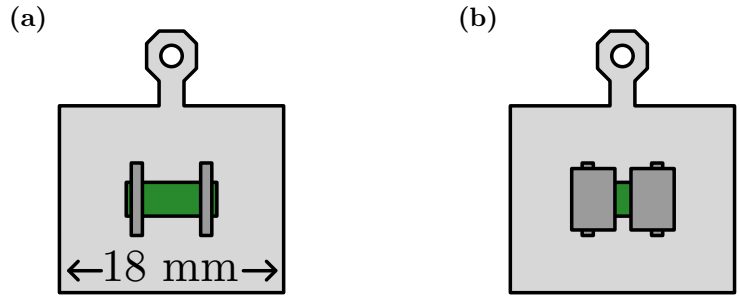

Figure 4.2: ***(a)*** *Normal sample mounting using Ta clips.* ***(b)*** *Sample mounting with additional Ta foil masks to create the stripe pattern for sample A in Fig. 4.1a.*

4.1.1 Sample preparation

A tantalum sample holder was cleaned using sandpaper to remove visible contaminants from previous experiments. Prior to mounting the SiC sample on the sample holder using strips of Ta-foil, each item was cleaned separately by the following recipe. First the items were thoroughly rinsed in a stream of acetone from a squirt bottle. The items were then immersed in separate beakers of acetone, and placed in an ultrasonic bath for 10 min. The items were then transferred to ethanol for another 10 min ultrasonic bath. Finally the items were dried in a stream of nitrogen at a large angle to blow away traces of ethanol.

Once cleaned, SiC samples were placed polished face up on the sample holder, and fixed by placing strips of Ta-foil over each side of the sample spot welded onto the sample holder. This is illustrated in Fig. 4.2a. Samples A and B were loaded with additional masks made of Ta foil shown in Fig. 4.2b and 4.5a respectively. The sample was then transferred into the vacuum chamber.

Samples were degassed by heating in UHV. Although temperatures up to 1050 °C are required to fully remove the native oxide layer on SiC [53], as in situ direct current heating was not working at the time of this project resistive heating was used up to a maximum of $\sim 700\,^{\circ}\mathrm{C}$. Common procedure for all samples included degassing overnight at 300 °C followed by a flash to 710 °C for 10 min. Ramp and cool rates above 300 °C were kept manually around $0.5\,^{\circ}\mathrm{C\,s^{-1}}$. Pressure was monitored during degas, and was generally kept below 5×10^{-9} mbar.

Once sample temperature had recovered to below 50 °C XPS-spectra of 'clean' SiC were generally taken. Procedure for sample alignment is overviewed in Sec. 4.1.3. The evolution of the C1s XPS peak at three stages during sample degas is shown in Fig. 4.3 showing a high attenuation of oxidised carbon as a result of the heat treatment. The corresponding total measured intensity of the O1s peak decreased

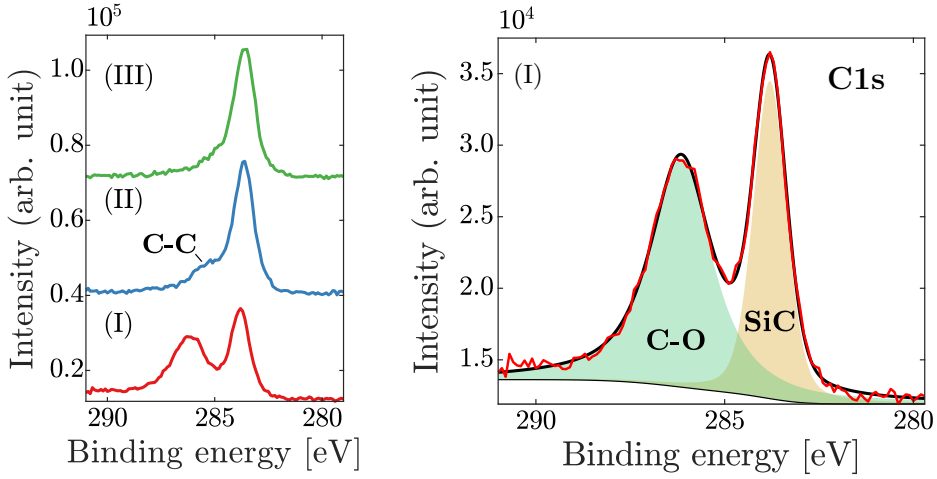

Figure 4.3: *Changes in the C1s core level during SiC degas. On the left the peak is shown at three stages (I) before degassing, (II) after overnight degas at* 300 °C *and (III) after* 10 min *flash to* 710 °C*. On the right the first peak deconvoluted for carbon in oxygen and silicon rich chemical environments is shown. The figure shows complete disappearance of the oxygen rich component during overnight degas, and the attenuation of the C-C component after the high temperature anneal.*

from 100% to 77% after overnight degas and 48% after flash to 710 °C.

4.1.2 Graphene growth

Once a clean SiC surface had been formed, samples were coated by a thin film of a iron using the *EGCO4 electron beam evaporator* at (see Sec. 3.6.2). The evaporator was typically degassed for a few hours at 15 nA flux prior to deposition. To achieve ~ 1 nm thickness of the iron film deposition was carried out at 10 nA flux in two rounds of 20 min. The attenuation of C1s and Si2p core levels was used to estimate the thickness of the iron film. XPS spectra were collected after iron deposition.

Once coated with a thin film of iron samples were annealed to form graphene. Resistive heating was used with a ramp rate of $0.5\,^{\circ}\mathrm{C\,s^{-1}}$ up to 710 °C, held for 10 min, and then cooled at a similar rate. For sample A this process was repeated twice in order to find out whether this had any effect. No clear change in the XPS spectrum was observed after the second anneal, and it was hence concluded that the reaction $\mathrm{SiC + Fe \rightarrow FeSi + C_{Gra}}$ had occurred to completion after the first annealing step.

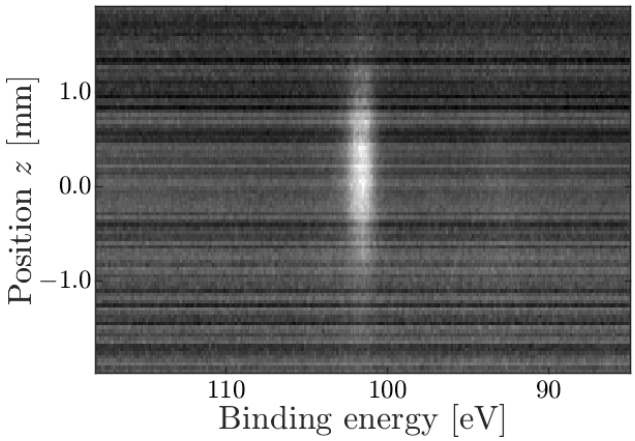

Figure 4.4: *XPS spectrum of Si2p with spatial resolution along the z-axis of the manipulator. The sample was mounted using two tantalum foils as masks forming a thin strip of exposed SiC as illustrated in Fig. 4.2. The blurry transition between the sample and masks suggests either improper sample alignment in y, or limited spatial resolution in the analyser, potentially due to the broken iris.*

4.1.3 XPS-procedure

XPS spectra were typically collected from clean SiC, after iron deposition and after graphitization by annealing. Samples were aligned prior to the first measurement in the x, y, z and θ directions on the manipulator by maximizing the Si2p core level while minimizing Ta4d from the sample holder and tantalum clips. In Fig. 4.4 the image formed in the detector's response to sample alignment is shown, with feedback of alignment in the z direction through spatial resolution, and through contrast and feature sharpness in the x and y directions. Once aligned the sample position was kept constant, and only the angle θ was moved between measurements in order to turn the sample away from the iron evaporator during degas. A magnesium anode *Specs XR50* X-ray source ($h\nu = 1253.6\,\text{eV}$) was used as the photoexcitation source, and electrons were detected using a *Specs Phoibos 150* hemispherical energy analyser. Typical scans over core levels were performed in 5 scans with energy step 0.1 eV and swell time 1 s using a pass energy of 20 eV over C1s, Si2p, O1s, Fe2p and Ta4d core levels.

XPS data of sample A was collected in spatially resolved mode as shown in Fig. 4.4. This allowed simultaneous acquisition from distinct regions. During the graphene formation described in the previous sections the sample was covered by Ta masks exposing only a small strip of SiC (Fig. 4.2b), and therefore spectra were

collected from regions of the SiC sample and Ta mask. Once finished graphene growth the sample was unloaded from the chamber, and the Ta mask was removed exposing regions of SiC exposed and unexposed to iron. The sample was loaded back into vacuum, and degassed as previously. XPS measurements were then repeated collecting data from exposed and unexposed regions of SiC simultaneously.

4.1.4 Valence band measurements and ARPES

Valence band spectra were collected from sample A at four stages of the experiment using the SPECS UVS 10/35 helium discharge lamp. The four stages included clean SiC, after iron deposition, after annealing to form graphene and after the Ta masks had been removed. Difficulties were faced in simultaneously aligning the UV light spot at the center of the sample and the sample under the detector were, mainly because the size of the light spot was comparable to the strip of exposed SiC. Hence some signal from the Ta mask was also expected.

ARPES measurements on sample B were attempted after degassing clean SiC, and after graphene formation, however no bands could be resolved.

4.1.5 Contact formation

Shadow masks for graphene patterning and contact formation in the fabrication a graphene Hall bar (sample B) were designed using the free computer-aided design software DraftSight. It was intended that the mask would be cut out of Ta foil by the NTNU Faculty of Sciences metal workshop using a water jet cutter - however due to long waiting time they were instead cut out by hand using a scalpel. The finished masks mounted on sample B at various steps of processing the Hall bar are shown in Fig. 4.5.

After successful graphene growth on sample B using the shadow mask in Fig. 4.5a it was removed from vacuum, and the mask for contact deposition (Fig. 4.5b) was spot welded on top of the first mask. The sample was then loaded back into the chamber, and degassed overnight at 300 °C in preparation for silver deposition. The rough steps for contact formation can be summarised as the following.

6. Attach shadow mask
7. Transfer back into vacuum
8. Overnight degas
9. Silver evaporation

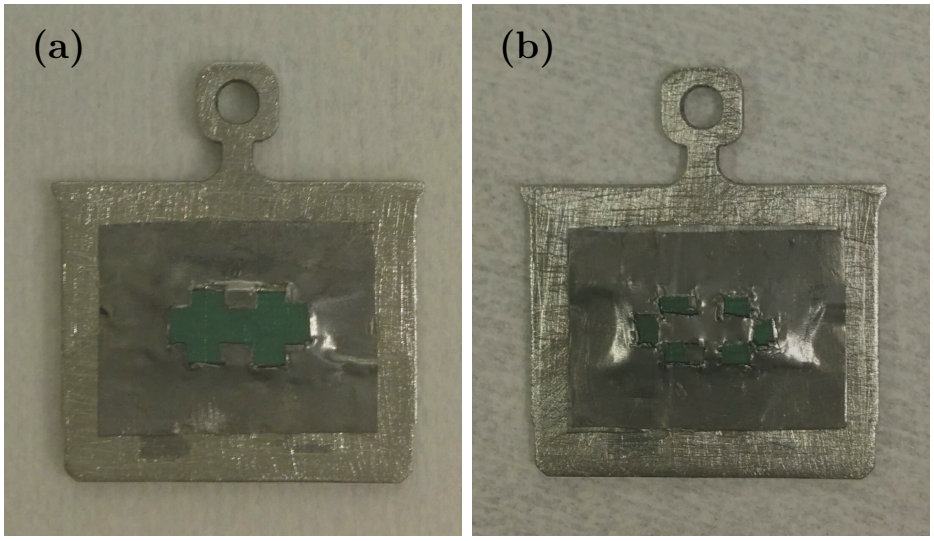

Figure 4.5: *Shadow masks for* ***(a)*** *graphene patterning and* ***(b)*** *contact formation mounted on sample B. Masks were cut out by hand using a scalpel, and were used for making a graphene Hall bar.*

10. Transfer out of vacuum chamber

Due to the lack of experience in UHV deposition of silver several attempts were made. Each evaporator was degassed overnight in the preparation chamber prior to deposition. The initial evaporator design included a tungsten filament wrapped around a piece of silver. Evaporation was carried out by passing a current through the filament to melt and evaporate the silver. The current was increased in small steps, and the sample was transferred to the main chamber between each step for XPS measurement to confirm the deposition of silver.

The first evaporation by this method failed as the piece of silver had fallen out of the evaporator during mounting. The second attempt using the same design was also unsuccessful, most likely due to the evaporation of all of the silver already during degassing. The final successful evaporation was carried out using silver wrapped inside a tantalum foil with small holes for the evaporation of silver toward the sample. Evaporation was carried out at 11 A for 9 hours. Figure 4.6 shows an optical microscope image of the sample after patterned graphene and contact formation.

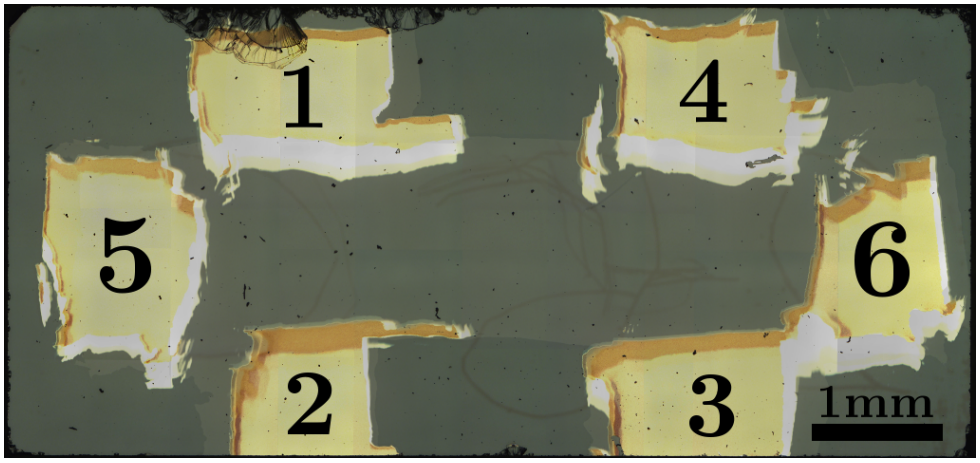

Figure 4.6: *Optical microscope image of the patterned graphene Hall bar with silver contacts. The image was constructed from smaller microscope images cropped together. A short between contacts 3 and 6 is visible, which was scraped off using a scalpel.*

4.2 XPS analysis

In this section the quantitative analysis on XPS data is described. The purpose of the analysis is to quantify the observed photoemission peaks in terms of intensity, position, spectral width, etc., and to use this information to determine the thickness and composition of layers formed at stages of SiC processing to grow graphene. In particular for characterisation of the reaction forming graphene by annealing iron treated SiC it is of interest to quantify amount of impurities present on SiC, the thickness of deposited iron film, the amount of graphene formed and the composition of the FeSi interlayer.

The analysis was done using Matlab, and all scripts beyond built-in Matlab functionality were written by the author. The analysis consisted of the three stages **(1)** correcting for transmission function and other experimental artefacts, **(2)** fitting curves which realistically deconvolute XPS features into peaks describing chemical states, spin-orbit splitting, etc, and **(3)** making a layer model of the sample surface that fits the peak parameters found.

In step **(1)** all XPS data was first divided by the transmission function provided by previous calibration of the instrument. For core levels with high separation between components such as the spin orbit splitted Fe2p core levels Mg Kα satellite components were removed by subtracting the data shifted and scaled to the spectral position and intensity of known satellite components from itself. Due to the small

exposed area of SiC on sample A the signal from the Ta mask was also subtracted by fitting Ta4d core levels on regions corresponding to SiC and Ta, and subtracting data measured on the mask from the SiC data scaled for Ta intensity. In the following two sections steps **(2)** and **(3)** are described.

4.2.1 Peak profile fitting

Peak profile fitting to XPS core level data was carried out using Levenberg-Marquardt least squares method in Matlab. Functions fitted were of the form

$$y = mx + c + \sum_{i=1}^{n} \Big[I_i \, \mathrm{P}\left(x; x_i, \dots\right) + a_i I_i \, \mathrm{S}\left(x; x_i, W_i\right) \Big] \tag{4.1}$$

where m and c are the coefficients of a linear background, n is the number of peak components fitted with intensities I_i, P is either the pseudo-Voigt function with peak parameters σ_i and γ_i or the normalized Doniach-Sunjic profile with parameters α_i and F_i and S is the Shirley background profile with height $a_i I_i$ and width W_i given as a function of the peak parameters (see Sec. 2.4.1).

The total degrees of freedom in the fit is therefore $5n + 2$ including the two linear coefficients, and for each peak a height, center, relative height of the Shirley background and two parameters defining the peak shape. In order to obtain realistic fits several of the parameters Eq. 4.1 had to be constrained. Typical constraints imposed can be summarized as the following.

- Generally for all direct photoemission peaks the Gaussian width σ of the pseudo-Voigt function was locked to a single variable. The justification for this is that the main contribution to σ is the linewidth of the X-ray source, which is a constant for all peaks.
- The linear background coefficient m was in most cases locked to zero as it is considered unphysical. In some cases however when fitting a small peak it is necessary to include to obtain a good fit, for instance in order to approximate the background from a wide neighbouring peak.
- The relative Shirley step height was in most cases also locked into a single variable as the increase in the in the secondary electron spectrum is typically proportional to the intensity of the peak.
- The ratio of the intensities of spin-orbit coupled peaks were locked to their theoretical value. In case of the Si2p peak also their separation was locked as the two peaks are difficult to resolve in most data.

Table 4.1: *Material parameters used in layer modelling. Parameters a and c are the lattice constants, n is the number of stoichiometric units per unit cell and δ is the calculated density. Lattice parameters obtained from Ref. [54–57].*

Material	Lattice structure	Plane	a [Å]	c [Å]	n	δ [g cm^{-3}]
SiC	Hexagonal	{0001}	3.08	15.12	6	3.22
Fe	Body-centered cubic	{111}	2.86	-	2	7.93
FeSi	Simple cubic	{111}	4.46	-	4	6.28
C_{Gra}	Hexagonal	{0001}	2.46	6.71	4	2.27

- Sometimes additional restrictions had to be imposed in order to obtain a fit, but these were in most cases only imposed to guide the convergence of the fit, and it was made sure that the final fit converged to a local minimum between the constraints.

4.2.2 Layer modelling

A model of the layer structure was created at each stage of the sample processing in order to evaluate the thickness of layers and degree of oxygen contamination. Parameters of the main materials used in modelling are summarized in Tab. 4.1. The intensity I_p of peak p corresponding to an XPS core level or particular chemical state was approximated as

$$I_p = \sigma_p \lambda_p \sum_l n_{l,p} \left(e^{\frac{d_l}{\lambda_p}} - e^{\frac{d_{l+1}}{\lambda_p}} \right) \tag{4.2}$$

where σ_p is the photoemission cross section of the core level at $h\nu = 1253.6\,\mathrm{eV}$, λ_p is the inelastic mean free path of electrons with kinetic energy $\mathrm{KE} = h\nu - \mathrm{BE_p}$ found using the "universal curve" (Eq. 2.32), $n_{l,p}$ is the atomic density of the element from layer l contributing to peak p calculated from Tab. 4.1, and d_l is the starting depth of layer l (i.e. $d_1 = 0$). Mixtures of materials with oxygen was assumed to have the same weight density as pure materials, and for SiO_2 an experimental density of $2.65\,\mathrm{g\,cm^{-3}}$ was assumed.

A model of the layer structure was made with several free variables such as the thickness of layers and ratio of elements in some layers. The sum of the intensities of all peaks was normalised for both experimental and simulated data, and a best fit of the parameters to data was carried out using the Levenberg-Marquardt least squares method. Uncertainties were estimated using the function `nlparci` in the

Matlab Statistics and Machine Learning Toolbox giving 95% confidence intervals of the parameters.

4.3 Characterization at NanoLab

Once finished with sample growth and characterization in UHV samples were taken to the NTNU NanoLab for further characterization. Samples were first viewed under an optical microscope. The difference between regions exposed and unexposed to iron on patterned samples is clearly visible by the naked eye and in an optical microscope. An optical microscope image of sample B after contact formation is shown in Fig. 4.6 revealing a short between contacts 3 and 6. The samples were also inspected using the *Hitachi TM3000 Tabletop microscope* in both scanning electron microscopy and energy-dispersive X-ray spectroscopy modes, but neither could resolve the difference between exposed and unexposed regions.

The *Renishaw inVia* Raman microscope was used to inspect each finished sample to check for the presence of graphene. Patterned samples were inspected at both exposed and unexposed regions. Raman spectra were collected using a 532 nm excitation source at 5 mW intensity over the a spectral range from 0 to 3200 cm^{-1}. No characteristic features of graphene could be observed.

Atomic force microscope images over the border between exposed and unexposed regions on sample A were taken using the *diMultimode V* AFM from *Veeco Metrology*. An example of an image obtained is shown in the Results (Fig. 5.8). The step height due to the deposited layer could not be determined as the transition between the two regions is relatively smooth, and measurements on pure SiC do not yield a sufficiently flat surface.

The *Nanosurf easyScan 2* scanning electron microscope (STM) was used to inspect sample A, and in particular to do local density of states measurements using the instrument in scanning tunnelling spectroscopy (STS) mode. No good data of the sample could however be obtained, and it is expected that this was due to insufficient conductivity of the substrate for STM measurements. An image of a highly ordered pyrolytic graphite (HOPG) reference sample was obtained using the same tool which is shown in Fig. 4.7. The image shows the same hexagonal pattern of carbons arranged in a honeycomb lattice as expected for graphene. Note that the apparent spheres arranged in a hexagonal pattern of what could be confused with a single atom in the image is in fact the two top atoms in the unit cell of graphite.

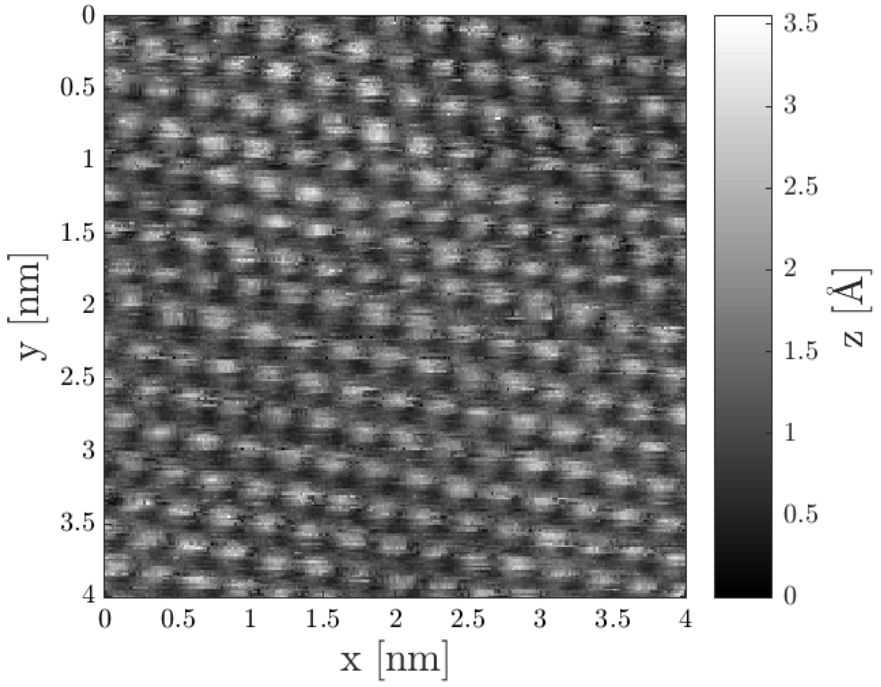

Figure 4.7: *STM image of highly oriented pyrolytic graphite. The figure shows a similar hexagonal pattern as expected for graphene.*

4.4 Electrical measurements

Electrical measurements were performed on the Hall bar in order to characterise the charge carriers in the sample, and to assess the performance of the device as a radiation detector. In order to carry out the Hall measurements the sample was mounted on a PVC (polyvinyl chloride) circuit board using carbon tape as shown in Fig. 4.8a. Copper tape was used to make a back-contact for photoconductance measurements. The sample as created in the UHV process had a short between contacts 3 and 6 (Fig. 4.6) which was carefully scraped off using a scalpel.

Wedge wire bonding was attempted to make connections from the device contacts to the PVC board using the *TPT HB05 Wedge and Ball Bonder*, however no suitable parameters were found to achieve formation of a good bond of the gold wire onto the sample without damaging the silver contacts. Hence a different approach was chosen using silver glue to attach copper wires to the contacts. This is shown in Fig. 4.8c. The device connections were debugged using a multimeter, and relatively

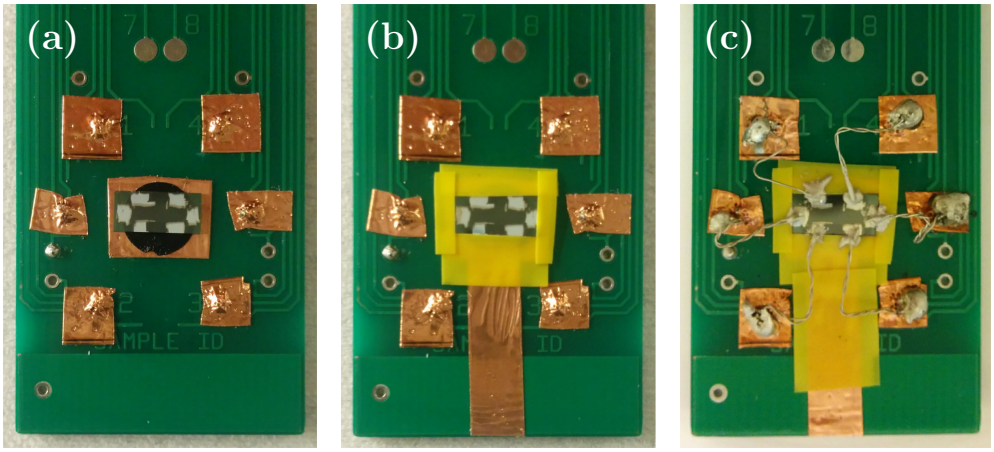

Figure 4.8: *Formation of electrical connections to device contacts using silver glue.*

high resistances in the order of a few kΩ were measured.

4.4.1 Hall mobility

Hall mobility measurements were carried out at the NTNU Hall lab in the Electrical Engineering Building using the *Lake Shore Model 7504* Hall system. An excitation current of 200 µA was applied between terminals 5-6 of the device, and an orthogonal magnetic field was varied in steps of 1 G with a maximum magnitude 5 G. The Hall voltage across terminals 1-2 and 3-4 were measured.

A low sample resistance was measured by four probe measurement. This along with the high contact resistance of silver glue resulted in poor measurements with non-linear IV-curves. Multiple attempts were made with limited success to obtain reliable measurements

4.4.2 Photoconductance

Photoconductance measurements were carried out at the Department of Physics Solar Simulator lab. The *Sun 2000 Solar Simulator* from *Abet Technologies* was used as a light source with an output equivalent to the intensity of the sun. Electrical connections to the device were made by placing probes directly on the silver contacts, hence eliminating problems related to the high resistance of silver glue. The resistance of the device was measured by passing a current I between terminals 5-6, and measuring the voltage V over contacts 2-3 or 1-4 along the current. A gate voltage V_g

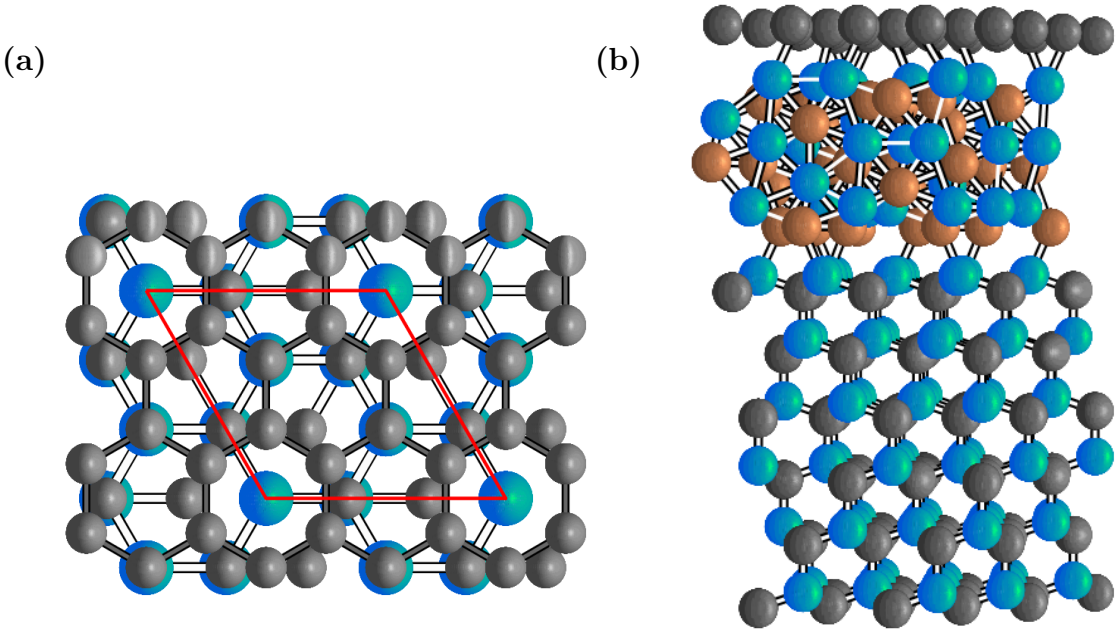

Figure 4.9: ***(a)*** *Supercell for DFT calculation of epitaxial graphene on SiC* (0001)*. The unit cell indicated in red consists of four unit cells of graphene and three unit cells of 6H-SiC laterally arranged in a* $(\sqrt{3} \times \sqrt{3})R30°$ *structure.* ***(b)*** *Unit cell of* $6\mathrm{H} - \mathrm{SiC} + \mathrm{FeSi} + \mathrm{C_{Gra}}$ *system for slab surface calculation consisting of four of the unit cells shown in (a) in a* 2×2 *arrangement with a* (111) *oriented FeSi interlayer.*

was applied between terminal 5 and the back contact. The electrical connections for radiation sensing using a similar device was illustrated in Fig. 2.8.

IV-curves were collected varying the current I in between -200 and $200\,\mu\mathrm{A}$ in steps of $10\,\mathrm{A}$ and measuring the voltage V with the light source on and off. Measurements were repeated varying the gate voltage V_G from -5 to $5\,\mathrm{V}$ in steps of $1\,\mathrm{V}$ for contact pairs 2-3 and 1-4.

4.5 Numerical methods

Simple *ab-initio* calculations were performed in order to illustrate physical phenomena in Chapter 2, and to gain greater understanding of the results in Chapter 5. All calculations were performed using the density functional theory (DFT) code SIESTA [17], a computer program implementation of a method to perform electronic structure calculations and molecular dynamics simulations of molecules and solids written in Fortran 95. SIESTA uses standard Kohn-Sham self-consistent den-

sity functional method described in Sec. 2.2 with localized atomic orbitals as the basis set. Core electrons are described by norm-conserving pseudopotentials.

All calculations in this thesis were performed with the generalized gradient approximation using the Perdew-Burke-Ernzerhof exchange-correlation functional. All pseudo-potentials generated using the ATOM program with input files downloaded from the ABINIT pseudo database [58]. Density of states curves were generated using the COOP utility with smearing parameter of 0.2 eV. All lattices were relaxed using Conjugate Gradient minimization, however in surface calculations already relaxed SiC unit cells were used and only the top atomic layer was relaxed again. No relaxing was performed in the generation of Fig. 2.1 as disequilibrium lattice parameters were used.

Simulations on single unit cell systems were performed using high k-point sampling of at least 30 points in each bulk dimension using the Monkhorst-Pack method, and double-zeta polarization basis sets. Surface simulations were performed using single-zeta basis sets and lower k-sampling for atomic relaxations, and only the final electronic structure calculations was performed using high k-sampling.

Epitaxial single and bilayers of graphene on pure SiC and with a FeSi interlayer were simulated. For lesser computational effort a $(\sqrt{3} \times \sqrt{3})R30°$ graphene reconstruction was assumed. The resulting graphene and FeSi lattice parameters had 2.4% and -1.7% deviation from their relaxed structure. The unit cells used in each case with a monolayer graphene are shown in Fig. 4.9. Simulations of epitaxial graphene on SiC included 44 and 52 atoms for mono- and bilayer of graphene, and atomic relaxations were carried out using $10 \times 10 \times 4$ k-grid sampling. Final electronic states structure was computed at $25 \times 25 \times 1$. The SiC-FeSi-C_{Gra} system included 242 atoms with a monolayer of graphene, and 202 atoms with a bilayer due to the exclusion the bottom layers of SiC in the latter. Relaxation was carried out using Γ-point sampling only, and final electronic structure was calculated using a $10 \times 10 \times 1$ k-grid.

Chapter 5

Results

The following chapter is dedicated for presenting the most central results from work described in the Methods. In the first section results relevant to graphene growth in UHV and characterisation of the graphitization reaction are shown. In the following section successful graphene patterning is demonstrated. The outcome of electrical measurements are overviewed in Sec. 5.3, and in Sec. 5.4 results from the computational work are presented.

5.1 Graphene formation

XPS is the main technique in this project used for characterizing the growth of graphene, and controlling critical parameters of the growth process such as the thickness of deposited layers, and the annealing time and temperature. Along with LEED it constitutes the only evident proof that the method for growing graphene has been successful, and provides means of estimating the compositional structure of layers formed at the sample surface.

As discussed in the Methods, multiple attempts to obtain a clean SiC sample and to grow graphene has been made. The experiment was completed for three of the samples, however for one of the samples only a thin layer of iron was deposited, resulting in a small fraction ($\sim 15\,\%$) of a monolayer graphene grown, i.e. partial coverage of the surface. Samples A and B had the same UHV processing steps and show similar XPS data, however the area exposed for graphene growth was larger in the latter, and hence all data shown in this section is from the latest sample.

5.1.1 Clean SiC

After degassing samples LEED and XPS measurements on clean SiC were done in order to assess the amount of contaminants on the surface. Note that while common procedure for removing the native layer of SiO_2 from the SiC surface involves annealing samples in the excess of 1000 °C [53], samples could only be heated up to approximately 710 °C due to a limitation in the maximum power tolerance of the filament. The actual temperature of the sample is likely to have been slightly higher as it is closer to the filament than the thermocouple. Argon sputtering of the sample to remove oxide layer was also attempted, however without success as increasing the power gradually resulted in a loss of crystallinity of SiC, and no LEED pattern could be observed after sputtering.

Data from measurements on clean SiC for sample B is shown in Fig. 5.1. Core-levels of the three main elements Si, C and O present in the sample are shown along with the LEED pattern of SiC. The widescan from the same data set was shown in in Chapter 2, Fig. 2.14. The data shows that the sample pre-treatment was not sufficient to fully remove the native oxide layer on SiC. The width of the Si2p core level, and the inability to resolve its spin-orbit splitted components, indicate the presence of silicon in multiple chemical environments due to oxidation. This is supported by the binding energy of the O1s peak at 532.3 eV, which coincides with the expected range for SiO_2 [59]. Quantitative analysis on the three core levels shows good agreement of the peak intensities with a partial coverage of SiC by SiO_2. The thickness was calculated to be (0.9 ± 0.2) Å assuming uniform coverage. Similar analysis on sample A reveals a SiO_2 thickness of (0.7 ± 0.2) Å.

The C1s core level shows a main component at binding energy 283.6 eV from SiC, and a small component at 284.6 eV matching the chemical shift for sp^2 C-C compounds. The carbonous peak is most likely due to some residual organic contamination, and is assumed to have limited effect on the device performance at the scope of this project. The converse is assumed to be true for SiO_2 which has been shown to highly impact the performance of SiC devices [60], and may also affect the subsequent growth of graphene.

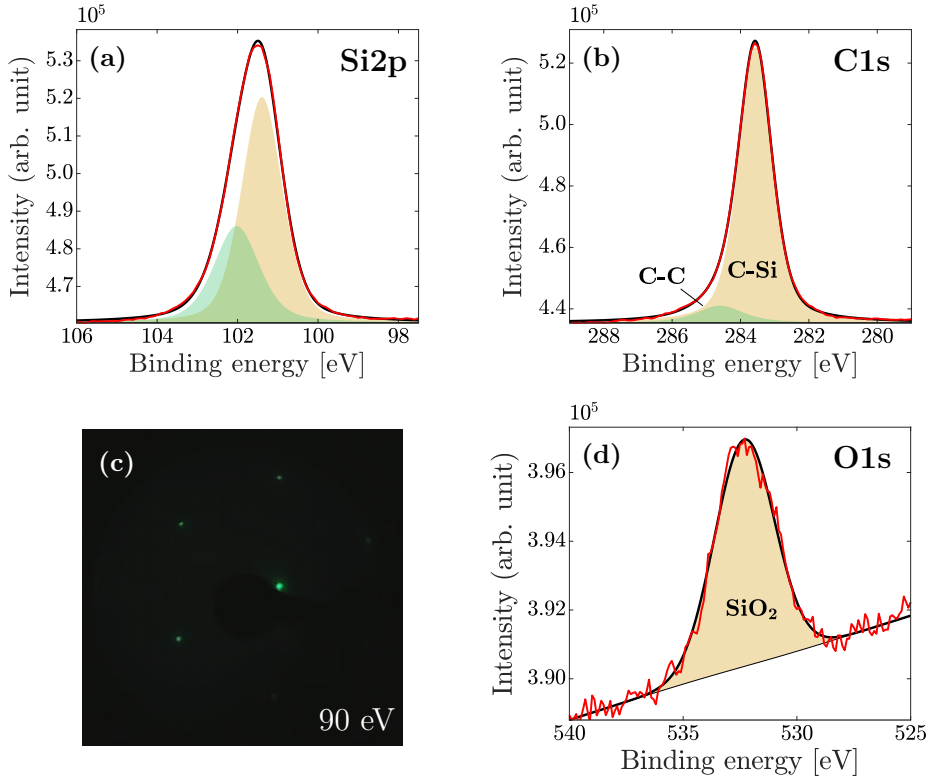

Figure 5.1: *Clean SiC* $(000\bar{1})$. ***(a)*** *Silicon core-level showing deconvoluted* $Si2p_{3/2}$ *and* $Si2p_{1/2}$ *spin-orbit components. The asymmetric shoulder due to spin orbit splitting is not visible, which indicates the presence of multiple chemical states due to oxidization.* ***(b)*** *C1s showing a main chemical component from SiC and a small amount of* sp^2 *carbon that may originate from organic or graphitic contamination.* ***(c)*** *Hexagonal LEED pattern of SiC at* 90 eV *incident electron energy.* ***(d)*** *Small O1s peak attributed to* SiO_2 *at the sample surface.*

5.1.2 Iron deposition

The Fe2p and O1s core level spectra after 40 min deposition of iron are shown in Fig. 5.2. The overall thickness of the iron film was determined to be (10 ± 2) Å. The appearance of an additional oxygen component indicates that degassing the iron evaporator was not sufficient, and that some oxygen was deposited along with iron. Analysis on all four core levels including two chemical states for oxygen suggests that iron and oxygen were deposited in a stoichiometric ratio 25:1. Improper degassing was a result of the flux monitor failing prior to degassing the evaporator for deposition on the last sample, which added uncertainty in the flux used during degassing. For

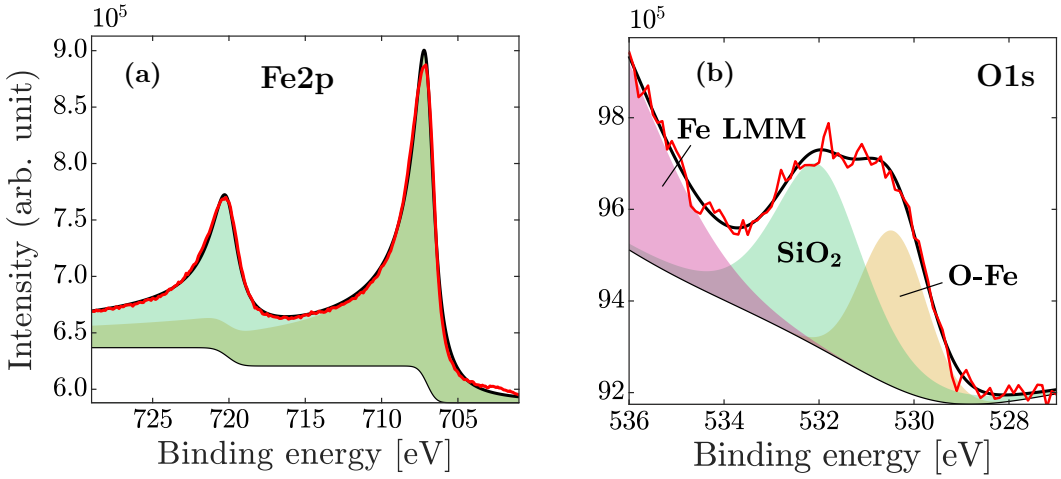

Figure 5.2: ***(a)*** *Fe2p of a freshly deposited thin film.* ***(b)*** *O1s after iron deposition showing components of oxygen reacted with iron and silicon.*

sample A no O1s peak was resolved after subtracting the oxygen signal originating from tantalum, and the thickness of the iron film found was (6 ± 1) Å.

5.1.3 Graphene growth

Graphene was formed by annealing iron-coated SiC samples at 710 °C for 10 min. XPS and LEED data confirming the formation of graphene is shown in Fig. 5.3. A widescan is shown in (a) showing large Fe2p and Fe Auger peaks along with slightly attenuated C1s, silicon peaks and small amounts of oxygen and tantalum from the mask.

The Si2p core level in (b) and (c) show the appearance of an additional chemical state owing to the reaction between SiC and Fe forming FeSi. Quantitative analysis shows that the stoichiometric ratio Fe:Si in the interlayer is approximately 1:0.92, which is in compliance the formation of FeSi as the main phase. The thickness of the interlayer was found (7 ± 2) Å, with an estimated 5% oxygen contamination. For sample A, a slightly lower silicon content with the stoichiometric ratio 1:0.79 and thickness of the FeSi layer (6 ± 1) Å were found.

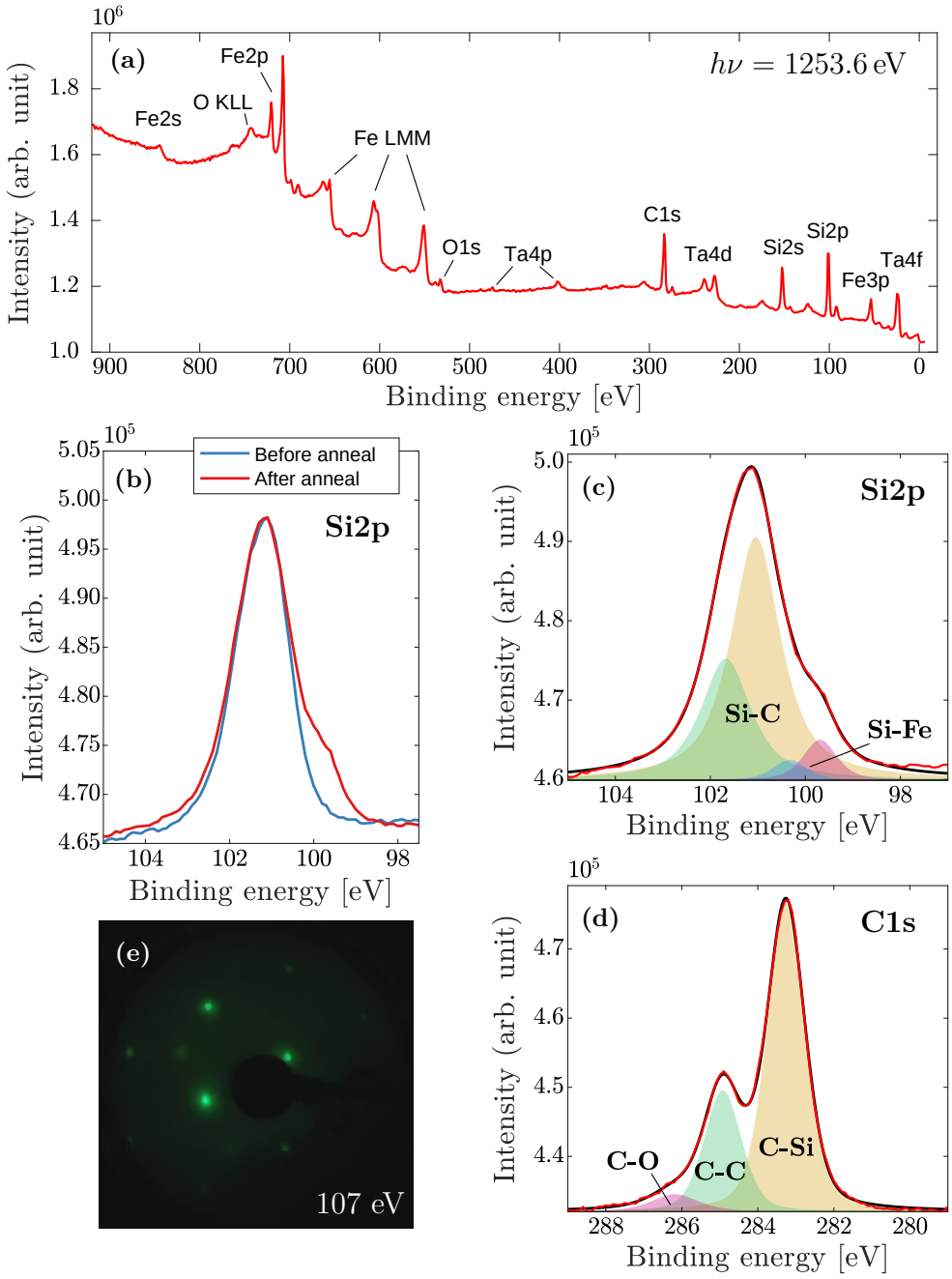

Figure 5.3: *XPS and LEED data showing graphene on SiC.* ***(a)*** *Widescan after annealing iron treated SiC at* 710 °C. ***(b)*** *Formation of a FeSi shoulder during annealing in the Si2p core level.* ***(c,d)*** *Deconvoluted Si2p and C1s peaks on SiC showing FeSi and graphitic components respectively.* ***(e)*** *LEED pattern of graphene on SiC with a dim hexagonal structure rotated by* 30° *compared SiC.*

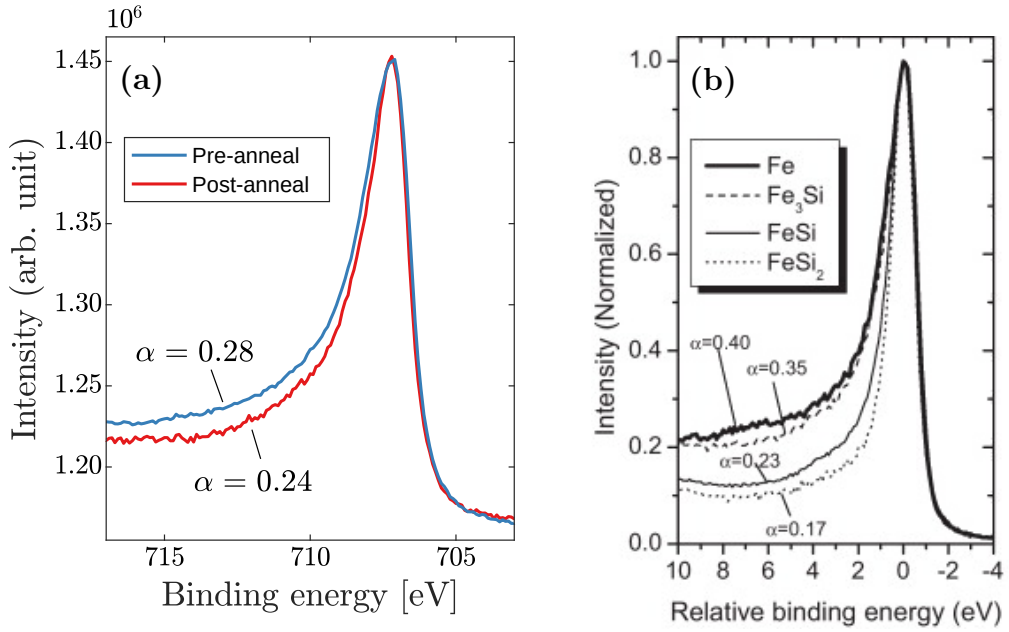

Figure 5.4: ***(a)*** *Fe2p core levels and asymmetry parameter before and after annealing iron-treated SiC* $(000\bar{1})$. ***(b)*** *Dependence of the asymmetry parameter of Fe2p on iron silicide phase. Adapted from [61].*

The C1s core level in Fig. 5.3d shows distinct carbon peaks originating from SiC and graphitic carbon. The position of the graphene peak at 284.9 eV corresponds to graphene [59]. The ratio of the peak areas is 0.38, and the thickness of the graphene layer in the layer model was found to be (1.7 ± 0.5) Å corresponding to half a monolayer of graphene. For sample A the graphene thickness was found to be (3.0 ± 0.7) Å corresponding to 89% of a monolayer.

In Fig. 5.3e the LEED pattern of sample A is shown after graphene formation. The pattern shows the same hexagonal structure from SiC as observed in Fig. 5.1c, with somewhat blurred spots due to the less ordered layers of FeSi and graphene at the surface. A dimmer hexagonal pattern rotated 30° from the SiC carbide pattern is also visible which is attributed to the graphene layer rotated 30° with respect to SiC. Note that only two diffraction spots are visible in the figure due to inhomogeneity in the phosphor screen, and the sample not being mounted perfectly along to the diffraction plane. The relative size of the patterns from SiC and graphene are in good agreement with the ratio of their lattice parameters.

The Fe2p core levels before and after annealing the sample at 710 °C to form graphene are shown in Fig. 5.4 along with a figure showing the asymmetry of Fe2p

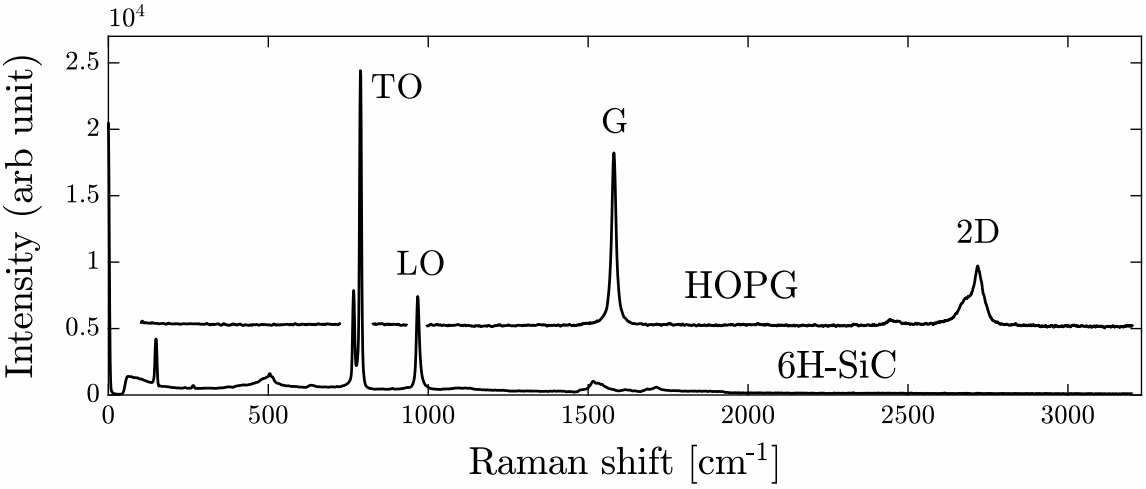

Figure 5.5: *Raman spectra of graphene patterned SiC and a HOPG reference sample. The spectrum for the sample shows a characteristic spectrum for SiC and no sign of graphene, most likely due to the low thickness of the graphene film.*

core levels for various phases of iron silicide. The post-anneal asymmetry parameter α is in good agreement with the formation on FeSi, however pre-anneal α is fairly lower than expected for clean iron. This could be partially explained by the measured oxidation of iron leading to less metallic behaviour of the thin film.

A Raman spectrum taken on the graphene strip of sample A is shown in Fig. 5.5 along with the spectrum of a HOPG reference sample. No difference in the spectrum between exposed and unexposed areas can be observed, and the spectrum looks like the typical spectrum for clean SiC. None of the expected features for graphene exhibited in the graphite reference sample can be observed on SiC. It is likely that a thicker film of graphene is required to observe it in the Raman spectrum. For epitaxial graphene on SiC it has been shown that the graphene buffer layer on pure SiC only exhibits minimal graphitic features [62].

5.1.4 Valence band mapping

Valence band spectra at various stages of processing sample A were taken using a He I ultraviolet light source ($h\nu = 21.22\,\mathrm{eV}$). The results are shown in Fig. 5.6a. All spectra extend up to the Fermi-level showing the Fermi edge profile of the Fermi-Dirac function (see Eq. 2.6) characteristic for metals. This is an unexpected result for clean SiC, a semiconductor (n-doped, see Sec. 5.3), and is most likely explained by some of electrons detected coming from the tantalum mask. It seems reasonable

to expect that the true valence band edge from SiC occurs around 2 eV of binding energy where a drop in the intensity is observed in the figure. After iron deposition the photoemission intensity at zero binding energy increases drastically which is expected for a metal due to their high density of states at the Fermi-level.

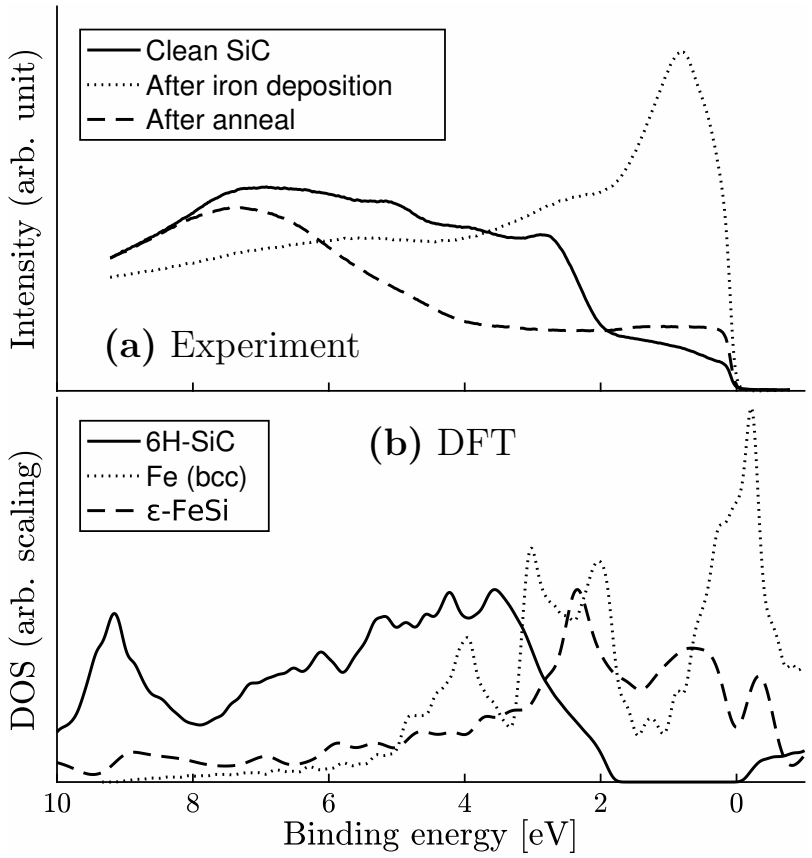

Figure 5.6: ***(a)*** *Valence band measurement results using photons from a He I ultraviolet source on sample A, showing spectra for clean SiC, iron coated SiC and spectrum after graphene formation.* ***(b)*** *Density functional theory calculations of the density of states in 6H-SiC, bcc Fe and cubic ϵ-FeSi. Calculated using SIESTA, see Sec. 4.5. A smearing of width* 0.2 eV *is applied which causes the narrow band-gap of FeSi to become unresolved.*

After annealing the density of states at the Fermi-level falls but remains higher than for clean SiC. It is not straight-forward to interpret the difference between clean SiC and after anneal valence band spectra in the figure due to fine sensitivity of results on sample alignment and uncertainty about where detected electrons originate from. One can nevertheless speculate that the majority of the signal comes from

graphene and the FeSi-interlayer.

In Fig. 5.6b the DFT density of states is shown for 6H-SiC, body-centered cubic iron and cubic iron silicide calculated using SIESTA. Keeping in mind that the valence band spectrum is roughly given by the density of states modulated by the Fermi-Dirac function plus a secondary electron background, which is comparable to the cumulative sum of the DOS, one can see resemblances between the UPS measurements and calculated DOS – at least for the case of clean SiC and iron. A weakness of this comparison is that while the valence band spectrum is only collected over a limited region in k-space, the density of states is calculated by integrating over the entire k-space.

5.2 Graphene patterning

Sample A was patterned with a narrow strip of graphene (see Fig. 4.1a) in order to show that selective formation of graphene is possible by depositing iron through a shadow mask prior to annealing. The patterned sample was investigated using spatially resolved XPS, and the results are shown in Fig. 5.7. In (a) the Fe2p core level spatially resolved in one dimension is presented showing the iron-treated strip light up on the sample. The C1s and Si2p spectra integrated over the exposed and unexposed regions indicated in the image are shown in (b-e).

The spectra show convincing evidence of that patterning graphene using this method works with a resolution within an upper limit of a few hundred micrometers. The C1s core levels show clear distinction between the exposed and unexposed regions, with a significant graphitic peak only present on the strip exposed to iron. A small C-C component can be observed in (c) which is comparable to the peak observed on clean SiC. Similarly (d-e) shows the formation of a FeSi component on the exposed region only.

An AFM image of sample A is shown in Fig. 5.8 over the edge of the graphene strip. The top region shown in the image is the clean unexposed SiC region, and the lower half corresponds to the region where graphene formation has been confirmed by spatially resolved XPS. It appears from the image that SiC has high surface roughness compared to the region with iron, which is an unexpected result for a polished single crystal SiC sample. The image also shows some larger defects on the iron covered region.

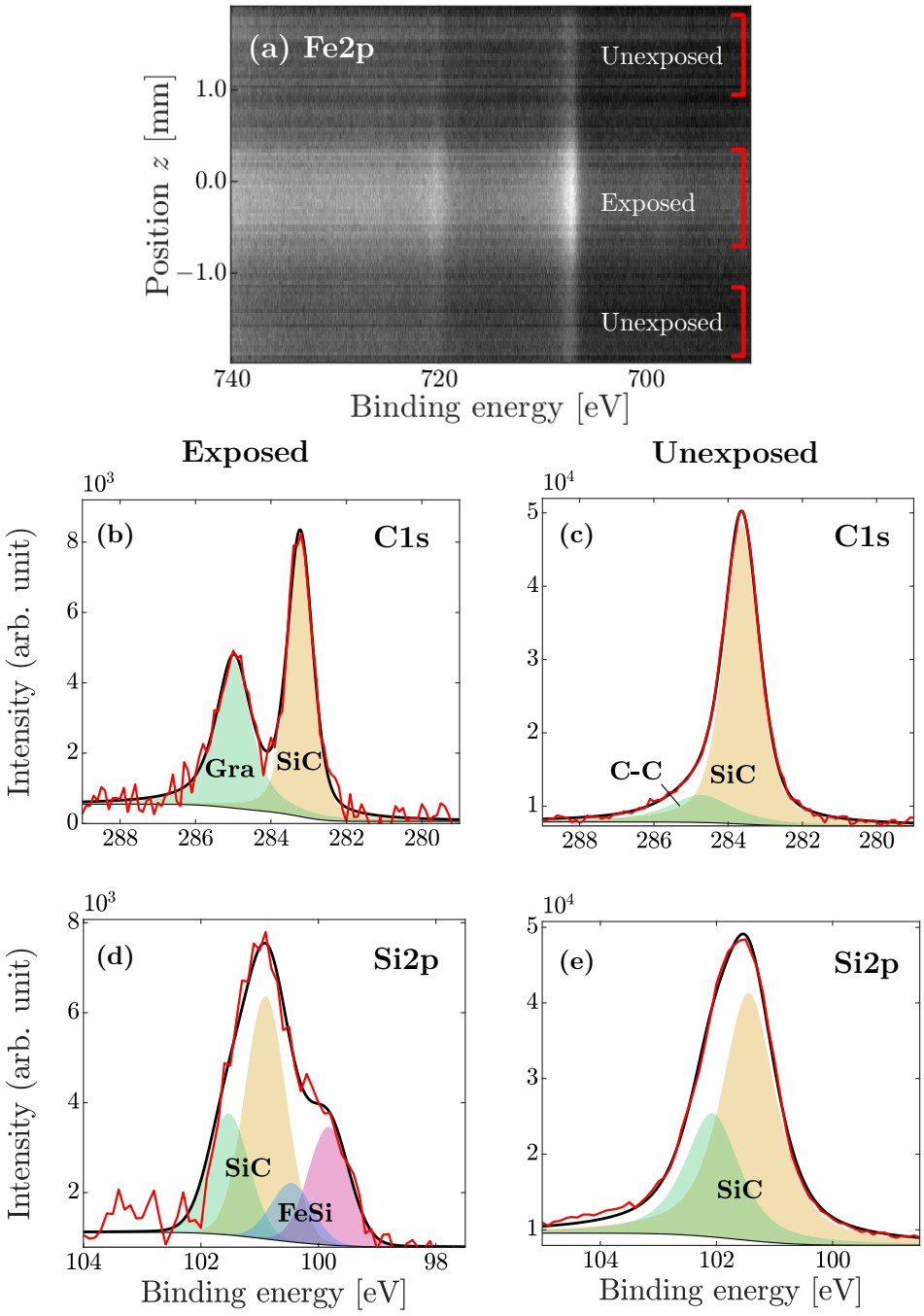

Figure 5.7: ***(a)*** *Fe2p core level resolved spatially in the z-direction of sample A after removing Ta mask, showing regions exposed and unexposed to iron.* ***(b-e)*** *C1s and Si2p core levels on regions exposed and unexposed to iron showing a successful patterning of the sample with graphene.*

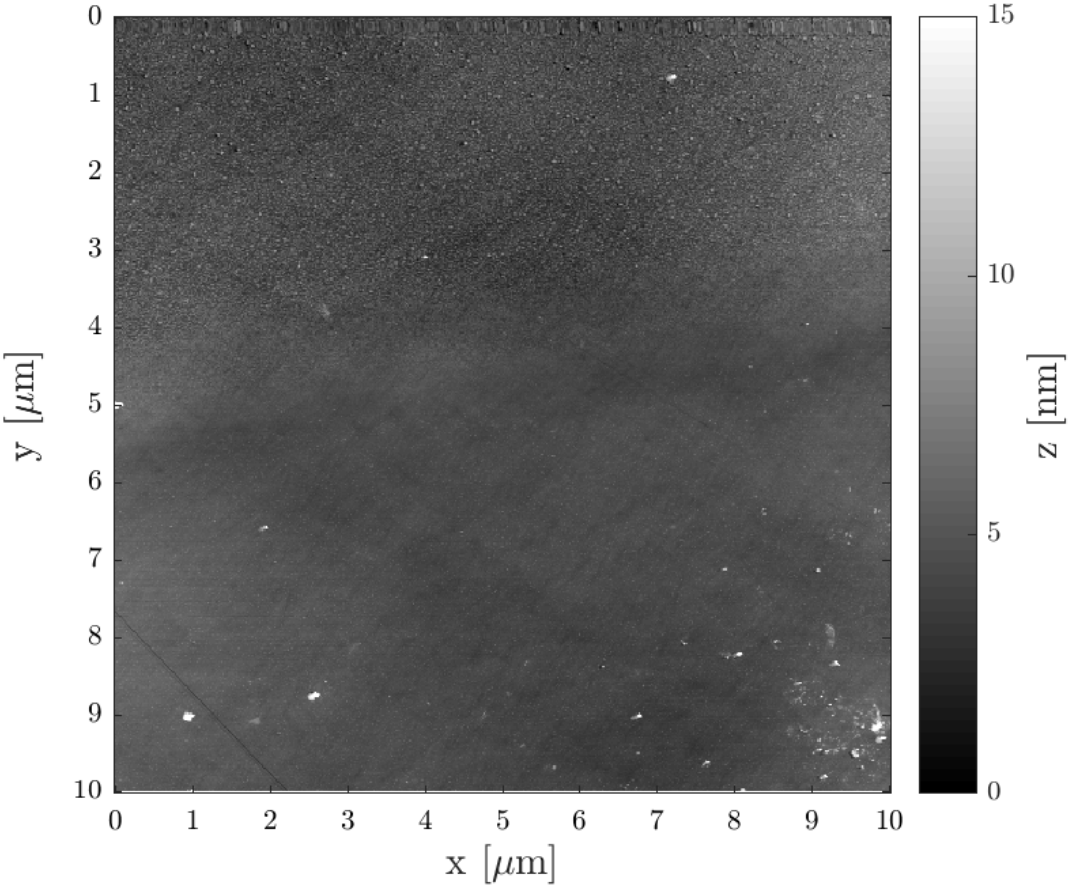

Figure 5.8: *Atomic force microscope image of sample A over the border between exposed (bottom) and unexposed (top) regions.*

5.3 Electrical behaviour

Sample B was made for characterising the electrical properties of the SiC-FeSi-C_{Gra} system. As the aim of studying this system is to exploit the electrical behaviour of the graphene film in the formation of a radiation sensor, measuring its electrical properties is a key step for achieving that goal. Two types of electrical measurements were carried out, Hall measurements for estimating the concentration and mobility of majority charge carriers in the sample, and photoconductance measurements in order to test whether any response in the conductance of graphene to radiation could be measured.

The averaged sample resistance measured between contact pairs along the length of the device (contacts 1-4 and 2-3) was found 1.08 Ω using four point probe measurement. As this value is far too low for a single sheet of graphene with approximately square dimensions, it is presumed that this value is dominated by the conductivity of the substrate.

5.3.1 Hall measurement results

Due to high resistivity of the silver glue used for wiring, poor quality Hall measurements were obtained with unreliable results. Only contact pair 1-2 produced a linear relationship of the Hall voltage as a function of applied magnetic field, and the slope of the measured curve was given by $(-19 \pm 1)\,\mathrm{mV\,G^{-1}}$ indicating electrons as majority charge carriers. The slope translates into a substrate sheet carrier density of $6.6 \times 10^{13}\,\mathrm{cm^{-2}}$ for an excitation current of 200 µA between terminals 5-6.

Assuming that the Hall measurements are dominated by conduction in the substrate, and using an effective substrate thickness of 500 µm the sheet carrier density translates into $1.3 \times 10^{15}\,\mathrm{cm^{-3}}$. Furthermore, using the 1.08 Ω zero-field resistance of the sample with channel width 1.5 mm and length 2 mm the electron mobility can be estimated as $1.2 \times 10^{5}\,\mathrm{cm^2\,V^{-1}\,s^{-1}}$. This value is clearly too high for SiC, or even for graphene grown epitaxially on a substrate.

5.3.2 Photoconductance results

Unlike Hall measurements, photoconductance measurements were made directly on the silver contacts on of the device, and therefore yielded far more accurate results. The IV curves measured were highly linear, and their slope in units of resistance for the two sets of contacts is shown in Fig. 5.9 as a function of gate voltage with and without light.

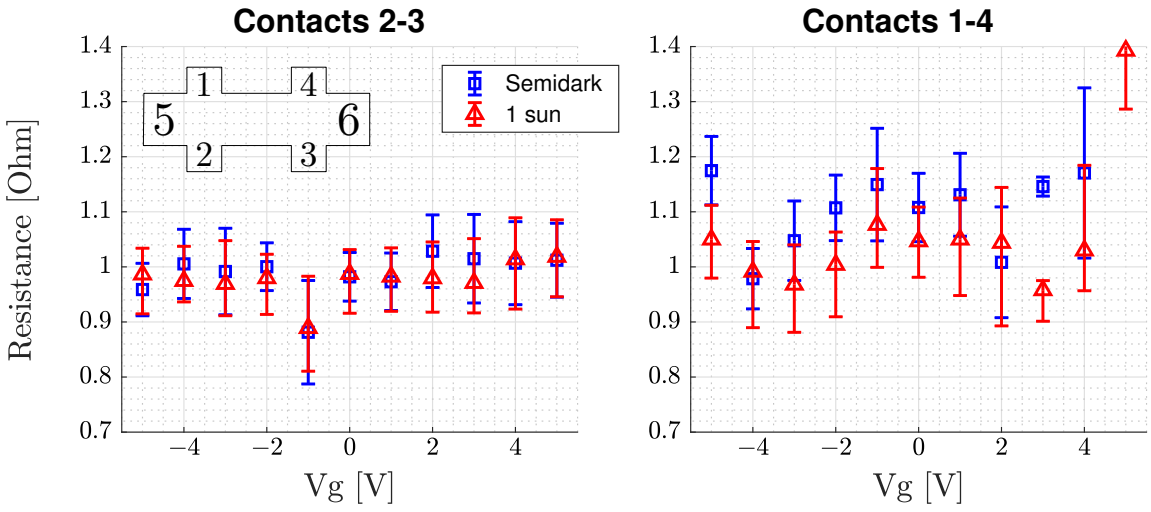

Figure 5.9: *Resistance of the sample between contacts 2-3 and 1-4 with and without light as a function of gate voltage. Error bars are the one standard deviation uncertainties based on goodness of the linear fit.*

No significant trend as a function of gate voltage is apparent. Contact pair 2-3 yields more consistent results due to larger exposed area on the silver contacts, and hence easier placement of probes. Exposure to light yields slightly improved conductivity of the sample, with a decrease in the resistance averaged over all gate voltages of 1% and 17% for contacts 2-3 and 1-4.

5.4 Computational results

The results of the numerical study on epitaxial and iron-catalyzed growth of graphene on SiC is shown in Fig. 5.10. The density of state from the first and second layers of graphene on both structures is plotted along with the DOS for free standing graphene (FSG). In both cases the formation of a buffer layer with characteristics distinct from FSG is evident. The second graphene layer shows intermediate features between the structure of the buffer layer and FSG, although with closer resemblance to the latter.

The DOS of graphene on SiC was found to exhibit the characteristics of the the buffer layer with the formation of a band gap below the Fermi-level as has been shown in previous works [63]. The atoms relax into a non-planar structure due to partial covalent bonding with the underlying substrate, and the Fermi-level shifts due to the higher electronegativity of carbon compared to silicon. The second graphene layer is held on top by van der Waals forces at a separation of 3.41 Å.

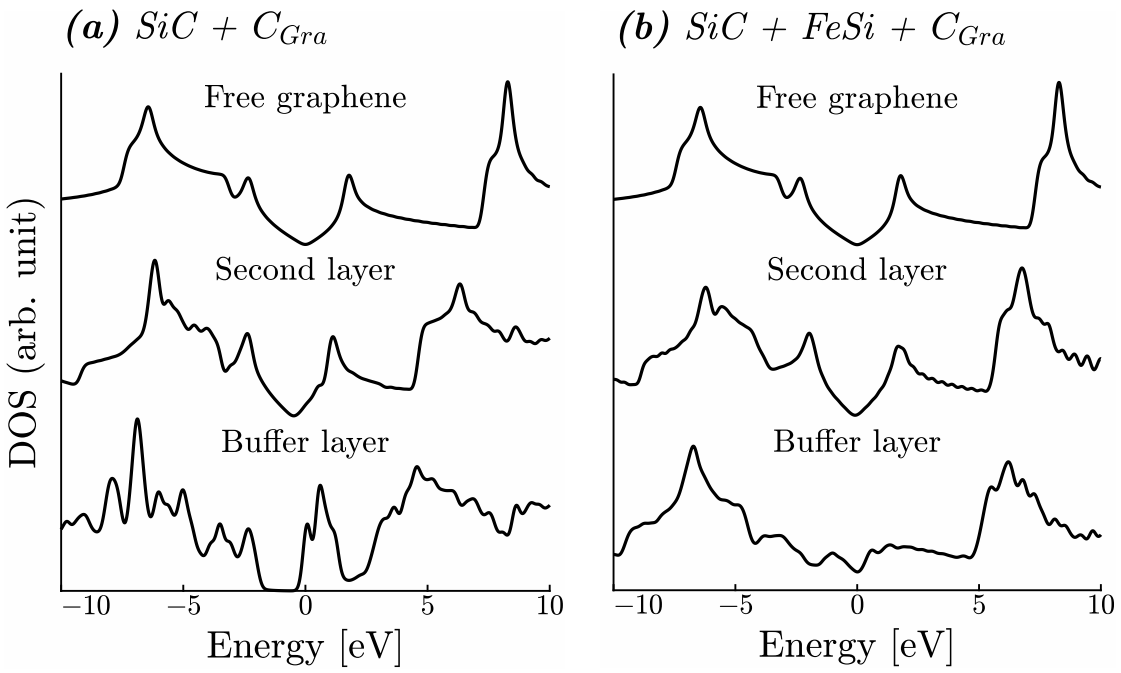

Figure 5.10: *Comparinson of the density of states in the first two layers of graphene epitaxially grown on* ***(a)*** *pure 6H-SiC and* ***(b)*** *iron-treated 6H-SiC. The density of states of free standing graphene is included in both subfigures as a reference. Calculated using SIESTA, see Sec. 4.5 for details.*

The physical structure of first graphene layer on the SiC-FeSi structure exhibits similar effects as the buffer layer on SiC. The atoms are again relaxed in a non-planar structure, and the density of states is highly distorted by the FeSi-interlayer. The DOS in this case suggests metallic behaviour in the buffer layer, as seen from the high DOS at the Fermi-level. The distance to the second graphene layer is 3.59 Å, which shows a DOS similar to that of FSG.

Chapter 6

Discussion

In this thesis the SiC-FeSi-C_{Gra} system was studied with regard to its suitability for making a radiation sensing device. The scope of this study has been declared in Chapter 4 in terms of objectives as **(1)** to study the formation and characteristics of graphene and the iron silicide interlayer on SiC, **(2)** to determine the suitability of the growth method for patterned formation of graphene, and **(3)** to fabricate a Hall bar for electrical measurements on the system. Each objective was directly addressed by experiments carried out, and satisfied to a certain extent.

In this chapter a discussion of the validity and implications of the Results is provided in the light the aforementioned objectives. The discussion is divided into four sections. In the first section the uncertainty in XPS analysis considered. This is a highly relevant topic as many conclusions drawn in this thesis are based on fine quantitative results from Chapter 5, such as the thickness of the formed graphene film, and ratio of iron and silicon in the interlayer. The subsequent section evaluates the validity of the computation methods presented in this thesis.

A general discussion about results regarding the growth of graphene on iron-treated SiC and graphene patterning by this method is provided in Sec. 6.3. There are many aspects about the SiC-FeSi-C_{Gra} system that are yet unknown such as the properties of the FeSi interlayer, and it is instructive to outline the contribution of results in this work to its understanding, and to consider the limitations of such results. To the knowledge of the author, although hypothesized [16], this is the first time patterning of graphene by this method has been demonstrated. In Sec. 6.4 aspects related to the formation of and electrical measurements on the graphene Hall bar are discussed.

6.1 Uncertainty in XPS analysis

As justified previously, discussing uncertainties of quantitative results from XPS analysis is imperative for making conclusions based on those results. Most of the results in Chapter 5 are reported with an estimate of the uncertainty, typically showing the 95% confidence interval for the given quantity. These values are however estimated using statistics on repeated measurements of the same value, goodness of fit, etc., and hence only consider random and some forms of systematic error that is possible to account for within the applied model.

An excellent example of an error which is impossible to account for using the current model of the layer structure is the uncertainty in the inelastic mean free path λ. It is expected that the largest source of uncertainty of quantitative results in this thesis stems from the uncertainty of λ, yet there is no way of controlling this uncertainty using the collected XPS data alone. As all layer thickness calculations rely on an assumption of the value of λ, and no data to confirms thickness of layers through other means of estimation.

The treatment of λ in XPS quantification tends to vary across the literature. In this work λ was consistently estimated by using an empirical formula from the compilation of 215 values of IMFP for various elements [41]. The equation was chosen for its simplicity and consistency across different materials. As however the materials used in this study are relatively common, finding fairly reliable reference values from literature should not be a difficult task. The National Institute of Standards and Technology (NIST) provides a database for the calculation of λ for various materials and electron energies [64]. A problem with such an approach is, however, the high sensitivity of the IMFP to fine material properties such as DOS at the Fermi-level and band gap [65], and thereby also phase and the presence of contaminants or dopants. Thus, even if λ for a given material is known accurately, the exact structure and hence the λ of the system under investigation is often not known.

Another potential source of error that is only partially accounted for in the reported uncertainties comes from the choice of peak profiles and components used to fit data. Although fit error is generally factored into the uncertainty, the correspondence between fit parameters of peak profiles and physical parameters of the sample is reliant on the choice of a model that is a good physical representation of the system. One could for instance, principally, fit an large number of peaks to any data obtaining a perfect fit, however the fit parameters in such case would not give any useful information about properties of the sample.

A concrete example of an imperfect model is the use of the Doniach-Sunjic peak profile with an arbitrary cut-off. Using this model the estimated thickness of a layer

by Doniach-Sunjic line shape is dependent an unjustified choice of a cut-off, and moreover the proportion of elements with Voigt- and asymmetric line shapes will be arbitrarily scaled. In some sources this problem has been solved by convolving the Doniach-Sunjic lineshape with a Gaussian profile, simulating the spectral width of the photon source [66, 67].

Similarly, various forms of pseudo-Voigt peak profiles exist, and using the real Voigt profile is also a possibility. The uncertainty from the used pseudo-Voigt function has however been shown to be below 1% [46], which is negligible compared to other sources of uncertainty in the present work. Many recent papers have been using the Tougaard model replacing the Shirley background, and it is argued to give a more realistic model along with a better fit [68].

Somewhat different results were obtained from the two samples A and B irrespective of fairly similar processing steps. A plausible contribution to this is the difference of XPS analysis for the two samples. As for sample A spectra from silicon carbide and tantalum -rich regions could be simultaneously collected, the contribution from tantalum was subtracted from the data for SiC to give an estimate of a spectrum collected with ideal alignment. Since no such spatial distinguishment could be made for measurements on sample B, no such subtraction could be done. The signal from tantalum is likely to have contributed to the oxygen peaks measured for determining levels of contamination.

Another common approximation made in XPS layer modelling is assuming uniform coverage of the layers, even for layers with sub-monolayer thickness. While this treatment does not give exact results, it is was assumed as including variable coverage in the model would complicate the fitting with the addition of more parameters, and thereby increase the uncertainty of the fit.

6.2 DFT and surface modelling

After discussing the uncertainty in XPS analysis it is time to review some of the inaccuracies in the calculation of the electronic bands and DOS of solids. As for all DFT calculations there is a general list of approximations, contributing to the error in calculated electronic structures. Such approximations include e.g. the use of an approximate exchange-correlation functional, treatment of core electrons by pseudopotentials, consideration of ground state configurations only and the imperfect convergence of the calculation to a global energy minimum. Such inaccuracies were superficially discussed in Sec. 2.2, and their most apparent consequence is typically the uncertainty in absolute calculated energies, most notably in the band gap of semiconductors [69].

Beside inaccuracies that are general for all DFT calculations, a number of additional limitations were present in the calculation described of the density of states of graphene on SiC and in the SiC-FeSi-C_{Gra} system. Several of those limitations are aspects that could potentially be improved in a more extensive study, and were not completed in this study due to insufficient computation time and the wide scope of this thesis.

Perhaps the most significant shortcoming of the computational study presented is that calculations for a very limited number of surface structures were carried out. Many assumptions had to be made in the alignment of surfaces, and a more comprehensive study should include more tests of what configuration yields the most realistic results. This also applies to the thickness and structure of iron silicide layer, as it exists in various crystal structures and its exact form in this system is not known for sure. All simulations were carried out on SiC (0001), as at the time simulations were begun experiments solely on Si-terminated SiC were carried out.

In all surface calculations a non-realistic supercell was used in the simulation of the lattice mismatch between layers in order to reduce computation time. It is for instance known that graphene forms a $(6\sqrt{3} \times 6\sqrt{3})$R30° structure on top of silicon carbide, however simulating a large enough unit cell to describe the supercell of this structure would require simulation of a very large number of atoms, and would therefore not be possible with the computational resources used in this thesis. Therefore a $(\sqrt{3} \times \sqrt{3})$R30° structure was used with a 2.4% strain of graphene's unit cell compared to relaxed structures. Similarly a compression of 1.7% of the FeSi lattice was required for modelling the SiC-FeSi-C_{Gra} structure.

Finally, it should be mentioned that in the relaxation of surface structures a smaller number of k-points was used than what is generally required for an accurate calculation. This also adds to the error of the calculations, as atoms in the structures were not relaxed to their ideal positions.

6.3 Graphene growth and patterning

One of the difficulties in growing high quality graphene has been obtaining a clean surface of SiC. As in situ direct current heating was not working at the time of this project, resistive heating was used to degas samples at temperatures lower than what is necessary to remove SiO_2 contamination from SiC [60], and the presence of oxygen contaminants after degassing was confirmed by XPS measurements. It is considered that contamination may have been the cause of not resolving bands in ARPES measurements on both clean SiC, and after graphene formation.

Small substrate size ($\sim 3.5 \times 7.5\,\mathrm{mm}$) along with the use of masks for patterning

made proper sample alignment in the detector difficult to achieve. Therefore all collected XPS spectra exhibit small tantalum peaks from the mask or sample holder. While the detector can in principle be optimized for measuring from a sufficiently small area, a potential cause for the inability to meet this is that the iris restricting the acceptance angle of the detector was broken at the home XPS system. The difficulty in obtaining a signal solely from SiC was especially limiting for interpreting UPS spectra, as it is a technique in which distinguishing between distinct elements and materials is generally more difficult.

Convincing evidence of graphene growth on iron-treated SiC $(000\bar{1})$ were provided by XPS and LEED data. The LEED pattern shows that the FeSi interlayer preserves the periodicity of SiC with the formation of graphene rotated 30° with respect to the substrate, similarly to epitaxially grown graphene on SiC. The reaction has been shown to be self terminating, providing better control over the thickness of graphene film formed compared to growth on clean SiC, which has been shown to be especially difficult on the $(000\bar{1})$ face [14].

Assuming that the thickness calculated for sample A is more accurate due to subtraction of the spectra from tantalum, it can be estimated that graphene is formed one monolayer per (7 ± 3) Å layer of deposited iron. This value is somewhat higher than the thickness 4.5 Å of iron film expected solely from stoichiometric counting based on the reaction $\mathrm{SiC + Fe \rightarrow FeSi + C_{Gra}}$. This could be explained by the formation of other phases of iron silicide, however could also mean that higher temperatures are necessary for the reaction to complete on SiC $(000\bar{1})$.

Spatially resolved XPS has proven to be a convenient method for comparing exposed and unexposed regions on patterned samples, and provides conclusive evidence that graphene patterning has been successful with an upper limit patterning resolution of a few hundred micrometers. AFM image of the sample showing the transition between exposed and unexposed regions suggests a patterning resolution of $\sim 1\,\mu\mathrm{m}$. It is expected that a higher resolution spatially resolved XPS could be achieved with the instrument given a functioning iris or improved alignment.

It is hence established that patterned deposition of iron constitutes a functional method for the formation of devices patterned by graphene, and a potential for it being applied in the fabrication of a wider range of graphene-based devices exists. The method is further illustrated in this thesis in the formation of a Hall bar. A disadvantage of the process is that iron deposition and annealing must be done in UHV which eliminates the possibility of using standard photolithography to pattern the iron film, and may pose difficulties for industrial scale processing. Patterning unconventional substrates by the use of shadow masks has been demonstrated with feature linewidths down to 10 nm [70], and therefore the aspect limiting patterning

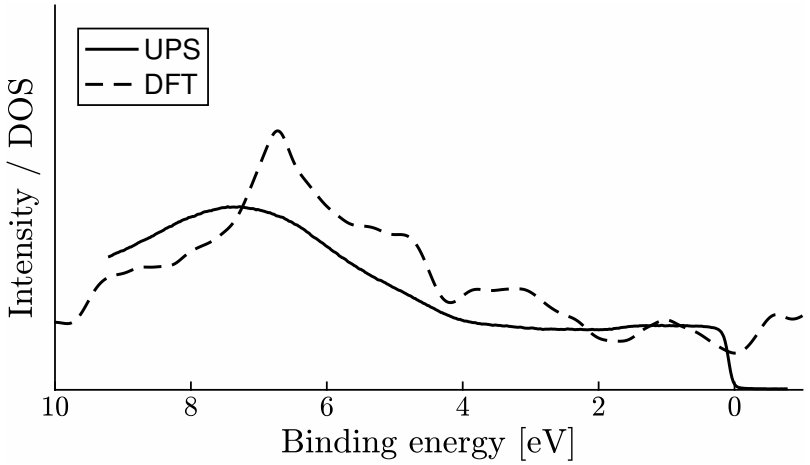

Figure 6.1: *Comparison of the UPS valence band spectrum of the sample after graphene formation and DFT simulation of the graphene DOS in the system (from Fig. 5.10). The results are in good agreement, suggesting a metallic buffer layer.*

resolution is thought to be the surface diffusion of iron during annealing.

For both samples A and B the aim has been to grow one monolayer of graphene, however quantitative XPS analysis suggests that slightly less was grown each time. For the formation of a working electrical device it is suggested that between 2-3 monolayers is grown. The primary justification for growing more than one monolayer is that the first graphene layer is thought to interact strongly with the FeSi interlayer. The formation of a buffer layer as the first layer of graphene with distinct electrical properties is known on various other substrates, and its formation in the system of the present study is supported by DFT calculations performed in this thesis. The calculations suggest that a metallic buffer layer is formed, which is in agreement with the measured band valence band spectrum of the FeSi-C_{Gra} system. This is illustrated in Fig. 6.1.

The formation of a buffer layer is the likely cause for no graphitic features observed in the Raman spectrum of a single sheet. It is hence also expected that electrical measurements on samples with only a monolayer will not exhibit the characteristic electrical behaviour of graphene such as the sharply peaked response to electric fields, or ultra-high mobility. Growing a second monolayer is believed to solve these problems, and should also make it possible to obtain ARPES measurements of graphene assuming that the sample including the graphene overlayer is of sufficiently high crystalline quality.

If the buffer layer is metallic, as suggested by DFT calculations, it may affect the

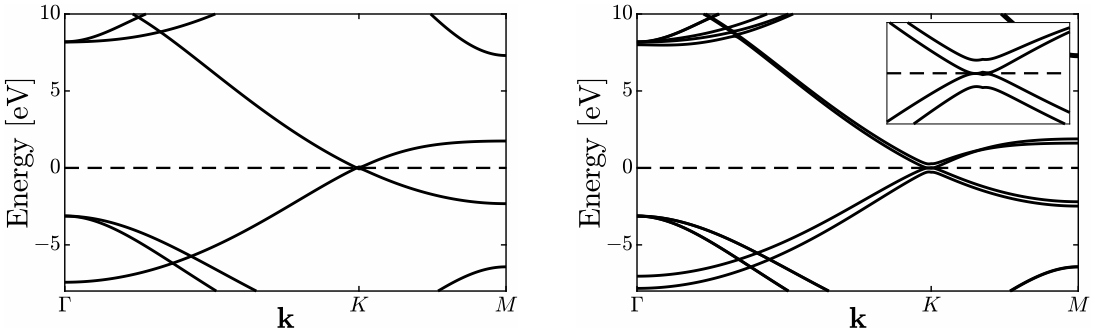

(a) *Monolayer* ***(b)*** *Bilayer*

Figure 6.2: *Band structure of a monolayer and bilayer of graphene showing the main difference at the Dirac-point where a linear behaviour of bands for bilayer graphene can no longer observed. Simulated using SIESTA (Sec. 4.5).*

device operation as the zero electric field conductivity will be higher than expected for a single sheet of free standing graphene. This might lead to less sharply peaked response to electric fields due to a larger zero-field conductance. It is nevertheless expected that the mobility of the buffer layer is significantly lower than of the second layer, and therefore a functional device should be possible to form.

An additional third layer of graphene might be advantageous in order to ensure full coverage of the sample surface by graphene. High coverage is a requirement for successful electrical measurements on graphene, and growing more than one monolayer in addition to the buffer layer would also ensure coverage over steps in the silicon carbide lattice. Growing a bilayer of graphene has the disadvantage that it distorts the the electronic band structure, lowering the electron mobility of graphene and making the ambipolar field effect less pronounced [71]. This is demonstrated in Fig. 6.2 showing the band structure of a mono- and bilayer of free standing graphene. Other works have shown that the band gap of graphene bilayer can be tuned by an electric field [72] which can be used to create field-effect transistors with similar behaviour as the discussed radiation detector. For the scope of this and successive studies however the primary goal should be demonstrating a proof-of-concept experiment, which is more likely to succeed with and additional layer of graphene.

Equally important are the electrical properties of the iron silicide interlayer. The band structure of bulk ϵ-FeSi is semiconducting with a small band gap (0.13 eV [73]), however its exact structure on SiC, and hence its electrical properties, are not known. Once exposed to atmospheric pressure the diffusion of oxygen through the thin graphene film may cause oxidation of the FeSi film, causing further altering of its electrical properties. The results in this thesis provide no convincing evidence about

the electrical properties of the FeSi layer.

6.4 Device formation and electrical measurements

Several practical difficulties were encountered during the formation of a Hall bar for electrical measurements. The masks were intended to be cut by a water jet cutter, however due to long waiting time at the mechanical workshop they were cut out by hand. Although a crude approach, it was thought to suffice for a proof-of-principle experiment. Slight misalignment of the two masks cut out lead to imperfect silver contacts, however this could be partially corrected with a scalpel. It was deemed essential to carry out silver deposition in situ, as this allowed the deposition of silver onto a clean surface which was properly degassed prior to the deposition.

The main limitation in Hall measurements arose from wiring to the silver contacts. Wire bonding was attempted, however it was given up due to the difficulty in achieving bonding of the wire to contacts, which were damaged by repeated attempts. It should also be noted that puncturing the potentially insulating FeSi layer should be avoided, as this would lead to measurement of the conductance of the sample too. Since wire bonding was unsuccessful, silver glue was used to attach wires to contacts, which turned out to have too high resistance for obtaining reliable Hall measurements. A better alternative may have been wire bonding by ball bonding, or even soldering.

Due to the poor wiring to the contacts, noisy Hall data was obtained with implausible results. It is however anticipated that even with proper wiring measurements would only reflect the electrical properties of the SiC due its high conductivity, and a too thin graphene layer with potentially poor coverage. The resistance of the sample across contacts 1-4 and 2-3 was measured $\sim 1\,\Omega$. The expected resistance of a sample with approximately square dimensions is equal to its sheet resistance, which for a high-quality single sheet of graphene is of the order of a few hundred ohms [74].

In an ideal radiation sensor device the high conductivity of the substrate should not compromise the operation of the device due to an insulating layer between graphene and the substrate. The measurement of substrate conductance between contacts therefore suggests that the insulating layer failed to stop charge carriers from entering the substrate. In the least desired case this could be caused by the non-insulating electrical properties of the FeSi interlayer. Other explanations include poor coverage of the layer, or the deposition some silver directly on SiC. There is a high possibility for the latter as iron deposition was carried out at a large angle from normal to the sample surface, and hence regions shadowed by the mask from iron may have been exposed to silver.

The value of electron mobility measured is unrealistically high for both graphene or SiC. It was estimated from gradient of the Hall voltage as a function of magnetic field, however an offset several orders of magnitude greater than the gradient was observed. This suggests that the Hall bar is geometrically asymmetric as the Hall voltage should vanish at zero magnetic field. This along with poor wiring to contacts justifies the incorrect measurement of even the substrate mobility.

The experiment should be repeated using a thicker sheet of graphene, a less conductive sample and better electrical contacts. It may be that different conductivity substrates must be used for characterisation of the graphene growth by XPS and for electrical measurements, as high resistivity samples tend to charge up under illumination by X-rays making XPS measurements inaccurate.

Photoconductance measurements led to nice linear IV-curves as probes were used directly on the silver contacts. There is nevertheless a problem associated with the use of probes as they pierce through the FeSi-layer, and hence the resistance of the entire sample most likely including the substrate is measured. Due to the high variance of photoconductance results it is difficult to conclude whether there is a systematic increase in the conductance of the sample as a result of incident light, however any increase observed is most likely due to the increased number of charge carriers in SiC rather than an electric-field effect in graphene.

Chapter 7

Conclusion and outlook

In this thesis the iron-mediated growth of graphene on SiC was investigated. The goal of the study was to evaluate the suitability of the growth process for making a radiation sensor based on the electric-field effect in graphene. Two successful samples were fabricated in UHV, and characterised by in situ XPS and LEED. A Hall bar was formed for electrical measurements on the system.

The growth of graphene was demonstrated by annealing iron-treated SiC $(000\bar{1})$ to 710 °C. XPS measurements suggest that approximately one monolayer of graphene is grown per (7 ± 3) Å of deposited iron, and the measured proportion iron and silicon in the interlayer is in good agreement with the formation of FeSi as the main phase. LEED data shows that the periodicity of SiC is transmitted to the graphene overlayer, which is rotated 30° with respect to the substrate. Graphene formation in this process has the advantage of greater control of the thickness of graphene film formed compared to epitaxial growth on clean SiC $(000\bar{1})$.

Approximately one monolayer of graphene was grown on two samples. Successful patterning of samples by evaporation of iron through shadow masks was demonstrated, for the first time to the knowledge of the author. The formation of graphene selectively on exposed regions was confirmed by spatially resolved XPS, and the method was applied in the formation of a Hall bar. Patterning by this method has the advantage of eliminating the complexity involved around using photolithography to remove graphene.

No graphitic features could be observed in the Raman spectrum of the samples. An explanation for this is provided by DFT calculations on the system, which suggest the formation of a buffer layer with metallic properties due to interaction with the underlying FeSi layer. The calculated DOS agrees well with the measured valence

band spectrum of the system. It is hence suggested that an additional graphene layer is grown in successive experiments to achieve the desired electrical behaviour of graphene. The conductive nature of the buffer layer may affect the performance of a sensor by increasing the intrinsic conductance of the device, however further study is required to make more certain conclusions about the nature of the buffer layer.

Electrical measurements on the Hall bar provided inconclusive results due to a number of practical limitations. The two most profound shortcomings of the experimental design were the growth of a too thin layer of graphene, and the high conductivity of the substrate. The FeSi interlayer failed to prevent the flow of charge carriers between contacts and the substrate. This may indicate that the FeSi layer is in fact conductive, however may also be caused by poor coverage or a fault in the device structure.

The main challenge that remains is to characterise the FeSi interlayer with respect to its electrical properties. As no evidence in this thesis gives clear indication of it being either conducting or insulating, it can also not be stated with certainty whether the SiC-FeSi-C_{Gra} system an appropriate candidate for forming the proposed radiation sensor.

Most direct evidence of the system's electrical behaviour is provided by electrical measurements, and hence further attempts to fabricate devices is suggested as future experiments. Hall or van der Pauw measurements provide valuable information about the charge carrier characteristics in a sample, and can in conjugation with photoconductance measurements provide conclusive evidence about whether the suggested device could be formed. Additional characterization of the electronic structure could be provided by local density of states measurements through STS as well as band structure mapping by ARPES.

Bibliography

[1] G. F. Knoll, *Radiation detection and measurement*. John Wiley & Sons, 2010.

[2] M. Foxe, G. Lopez, I. Childres, *et al.*, "Detection of ionizing radiation using graphene field effect transistors," in *Nuclear Science Symposium Conference Record (NSS/MIC)*, IEEE, 2009, pp. 90–95.

[3] K. S. Novoselov, A. K. Geim, S. V. Morozov, *et al.*, "Electric field effect in atomically thin carbon films," *science*, vol. 306, no. 5696, pp. 666–669, 2004.

[4] I. Ovid'ko, "Mechanical properties of graphene," *Rev. Adv. Mater. Sci*, vol. 34, no. 1, pp. 1–11, 2013.

[5] A. A. Balandin, "Thermal properties of graphene and nanostructured carbon materials," *Nature materials*, vol. 10, no. 8, pp. 569–581, 2011.

[6] A. C. Neto, F. Guinea, N. M. Peres, *et al.*, "The electronic properties of graphene," *Reviews of modern physics*, vol. 81, no. 1, p. 109, 2009.

[7] K. S. Novoselov, A. K. Geim, S. Morozov, *et al.*, "Two-dimensional gas of massless Dirac fermions in graphene," *nature*, vol. 438, no. 7065, pp. 197–200, 2005.

[8] S. Zhou, G.-H. Gweon, J. Graf, *et al.*, "First direct observation of Dirac fermions in graphite," *Nature physics*, vol. 2, no. 9, pp. 595–599, 2006.

[9] D. Reddy, L. F. Register, G. D. Carpenter, *et al.*, "Graphene field-effect transistors," *Journal of Physics D: Applied Physics*, vol. 44, no. 31, p. 313 001, 2011.

[10] M. Foxe, G. Lopez, I. Childres, *et al.*, "Graphene field-effect transistors on undoped semiconductor substrates for radiation detection," *IEEE Transactions on Nanotechnology*, vol. 11, no. 3, pp. 581–587, 2012.

[11] O. Koybasi, I. Childres, I. Jovanovic, *et al.*, "Graphene field effect transistor as a radiation and photodetector," in *SPIE Defense, Security, and Sensing*, International Society for Optics and Photonics, 2012, 83730H–83730H.

[12] A. Patil, O. Koybasi, G. Lopez, *et al.*, "Graphene field effect transistor as radiation sensor," in *Nuclear Science Symposium and Medical Imaging Conference (NSS/MIC)*, IEEE, 2011, pp. 455–459.

[13] C.-M. Seah, S.-P. Chai, and A. R. Mohamed, "Mechanisms of graphene growth by chemical vapour deposition on transition metals," *Carbon*, vol. 70, pp. 1–21, 2014.

[14] N. Mishra, J. Boeckl, N. Motta, *et al.*, "Graphene growth on silicon carbide: A review," *physica status solidi (a)*, vol. 213, no. 9, pp. 2277–2289, 2016.

[15] H. Zhou, W. J. Yu, L. Liu, *et al.*, "Chemical vapour deposition growth of large single crystals of monolayer and bilayer graphene," *Nature communications*, vol. 4, 2013.

[16] S. Cooil, F. Song, G. Williams, *et al.*, "Iron-mediated growth of epitaxial graphene on SiC and diamond," *Carbon*, vol. 50, no. 14, pp. 5099–5105, 2012.

[17] J. M. Soler, E. Artacho, J. D. Gale, *et al.*, "The SIESTA method for ab initio order-N materials simulation," *Journal of Physics: Condensed Matter*, vol. 14, no. 11, p. 2745, 2002.

[18] C. Kittel, *Introduction to solid state physics*. Hoboken, NJ: Wiley, 2005.

[19] P. Hofmann, *Solid state physics: an introduction*. John Wiley & Sons, 2015.

[20] D. Jamison and S. Waite, *Venture Investing in Science*. Columbia University Press, 2017.

[21] D. Sholl and J. A. Steckel, *Density functional theory: a practical introduction*. John Wiley & Sons, 2011.

[22] W. O'Mara, R. B. Herring, and L. P. Hunt, *Handbook of semiconductor silicon technology*. Crest Publishing House, 2007.

[23] D. J. Griffiths, *Introduction to quantum mechanics*. Cambridge University Press, 2016.

[24] S. M. Sze and K. K. Ng, *Physics of semiconductor devices*. John Wiley & Sons, 2006.

[25] S. Mukherjee, *Applied mineralogy: applications in industry and environment*. Springer Science & Business Media, 2012.

[26] P. R. Wallace, "The band theory of graphite," *Physical Review*, vol. 71, no. 9, p. 622, 1947.

[27] C. D. Simpson, J. D. Brand, A. J. Berresheim, *et al.*, "Synthesis of a giant 222 carbon graphite sheet," *Chemistry–A European Journal*, vol. 8, no. 6, pp. 1424–1429, 2002.

[28] J.-N. Fuchs and M. O. Goerbig, "Introduction to the physical properties of graphene," *Lecture Notes*, 2008.

[29] R. Saito, G. Dresselhaus, and M. S. Dresselhaus, *Physical properties of carbon nanotubes*. World scientific, 1998.

[30] K. I. Bolotin, K. Sikes, Z. Jiang, *et al.*, "Ultrahigh electron mobility in suspended graphene," *Solid State Communications*, vol. 146, no. 9, pp. 351–355, 2008.

[31] E. Pallecchi, F. Lafont, V. Cavaliere, *et al.*, "High electron mobility in epitaxial graphene on 4H-SiC (0001) via post-growth annealing under hydrogen," *arXiv preprint arXiv:1403.5059*, 2014.

[32] T. Ando, A. B. Fowler, and F. Stern, "Electronic properties of two-dimensional systems," *Reviews of Modern Physics*, vol. 54, no. 2, p. 437, 1982.

[33] J.-C. Charlier, P. Eklund, J. Zhu, *et al.*, "Electron and phonon properties of graphene: their relationship with carbon nanotubes," *Carbon nanotubes*, pp. 673–709, 2008.

[34] P. Hohenberg and W. Kohn, "Inhomogeneous electron gas," *Physical review*, vol. 136, no. 3B, B864, 1964.

[35] J. Fan and P. K. Chu, "General properties of bulk SiC," in *Silicon Carbide Nanostructures*, Springer, 2014, pp. 7–114.

[36] C. Berger, Z. Song, T. Li, *et al.*, "Ultrathin epitaxial graphite: 2D electron gas properties and a route toward graphene-based nanoelectronics," *The Journal of Physical Chemistry B*, vol. 108, no. 52, pp. 19 912–19 916, 2004.

[37] A. Einstein, "Über einen die erzeugung und verwandlung des lichtes betreffenden heuristischen gesichtspunkt," *Annalen der physik*, vol. 322, no. 6, pp. 132–148, 1905.

[38] K. Siegbahn and K. Edvarson, "B-ray spectroscopy in the precision range of 1:105," *Nuclear Physics*, vol. 1, no. 8, pp. 137–159, 1956.

[39] D. P. Woodruff, T. A. Delchar, and J. Rowe, *Modern techniques of surface science*, 1988.

[40] J. F. Watts and J. Wolstenholme, "An introduction to surface analysis by XPS and AES," *Wiley Online Library*, p. 224, 2003.

[41] M. P. Seah and W. Dench, "Quantitative electron spectroscopy of surfaces: a standard data base for electron inelastic mean free paths in solids," *Surface and interface analysis*, vol. 1, no. 1, pp. 2–11, 1979.

[42] *Interaction of gamma radiation with matter*, `http://http://www.nuclear-power.net`, Accessed: 2017-05-23.

[43] J.-J. Yeh, *Atomic calculation of photoionization cross-sections and asymmetry parameters*. Gordon & Breach Science Publ.; AT&T Bell Laboratories, 1993.

[44] S. Hüfner, *Photoelectron spectroscopy: principles and applications*. Springer Science & Business Media, 2013.

[45] P. Thompson, D. Cox, and J. Hastings, "Rietveld refinement of Debye–Scherrer synchrotron X-ray data from Al2O3," *Journal of Applied Crystallography*, vol. 20, no. 2, pp. 79–83, 1987.

[46] T. Ida, M. Ando, and H. Toraya, "Extended pseudo-Voigt function for approximating the Voigt profile," *Journal of Applied Crystallography*, vol. 33, no. 6, pp. 1311–1316, 2000.

[47] S. Doniach and M. Sunjic, "Many-electron singularity in X-ray photoemission and X-ray line spectra from metals," *Journal of Physics C: Solid State Physics*, vol. 3, no. 2, p. 285, 1970.

[48] D. A. Shirley, "High-resolution X-ray photoemission spectrum of the valence bands of gold," *Physical Review B*, vol. 5, no. 12, p. 4709, 1972.

[49] J. A. Eichmeier and M. Thumm, *Vacuum electronics: components and devices*. Springer Science & Business Media, 2008.

[50] H. Lüth, *Solid surfaces, interfaces and thin films*. Springer, 2001, vol. 4.

[51] M. H. Hablanian, *High-vacuum technology: a practical guide*. CRC Press, 1997, vol. 111.

[52] Specs, *PHOIBOS hemispherical energy analyser series*, SPECS, 2008.

[53] A. Seubert, J. Bernhardt, M. Nerding, *et al.*, "In situ surface phases and silicon-adatom geometry of the (2x2) C structure on 6H-SiC (0001)," *Surface science*, vol. 454, pp. 45–48, 2000.

[54] O. Madelung, U. Rössler, and M. Schulz, "Group iv elements, iv-iv and iii-v compounds," *Part a–Lattice Properties, Landolt-Börnstein–Group III Condensed Matter*, vol. 41, 2001.

[55] W. P. Davey, "Precision measurements of the lattice constants of twelve common metals," *Physical Review*, vol. 25, no. 6, p. 753, 1925.

[56] L. Vocadlo, G. D. Price, and I. Wood, "Crystal structure, compressibility and possible phase transitions in ε-FeSi studied by first-principles pseudopotential calculations," *Acta Crystallographica Section B: Structural Science*, vol. 55, no. 4, pp. 484–493, 1999.

[57] D. Gray, A. McCaughan, and B. Mookerji, "Crystal structure of graphite, graphene and silicon," *Physics for solid state applications. WVU, Boston*, 2009.

[58] X. Gonze, J.-M. Beuken, R. Caracas, *et al.*, "First-principles computation of material properties: the ABINIT software project," *Computational Materials Science*, vol. 25, no. 3, pp. 478–492, 2002.

[59] C. D. Wagner and G. Muilenberg, *Handbook of X-ray photoelectron spectroscopy*. Perkin-Elmer, 1979.

[60] W. Huang, X. Liu, X. C. Liu, *et al.*, "Nano-scale native oxide on 6H-SiC surface and its effect on the Ni/native oxide/SiC interface band bending," in *Materials Science Forum*, Trans Tech Publ, vol. 778, 2014, pp. 566–570.

[61] N. Ohtsu, M. Oku, K. Satoh, *et al.*, "Dependence of core-level XPS spectra on iron silicide phase," *Applied Surface Science*, vol. 264, pp. 219–224, 2013.

[62] F. Fromm, M. Oliveira Jr, A. Molina-Sanchez, *et al.*, "Contribution of the buffer layer to the Raman spectrum of epitaxial graphene on SiC (0001)," *New Journal of Physics*, vol. 15, no. 4, p. 043 031, 2013.

[63] A. Mattausch and O. Pankratov, "Ab initio study of graphene on SiC," *Physical Review Letters*, vol. 99, no. 7, p. 076 802, 2007.

[64] C. Powell and A. Jablonski, "The NIST electron effective-attenuation-length database," *Journal of Surface Analysis*, vol. 9, no. 3, pp. 322–325, 2002.

[65] S. Tanuma, C. J. Powell, and D. R. Penn, "Calculations of electron inelastic mean free paths (IMFPs). iv. evaluation of calculated IMFPs and of the predictive IMFP formula TPP-2 for electron energies between 50 and 2000 eV," *Surface and interface analysis*, vol. 20, no. 1, pp. 77–89, 1993.

[66] F. Sette, G. Wertheim, Y. Ma, *et al.*, "Lifetime and screening of the C 1s photoemission in graphite," *Physical review B*, vol. 41, no. 14, p. 9766, 1990.

[67] C. Morant, L. Galan, and J. Sanz, "An XPS study of the initial stages of oxidation of hafnium," *Surface and Interface Analysis*, vol. 16, no. 1-12, pp. 304–308, 1990.

[68] S. Tougaard and C. Jansson, "Comparison of validity and consistency of methods for quantitative XPS peak analysis," *Surface and Interface Analysis*, vol. 20, no. 13, pp. 1013–1046, 1993.

[69] A. Seidl, A. Görling, P. Vogl, *et al.*, "Generalized Kohn-Sham schemes and the band-gap problem," *Physical Review B*, vol. 53, no. 7, p. 3764, 1996.

[70] L. Li, I. Bayn, M. Lu, *et al.*, "Nanofabrication on unconventional substrates using transferred hard masks," *Scientific reports*, vol. 5, 2015.

[71] S. Xiao, J.-H. Chen, S. Adam, *et al.*, "Charged impurity scattering in bilayer graphene," *Physical Review B*, vol. 82, no. 4, p. 041 406, 2010.

[72] G. Fiori and G. Iannaccone, "On the possibility of tunable-gap bilayer graphene FET," *IEEE Electron Device Letters*, vol. 30, no. 3, pp. 261–264, 2009.

[73] L. Mattheiss and D. Hamann, "Band structure and semiconducting properties of FeSi," *Physical Review B*, vol. 47, no. 20, p. 13 114, 1993.

[74] J. Krupka and W. Strupinski, "Measurements of the sheet resistance and conductivity of thin epitaxial graphene and SiC films," *Applied Physics Letters*, vol. 96, no. 8, p. 082 101, 2010.